

2
2009

This is to certify that the
dissertation entitled

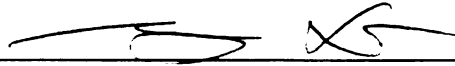
CARBON NANOTUBE BASED INFRARED SENSORS –
DESIGN, FABRICATION, AND TESTING

presented by

JIANGBO ZHANG

has been accepted towards fulfillment
of the requirements for the

Ph.D. degree in Electrical Engineering



Major Professor's Signature

12/1/08

Date

**CARBON NANOTUBE BASED
INFRARED SENSORS - DESIGN,
FABRICATION, AND TESTING**

By

Jiangbo Zhang

A DISSERTATION

Submitted to
Michigan State University
in partial fulfillment of the requirements
for the degree of

DOCTOR OF PHILOSOPHY

Electrical Engineering

2008

ABSTRACT

CARBON NANOTUBE BASED INFRARED SENSORS - DESIGN, FABRICATION, AND TESTING

By

Jiangbo Zhang

In this research, we focus on the design, fabrication, and testing of single carbon nanotube (CNT) based infrared (IR) sensor, which consists of two microelectrodes bridged by a single CNT. Sensors with symmetric structure and asymmetric structure were designed respectively to study the dependence of the photocurrent on CNT-metal contacts. In a symmetric structure (same metal for both sides), photogenerated electrons and holes at one CNT-metal interface have to tunnel through another interface to form photocurrent, and the photocurrents from the two reversely connected diodes will cancel each other. While the asymmetric structure (different metals for both sides) increases the measurable photocurrent by lowering one of the Schottky barriers and enlarging the difference between the photocurrents generated at the two CNT-metal interfaces.

Nano-manufacturing/assembly plays an extremely important role in studying nanomaterials and nanodevices including the CNT nanodevices. To fabricate the CNT based IR sensors, a nanoassembly process which is able to assemble a single CNT/nanowire onto a pair of microelectrodes using the Atomic Force Microscope (AFM) based nano-robotic manipulation system and the dielectrophoresis (DEP) deposition system, was developed and experimentally tested. The DEP force attracts one or more individual CNTs around the microelectrodes. Then the AFM based nanomanipulation system manipulates one CNT to bridge the microelectrodes and cleans the rest CNTs and particles away from the microelectrodes. This nanoassembly

process provides a controllable, reliable and efficient approach to assemble nanodevices.

With the developed nanoassembly process, single CNT based Schottky photodiodes using symmetric and asymmetric structures have been fabricated. Experimental measurements on both types of devices have shown that the asymmetric structure can improve the photodiode performance by increasing the signal-to-dark current ratio up to three orders of magnitude higher than a symmetric device. It has also been verified that the photocurrent is generated by the photovoltaic effect rather than heating or photoconduction effect as previously reported. With the asymmetric structure, middle infrared (MIR) detection has been demonstrated using individual MWNTs, whose bandgap was tuned by electrically burning out the outer layers of the MWNT.

Furthermore, multi-pixel CNT sensor arrays have been fabricated and tested in this study. The fabrication of multi-pixel CNT sensor array demonstrated that the developed nanoassembly process is able to fabricate single CNT/nanowire device arrays, which is difficult for other fabrication methods. Experimental testing results on CNT sensor arrays have shown that the adjacent pixels have small thermal crosstalk, which is an important factor limiting the pixel pitch of IR focal plane arrays (IRFPAs). The small pixel pitch of the developed CNT detector array makes it possible to fabricate high resolution IRFPAs. Moreover, a multicolor CNT IR sensor has also been developed by assembling two CNTs with different diameter (bandgap) on two adjacent microelectrode pairs respectively. The multicolor CNT IR sensor further demonstrated the abilities of the developed nanoassembly process and showed potential applications of CNTs in advanced IR sensor systems, which need multicolor capability for better target discrimination, tracking, and identification, as well as temperature determination.

*To my parents, my wife Ying Zhao,
and to my daughter, for their love and support*

ACKNOWLEDGMENTS

I would like to express my sincere gratitude and appreciation to my advisor, Dr. Ning Xi, for providing me with the unique opportunity to work in the research area of nanomanufacturing and nanosensors, for his expert guidance and generous help, and for his encouragement and support for my work. I am grateful to him for giving me the support and confidence during the period of my doctoral studies.

I would like to thank all members of my guidance committee: Dr. Jes Asmussen, Dr. Timothy Grotjohn, Dr. Hassan Khalil, Dr. Guowei Wei. At different stages of my Ph.D. studies, they offered me timely help and unfailing support. Their astute comments and suggestions have enhanced both the technical soundness and the presentation of this dissertation.

I would like to express my sincere gratitude to all the colleagues from the Robotics and Automation Laboratory especially to Dr. Guangyong Li for many hours of discussions and mentoring during my doctoral studies. Hongzhi Chen and Dr. King Wai Chiu Lai have helped me fabricate electrode chips. The discussions with Dr. Yantao Shen, Dr. Quan Shi, Lianqing Liu, and Dr. Uchechukwu Wejinya have substantially contributed to my work and broadened my knowledge.

No matter how much I acknowledge the support I received from all those mentioned above, my deepest gratitude goes to my parents, and my wife, Ying Zhao. They have always been my cheerleaders and supporters. This dissertation would not have been possible without their years of encouragement and continuous support. With love and gratitude, I dedicate this dissertation to them.

TABLE OF CONTENTS

LIST OF TABLES	viii
LIST OF FIGURES	ix
1 Introduction	1
1.1 Overview	1
1.2 Literature Review	2
1.2.1 Carbon Nanotubes	2
1.2.2 Design of CNT Infrared Sensors	5
1.2.3 Fabrication of CNT Devices	7
1.2.4 Testing of CNT Infrared Sensors	21
1.3 Objectives and Challenges	22
1.4 Organization of Dissertation	24
2 Design of Carbon Nanotube based Infrared Sensors	25
2.1 Manufacturing Issues in Design	25
2.2 Diode based CNT Sensor	26
2.3 Optimizing the CNT Sensor	27
2.4 Chapter Summary	29
3 Assembly of Carbon Nanotube based Infrared Sensors	30
3.1 Development of the Fabrication Process for Single CNT based Nano- Devices	31
3.2 Development of the AFM based Nanomanipulation System	33
3.2.1 Modeling of Adaptable End Effector	34
3.2.2 Control of Adaptable End Effector	45
3.2.3 Experimental Implementation	50
3.2.4 Experimental Results on Manipulating Nano-Objects	56
3.3 Experimental Results on Fabricating Single CNT based Infrared Sensors	62
3.4 Chapter Summary	62
4 Testing of Single CNT based IR Sensors	66
4.1 Development of the Testing System	66
4.2 Individual Multi-Walled Carbon Nanotube based IR Sensors	68
4.2.1 Bandgap Engineering of MWNTs	68
4.2.2 Experimental Testing of MWNT Sensors	70
4.3 Individual Single-Walled Carbon Nanotube based IR Sensors with Symmetric Structure	73

4.4	Individual Single-Walled Carbon Nanotube based IR Sensors with Asymmetric Structure	77
4.5	Sensing Middle IR Using CNT Based IR Sensors	81
4.6	Temperature Dependence of CNT Based IR Sensors	86
4.7	Performance Evaluation and Analysis	88
4.8	Chapter Summary	96
5	Multi-Pixel CNT Sensor Array	97
5.1	Fabrication of Single CNT based IR Sensor Array	98
5.2	Testing of Multi-Pixel CNT Sensor Array	99
5.3	CNT based Multi-color IR Sensors	102
5.4	Chapter Summary	111
6	Conclusions	114
6.1	Major Contribution	115
6.2	Future Research	116
	REFERENCES	119
	BIBLIOGRAPHY	124

LIST OF TABLES

3.1	Cantilever parameters	51
3.2	Damping constants	52
3.3	Modal frequencies (kHz)	52
4.1	Quantum efficiency of different IR materials	95

LIST OF FIGURES

1.1	(a) Schematic honeycomb structure of a graphene sheet. (b) CNT cylinders with different chiralities. ([16])	3
1.2	The structure of an ideal CNT diode. ([14])	6
1.3	Diagram illustrating the displacement photocurrent measurement technique. ([15])	7
1.4	(a) Optical image of an array of CNT devices. (b) Optical image of a single device with three CNTs bridging the electrodes. (c) Scanning electron microscope (SEM) image of a single device. ([35])	9
1.5	The AFM image of two electrodes bridged by several SWNTs which were deposited by DEP process. ([37])	11
1.6	Schematic diagram of a head scanning AFM.	12
1.7	Possible mechanical manipulation tasks using an AFM probe. ([67])	14
1.8	Pushing a silver nanowire with an unpreloaded traditional tip ($k=0.57\text{N/m}$). (a) Schematic illustration of the pushing process. (b) The AFM image of a silver nanowire with length of $2.5\mu\text{m}$ and diameter of 120nm . The scanning range is $10\mu\text{m} \times 10\mu\text{m}$.(c) The AFM image by a new scan after pushing. (d) Tip displacement signal measured by the photodiode sensor.	15
1.9	Pushing a silver nanowire with a preloaded traditional tip ($k=1-5\text{N/m}$). (a) Schematic illustration of the pushing process. (b) The AFM image of a silver nanowire with length of $2.5\mu\text{m}$ and diameter of 120nm . The scanning range is $10\mu\text{m} \times 10\mu\text{m}$. (c) The AFM image by a new scan after pushing. (d) Tip displacement signal measured by the photodiode sensor.	17
1.10	Schematic illustration of pushing a nano-object using the adaptable end effector.	18
1.11	Flexible beam	20
1.12	Temporal photocurrent response of a SWNT film. ([10])	22
1.13	Gating characteristics of an ambipolar NT-FET with and without infrared illumination ([13])	23

2.1	(a) Structure of the single CNT based infrared sensor. (b) Cross section of the microelectrodes.	26
2.2	Illustrations of pushing CNT over the microelectrodes which are fabricated by (a) etching and (b) lift off process.	26
2.3	The energy band diagrams of the CNT-metal contact for (a) n-type CNTs and (b) p-type CNTs.	27
2.4	The single CNT based infrared sensors with symmetric contacts. (a) Structure of the CNT sensors. (b) Energy band diagram of the CNT sensors.	28
2.5	The single CNT based infrared sensors with asymmetric contacts. (a) Structure of the CNT sensors. (b) Energy band diagram of the CNT sensors.	29
3.1	(a) The CNT assembly process. (b) The fabrication process of micro electrodes.	31
3.2	The CNT deposition process.	32
3.3	The setup of the AFM based nanomanipulation system using adaptable end effector.	34
3.4	The control scheme of the AFM based nanomanipulation system using adaptable end effector. 1: Piezo tube. 2: Piezoceramic layer of the adaptable end effector. 3: Adaptable end effector. 4: Substrate surface. 5: Object. 6: Laser beam. 7: Quad-photodiode detector. 8: Mirror. 9: Laser gun.	35
3.5	Adaptable end effector with an integrated Zinc Oxide piezoelectric actuator.	36
3.6	Adaptable end effector configuration.	37
3.7	Diagram of the cantilever under bending.	39
3.8	Controller block diagram.	50
3.9	Measured tip vibration of the cantilever without closed-loop control. .	53
3.10	Tracking response of (a) a sine wave and (b) a triangular wave. The controller is LQR controller.	55
3.11	Tracking response of (a) a sine wave and (b) a triangular wave. The controller is a PD controller.	56

3.12	(a) Tracking response of a square wave with PD controller. (b) Tracking response of a square wave with PD controller. (c) Zoom in around 0.016 sec in (b).	57
3.13	Tracking response of a square wave with the LQR controller and input shaping	58
3.14	Pushing a silver nanowire with an adaptable end effector. (a) The AFM image of a silver nanowire with length of $1.9\mu m$ and diameter of $120nm$. The scanning range is $6\mu m \times 6\mu m$. (b) The AFM image by a new scan after pushing. (c) The control voltage applied on the adaptable end effector. (d) Tip displacement signal measured by the photodiode sensor.	59
3.15	Successful rates of manipulations using different probe	61
3.16	Manipulating a CNT onto a pair of gold electrodes. (a) The AFM image before manipulation. (b) The image from a new AFM scan after manipulations.	63
3.17	Manipulating a CNT onto a pair of gold electrodes. (a) The AFM image before manipulation. (b) The image from a new AFM scan after manipulations.	63
3.18	Four different results of pushing CNT onto gold electrodes.	64
4.1	(a) The SWNT IR detection system. (b) The structure of the CNT chip.	67
4.2	The cryogenic MIR testing system.	68
4.3	I-V curves of a single MWNT device.	69
4.4	I-V curve of the single MWNT device after three breakdowns.	69
4.5	AFM image of the MWNT IR sensor.	71
4.6	I-V curve of the MWNT IR sensor.	71
4.7	Temporal photoresponse of the MWNT IR sensor. The bias voltage across the electrodes is $-0.1 V$	72
4.8	Temporal photoresponse of the MWNT IR sensor. The bias voltage across the electrodes is $0.1 V$	72
4.9	The plot of photocurrent vs. bias voltage.	73
4.10	(a) AFM image of an individual SWNT based photodiode with symmetric Au electrodes. (b) I-V curve of the CNT photodiode.	74

4.11	Temporal photocurrent response of the SWNT photodiode with a zero bias voltage. (a) IR irradiates the left electrode. (b) IR irradiates the right electrode.	75
4.12	The plot of the photocurrent as a function of the IR spot position. . .	77
4.13	(a) AFM image of an individual CNT photodiode with asymmetric Ti-Au electrodes. (b) I-V curve of the asymmetric CNT photodiode. .	78
4.14	(a) The photocurrent as a function of the IR spot position. (b) Temporal photocurrent response of the photodiode with asymmetric electrodes. The device was zero biased. The IR power was 30 mW. . . .	79
4.15	I-V characteristic curves of the asymmetric CNT photodiode. P_0 - P_3 represent different IR powers.	81
4.16	I-V characteristic curve of a MWNT MIR sensor	82
4.17	I-V characteristic curve of the MWNT MIR sensor after first breakdown	83
4.18	Temporal photoresponse of the MWNT sensor to NIR	84
4.19	I-V characteristic curve of the MWNT MIR sensor after second breakdown	85
4.20	Temporal photoresponse of the MWNT sensor to MIR	86
4.21	I-V characteristic curves of a MWNT sensor at different temperatures. The sensor was assembled through nanomanipulation.	87
4.22	I-V characteristic curves of a MWNT sensor at different temperatures. The sensor was assembled without nanomanipulation.	88
4.23	Temporal NIR photocurrent response of an individual SWNT IR sensor measured at high sampling rate	90
5.1	Nano-manufacturing process for single CNT based nanodevices. . . .	99
5.2	(a) The structure of a single pixel CNT IR sensor. (b) The 3D AFM image of a three-pixel CNT IR sensor array.	100
5.3	The AFM image of the three-pixel CNT IR sensor.	101
5.4	I-V curves of the three pixels.	102
5.5	Illustration of the photocurrent measurements. IR spot was on (a) pixel 1, (b) pixel 2 and (c) pixel 3 respectively.	102

5.6	Temporal photocurrent response of each pixels while the IR spot was on pixel 1 (Fig. 5.5(a)).	103
5.7	Temporal photocurrent response of each pixels while the IR spot was on pixel 2 (Fig. 5.5(b)).	103
5.8	Temporal photocurrent response of each pixels while the IR spot was on pixel 3 (Fig. 5.5(c)).	104
5.9	Structure of the multicolor CNT IR sensor	105
5.10	I-V characteristic curve of the SWNT pixel of the multicolor CNT IR sensor	106
5.11	NIR response of the SWNT pixel of the multicolor CNT IR sensor	106
5.12	I-V characteristic curve of the MWNT pixel of the multicolor CNT IR sensor	108
5.13	I-V characteristic curve of the MWNT pixel after breaking down outer layers	109
5.14	NIR response of the MWNT pixel of the multicolor CNT IR sensor	111
5.15	MIR response of the MWNT pixel of the multicolor CNT IR sensor	112

CHAPTER 1

Introduction

1.1 Overview

The development of middle infrared (MIR) sensors that operate near ambient temperature will allow significant simplifications of thermal imaging systems for applications such as remote sensing, environmental monitoring, medical diagnostics, as well as defense and aerospace applications. Photonic MIR sensors have been made with materials that have energy bandgaps sufficiently small to absorb MIR radiation. However, the small bandgap makes such sensors susceptible to thermal noise. Hence the traditional photonic MIR sensors have to work at ultra low temperature. As a one-dimensional (1-D) nanostructural material, carbon nanotubes (CNTs) have potential applications in solar collection and IR sensing due to their unique properties such as direct bandgap, wide range of bandgaps, and reduced carrier scattering. With the unique properties, CNT based MIR sensors have the potential to work at room temperature or moderate low temperature with a high quantum efficiency. Hence it is very important and necessary to study electronic and photonic properties of CNTs. However, since CNT films or bundles lose the advantages brought by the 1-D structure of CNTs, it becomes necessary to study the single CNT based nanodevices.

To study the single CNT based nanodevices, a manufacturing process is required to make a CNT into nanodevice. This process is normally called nano-manufacturing or nano-assembly. Nano-manufacturing plays an extremely important role in studying nanomaterials and nanodevices including the CNT nanodevices. With its ability to characterize and modify the sample surface at molecular and atomic scales, Atomic Force Microscope (AFM) provides such a promising way to build or modify nanodevices. With AFM, nanoobjects (such as DNAs, CNTs, nano-wires, etc.) can be moved and positioned very accurately. Since AFM scans the sample surface by measuring attractive or repulsive forces between a tip and the sample, it is impossible to image the sample surface when the tip is used for manipulations. This means the object is unobservable when it is being manipulated. To facilitate AFM based nanomanipulations and improve the accuracy of nanomanipulations, it is very important to develop a tele-operation system with a sensitive force feedback and accurately tip position control.

1.2 Literature Review

1.2.1 Carbon Nanotubes

As the traditional silicon based semiconductor industry faces increasing technological and financial challenges on the way to further scaling down, new technologies and concepts have to be developed and assessed. CNT is such a candidate and is likely to create breakthroughs in the fields of nanoelectronics. Since the discovery of CNTs in 1991 [1], their mechanical and electrical properties have been intensively studied. Due to their unique hollow cylindrical structure, carbon nanotubes have promising potential applications in nano-electronics [2,3] and nano-mechanics [4]. They are able to work as fundamental building blocks of nano-electronic devices with their excellent one-dimensional material properties [5]. They are also extremely strong materials and

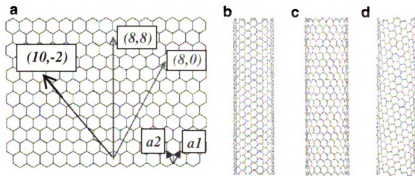


Figure 1.1. (a) Schematic honeycomb structure of a graphene sheet. (b) CNT cylinders with different chiralities. ([16])

have good thermal conductivity [6]. Moreover, carbon nanotube's photobehavior has attracted lots of attention due to their well-defined one-dimensional structure [7–15].

A single-walled carbon nanotube (SWNT) is formed by rolling a sheet of graphene into a cylinder along a lattice vector (m,n) in the graphene plane. The (m,n) vector determines the diameter and the particular roll orientation of a CNT, which is called the chirality. The (m,n) vector is also called chiral vector. The angle between the roll orientation and the axis of the tube is termed the chiral angle. The chirality (or chiral angle) determines the electronic properties of a CNT. Depending on the chirality, CNTs with same diameter can be either metallic or semiconducting. There are three types of rolls: armchair, zigzag, and chiral. Armchair CNTs are formed when $m=n$. The chiral angle of an armchair CNT is 30° , and the armchair CNTs display metallic properties. Zigzag CNTs are formed when either n or m equals zero, where the chiral angle is 0° . All other lattice vectors result in nanotubes that are termed chiral CNTs. Both zigzag and chiral CNTs are semiconducting. As shown in Fig. 1.1a, there are three lattice vectors $(8,8)$, $(8,0)$, $(10,-2)$. Folding of the three vectors leads to armchair, zigzag, and chiral tubes, as shown in Fig.1.1b-d respectively. The diameter of a SWNT is determined by the vector (m,n) with the equation [17]

$$d_{CNT} = \frac{a\sqrt{3(m^2 + mn + n^2)}}{\pi} = \frac{C_h}{\pi} \quad (1.1)$$

where a is the carbon to carbon bond length (1.42 Å), or the length between consecutive carbon atoms. C_h is the length of the chiral vector (m,n).

A metallic CNT has a much higher conductivity than the best metals, and semiconducting CNTs have mobilities and transconductances that meet or exceed the best semiconductors [5]. Hence the metallic CNTs have the potential to work as nanowires for interconnection in nanodevices. And the semiconducting CNTs have the potential to be the future material for field effect transistor channels. The bandgap of a semiconducting CNT is give by the equation [17–20]

$$E_{gap} = \frac{4\hbar v_f}{3d_{CNT}} \quad (1.2)$$

where v_f is the fermi velocity, and \hbar is the Dirac constant. The unique electrical properties of SWNTs are caused by the confinement of electrons in the two directions and the requirements for energy and momentum conservation. These constrains reduce the scattering processes of electrons and result in a ballistic transport.

As rolling a single graphene sheet into a SWNT, a multi-walled carbon nanotube (MWNT) can be formed by rolling multiple layers of graphene sheets into a cylinder shape. Hence a MWNT consists of multiple tubes [17, 21] with spacing between consecutive tubes of 3.4 Å [22]. Each layer of the MWNT can have different chirality and can be metallic or semiconducting. It has been reported that the concentric tubes of a MWNT have poor electrical contact with each other [23]. Theoretical and experimental studies have also shown that the outermost layer of a MWNT dominates

the electrical conduction of the MWNT [24]. Since the bandgap of a SWNT varies inversely with its diameter and the outermost layer of MWNT normally has a large diameter exceeding 10 nm [22]. The bandgap of the outermost nanotube is so small that MWNTs are metallic in nature.

With its outstanding properties, CNT has potential applications in a wide range of fields. MWNTs have been studied as very-large-scale integration (VLSI) interconnectors because of their high thermal stability, high thermal conductivity and high current conductivity [25]. Semiconducting CNTs have been used as the channels of field effect transistors (CNTFETs) because of their superior electrical characteristics [26–31].

1.2.2 Design of CNT Infrared Sensors

As a 1-D nano-structural material, carbon nanotubes (CNTs) have potential applications in solar collection and IR sensing due to their unique properties such as direct bandgap, wide range of bandgaps [5], and reduced carrier scattering [32]. Many researchers are looking into CNT optoelectronics, and the photoconductivity of CNTs has been studied in thin single-walled carbon nanotube (SWNT) films [9,10,33], multi-walled carbon nanotube (MWNT) arrays [11], and single SWNT transistors [12,13]. It has also been demonstrated that both semiconducting and metallic SWNTs can function as photodetectors over a wide spectral range using capacitive photocurrent measurement [15]. Moreover, a single SWNT *p-n* junction diode was built in [14] to demonstrate its photovoltaic effect.

The CNT based photosensing devices can be classified into three categories based on their structures. The first category is the basic structure with a pair of micro-electrodes bridged by a CNT or CNT bundle/film [10,11,33]. The second type of the CNT photosensing device is featured with the gate structure. Gate electrodes are employed to electrically control the photoconducting of the CNT channel [12,13].

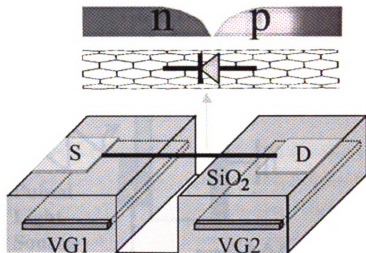


Figure 1.2. The structure of an ideal CNT diode. ([14])

As shown in Fig. 1.2, two bottom gate was used to electrically shift the fermi level of the CNT at both ends to create a p - n junction in the middle of the CNT [14]. As shown in Fig. 1.3, the third type of the CNT photosensing device is a metal-insulator-semiconductor photodetector [15]. Photons are detected by measuring the displacement photocurrent on the semiconductor.

The first structure is simple and easy to implement. The other two structures may leads to a better performance, but the complicated design makes it difficult to fabricate, especially for the device arrays. In this research, we will first fabricate the single CNT based IR sensors using the basic structure (two microelectrodes bridged by a CNT) to study the photobeaviors of single CNTs. After that, new designs enhanced by additional structures will be employed to improve the performance of the single CNT based IR sensors.

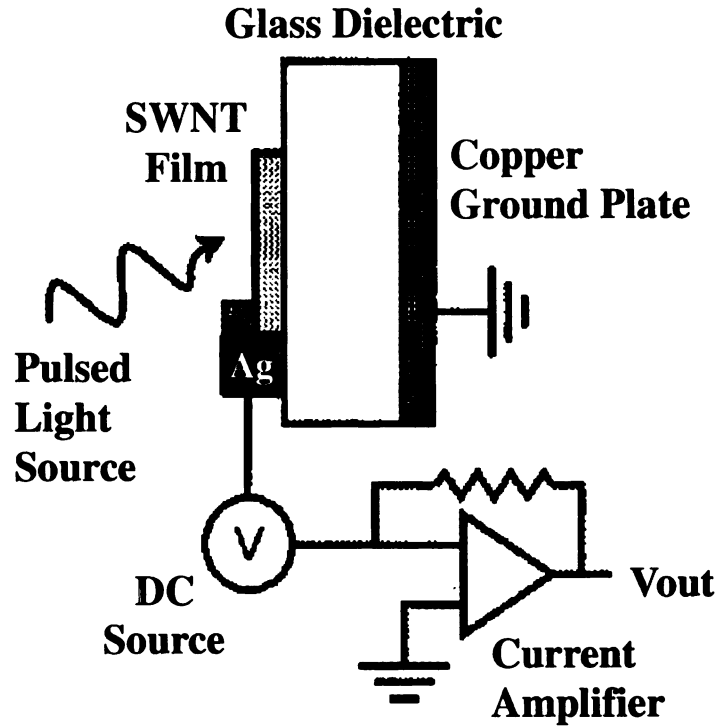


Figure 1.3. Diagram illustrating the displacement photocurrent measurement technique. ([15])

1.2.3 Fabrication of CNT Devices

The techniques for manufacturing nanodevices can be generally classified into bottom-up and top-down methods. The fabrication process of CNT devices normally includes both methods, where top-down methods are used to fabricate supporting structures such as contacting electrodes, and bottom-up methods are used to assemble CNTs with the supporting structures. Current available methods in fabricating single CNT devices include directly growth of CNT across microelectrodes [14, 34–36], deposition of as-grown CNTs on electrodes by dielectrophoresis (DEP) [37–40], fabrication of electrodes on top of as-deposited CNTs either by electron beam lithography (EBL) [41–43] or by shadow masks [44,45], and self-assembly by functionalizing CNTs

and electrodes with different chemicals or even DNA molecules [46,47]. To a certain extent, these methods have their shortcomings in terms of repeatability, mass production, and ability in eliminating uncertainties.

Directly Growth

With the directly growth method, single CNT devices are fabricated by directly growing a single CNT between a pair of prefabricated microelectrodes to make connections [14,34–36]. The directly growth method is able to fabricate multiple single CNT devices at one time. Thus it is good for making CNT based nanodevice arrays. But limitation of this method is that the properties of the CNTs can not be effectively controlled. Different CNTs may have different properties even they were produced at one batch. Moreover, the production process may generate impurities around the microelectrodes and CNTs, which will affect the electronic properties of the CNT device. The third limitation is that it is difficult to only grow a single CNT between the microelectrodes. Since CNT bundles or films lose the unique properties brought by the 1-D structure of CNTs, this limitation limits the performance of the CNT device. As shown in Fig. 1.4, an array of CNT devices were fabricated by CVD growth of SWNTs across the prefabricated electrodes pairs [35]. But as shown in Fig. 1.4(c), there were more than one CNT between the electrodes pair. Since different CNTs may have different properties, multiple CNTs bridging two electrodes will makes it difficult to control and analyze the properties of the device.

EBL Fabrication

Another approach for CNT assembly is to grow CNTs on the substrate surface first (or disperse the pre-grown and purified CNTs on the substrate surface), then use EBL fabrication or shadow mask to form microelectrodes on the top of a single CNT which was located by scanning electron microscope (SEM) [41–43]. This fabrication method

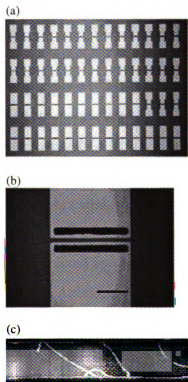


Figure 1.4. (a) Optical image of an array of CNT devices. (b) Optical image of a single device with three CNTs bridging the electrodes. (c) Scanning electron microscope (SEM) image of a single device. ([35])

provides a best contact condition between the CNT and microelectrodes among these fabrication methods. But due to the low efficiency of the EBL fabrication process, this method is inefficient. More importantly, since the CNTs are randomly distributed on the substrate surface, it is impossible to fabricate a CNT device array which aligns in a desired pattern. Hence the EBL fabrication method is only good for prototyping individual devices.

DEP Deposition

Instead of fabricating microelectrodes on the top of randomly distributed CNTs, preproduced and purified CNTs are manipulated to bridge two preformed microelectrodes. There are two ways to manipulate CNTs, dielectrophoresis (DEP) manipulation and nanoprobe based mechanical manipulation. With the DEP deposition method, microelectrodes are first fabricated, then a droplet of the CNT suspension is dropped between the microelectrodes and an AC voltage is applied across the two microelectrodes. CNTs will be attracted by the dielectrophoretic force to the electrodes to form connections [37–40]. Although the number of CNTs attracted to the electrodes can be roughly controlled by varying the AC voltage and the concentration of the CNT solution, it is very difficult to deposit a single CNT with this method. As shown in Fig. 1.5, several SWNTs were attracted to bridge the electrodes by DEP force. Hence the DEP deposition method is normally used to fabricate devices with CNT films or CNT bundles.

Nano-Manipulation Method

Another controllable assembly process for fabricating CNT devices is to mechanically manipulate CNTs to bridge the microelectrodes. A single CNT attached at the tip end of an AFM cantilever was manipulated using focused ion beam [48]. But the nanotube has to be metal-coated for manipulation. Hence this technology is not

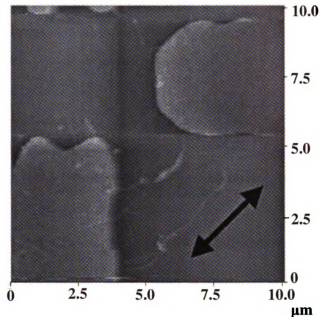


Figure 1.5. The AFM image of two electrodes bridged by several SWNTs which were deposited by DEP process. ([37])

good for building nanoelectronic devices. Three-dimensional manipulation of carbon nanotubes has been studied in [49]. But the manipulation has to be performed under SEM, which limited the applications. A more general way is to manipulate CNTs using the AFM tip such that CNTs can be positioned on substrate surface in a bare environment [50–52]. But all these work limited to manipulating CNTs and none of them built nanoelectronic devices through manipulating CNTs. In this research, we will develop a hybrid fabrication process for building CNT based nanodevices using AFM manipulation and DEP deposition systems.

The AFM, or scanning force microscope (SFM) was invented in 1986 by Binnig, Quate and Gerber [53]. Fig. 1.6 shows the schematic diagram of a head scanning AFM system. Like all other scanning probe microscopes, the AFM utilizes a sharp probe moving over the surface of a sample in a raster scan. In the case of the AFM, the probe is a tip at the end of a cantilever which bends in response to the force

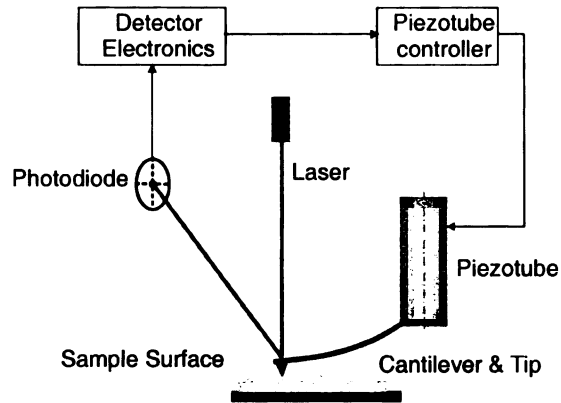


Figure 1.6. Schematic diagram of a head scanning AFM.

between the tip and the sample. The surface topography is acquired by recording the bending of the cantilever at each sampling point.

AFM has already been used to study the supermicroscopic structures of objects that could not be viewed with the Scanning Tunneling Microscope (STM). It is especially widely used to observe living cells, DNA molecules and some other biological objects. Structures of DNA are observed and analyzed using AFM in [54–57]. Membranes and proteins are inspected in [58–60]. The possibility of AFM to be operated **under** physiological conditions, without submitting the sample to fixation or any other **chemical** preparation, allowed its use on the observation of living cells [61, 62]. **Under** appropriate experimental conditions, these cells remained viable during extensive **periods** of time, without damages caused by the scanning.

AFM has also been used to measure nanomechanical properties of biological **samples**, such as elasticity, adhesion, rigidity, friction or viscosity. Some of these **properties** are measured using force vs. distance plots or force vs. time plots. In these **methodologies**, the AFM does not carry out any kind of scanning, measuring only the **interactions** between the tip and the surface of the sample. The improvement of the **studies** using force vs. distance plots lead to the creation of a new experimental **possibility**, named single-molecule force spectroscopy (SMFS) [63]. In order to measure

the interface, the partners in the molecular reaction have to be immobilized onto the surface and the probe. So functionalized tips are used in order to bind easily to the molecular under evaluation. The sample is analyzed following a scanning pattern similar to tapping mode, until the formation of the bond. Then it becomes possible to measure and interpret the force necessary to break the bond or to modify the conformation of a molecule simultaneously bound to the substrate and to the tip. Microbial cell surfaces can show important lateral variations in composition and physical properties. Spatially resolved AFM force spectroscopy, combined with topographic imaging, is emerging as a valuable technique to map such physical heterogeneities. For instance, cell surface charges are mapped using chemically functionalized probes [64].

Through the optimization of the scanning conditions, the tip of the microscope can be used, not only as a probe, but also as a tool for sample manipulation, allowing its cut, dragging, dissection or conformational alteration. For example, S. Nishida, Y. Funabashi and A. Ikai use the AFM tip to do the cell injection and verify the injection results with a total internal reflection fluorescence microscope (TIRFM) [65]. The AFM tip is also employed to dissect chromosomes in [66].

AFM [53] is primarily a tool for characterizing surface topography, but there is also **a** strong interest in using AFM as a nanomanipulator to modify the sample surfaces **or** manipulate nanostructures such as nanoparticles and nanowires on surfaces. Fig. 1.7 shows the possible mechanical manipulation tasks using an AFM probe [67].

Many research groups have been working on AFM based nanomanipulation [68–80]. Some of them are trying to utilize the haptic devices to facilitate the **nanomanipulation** [74,77–79,81]. However, even with the assistance of the haptic devices, the **efficiency** and accuracy of AFM based nanomanipulation is still a major issue due to **the nonlinearities** and uncertainties in nanomanipulation operations. The **compensation of drift**, creep, hysteresis and some other nonlinearities generating large spatial **uncertainties** has been studied by some research groups [80]. The compensation of

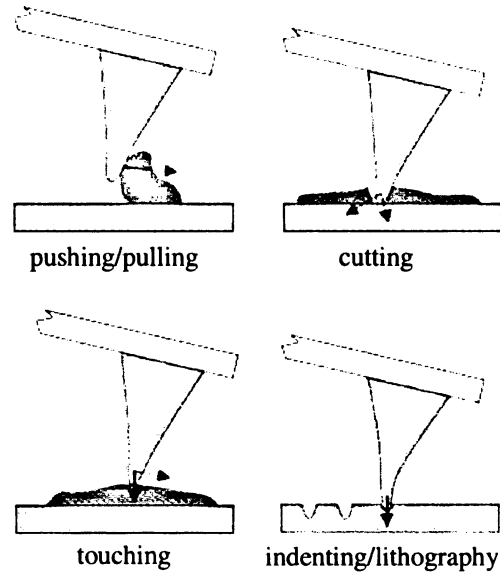


Figure 1.7. Possible mechanical manipulation tasks using an AFM probe. ([67])

these uncertainties does help to improve the accuracy of nanomanipulation to a certain extent, but there are still some other important factors that affect the accuracy of manipulation significantly. The deformation of the cantilever is one of the major nonlinearities that affect the tip position accuracy during manipulation. It is difficult to control the tip position accurately due to the uncertainty of the deformation. Therefore, it is necessary to take the deformation into consideration or find some way to eliminate the deformation. Obviously, a rigid cantilever reduces the deformation significantly if its spring constant is large enough. Unfortunately, as the deformation is reduced, the feedback signal measured from the deformation is also reduced. Because the feedback signal is very important for closed-loop haptic nanomanipulation, it is in a dilemma whether to use a soft cantilever or a rigid one for nanomanipulation.

Fortunately, the invention of the active AFM probe [82–84] provides a promising way to solve this problem by actively changing the nominal rigidity of the cantilever. The cantilever can be controlled to be rigid and maintain its straight shape, and

thus the deformation of the cantilever is eliminated during manipulation. At the same time, the control signal is used to represent the interaction force, which can not be measured by a rigid cantilever only. Hence, the active probe can be used to improve the accuracy of nanomanipulation and the force sensitivity of the haptic nanomanipulation system simultaneously. Since the cantilever keeps straight during manipulation and is adaptable to different sized objects, it is called adaptable end effector in this research.

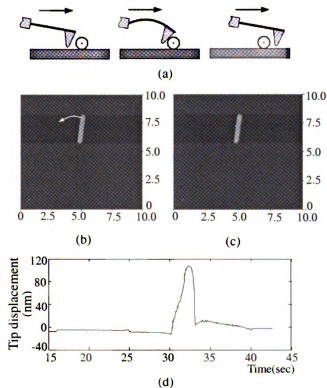


Figure 1.8. Pushing a silver nanowire with an unpreloaded traditional tip ($k=0.57\text{N/m}$). (a) Schematic illustration of the pushing process. (b) The AFM image of a silver nanowire with length of $2.5\mu\text{m}$ and diameter of 120nm . The scanning range is $10\mu\text{m} \times 10\mu\text{m}$. (c) The AFM image by a new scan after pushing. (d) Tip displacement signal measured by the photodiode sensor.

A soft cantilever can provide sensitive force feeling while pushing nano-objects, but on the other hand, the tip is very easy to slip over the nano-objects due to the

flexibility of the cantilever and makes the nanomanipulation inefficient. Fig. 1.8. (a) schematically shows the process of pushing a nano-object using an unpreloaded soft traditional tip. Since there is no preload, the tip floats on the surface during manipulation. As shown in the figure, the cantilever starts to bend after hitting the object and the bending will increase with the tip moving ahead. Finally, the big bending causes the tip to slip over the object. Experimental results from Fig.1.8. (b) to (d) verified these analysis. Fig. 1.8. (b) shows an AFM image of a silver nanowire with length of $2.5 \mu m$ and diameter of 120nm. A silicon nitride probe with a spring constant of 0.57 N/m is used to push the nanowire following the trajectory indicated by the arrow without preload. Fig. 1.8. (c) shows the image from a new AFM scan after manipulation. It can be seen that the manipulation failed and the nanowire is still in its original position. From Fig. 1.8. (d), which shows the photodiode output (deflection signal), it can be seen that the tip slipped over the nanowire while pushing.

The traditional way to overcome the tip slipping over the nano-objects, is to apply a preloaded normal force on the tip to keep the tip contacting the surface. Fig. 1.9. (a) schematically shows the process of pushing a nano-object using a preloaded traditional tip. As shown in the figure, the cantilever has a large bending even before touching the object due to the preloaded force. This large bending makes the tip scratch over the surface and thus avoid slipping over the object. However, since the preloaded force is much stronger than the interaction force, the shape of the cantilever dose not change much during pushing the object. Therefore, it is difficult to get sensitive force information from the deflection of the cantilever. Experimental results from Fig. 1.9. (b) to (d) verified the above analysis. The same tip used in the last experiment is used here to push the same nanowire again. Fig. 1.9. (c) shows the image from a new AFM scan after manipulation. It is observed that the nanowire is pushed away successfully. Fig. 1.9. (d) shows the deflection signal during manipulation. The silicon nitride

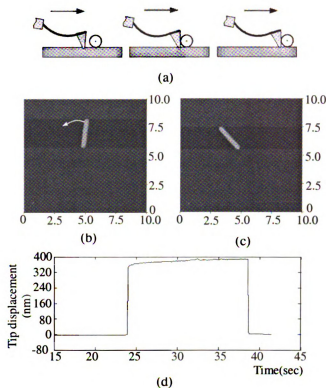


Figure 1.9. Pushing a silver nanowire with a preloaded traditional tip ($k=1.5\text{N/m}$). (a) Schematic illustration of the pushing process. (b) The AFM image of a silver nanowire with length of $2.5\mu\text{m}$ and diameter of 120nm . The scanning range is $10\mu\text{m} \times 10\mu\text{m}$. (c) The AFM image by a new scan after pushing. (d) Tip displacement signal measured by the photodiode sensor.

probe was preloaded and stuck on the surface at $t = 24\text{sec}$, and then moved toward **the rod**. At $t = 33\text{sec}$, the tip touched the nanowire and began to push it. Obviously, **the preloaded force** almost saturates the photodiode output and the interaction force **is unobservable**. It becomes very difficult to feel the actual tip-object interaction force **in this situation**. Consequently, it also becomes very difficult to precisely control the **tip position** in the lateral direction during manipulation because the preloaded force **not only** causes the cantilever to bend in the normal direction but also causes the tip **to move** in the lateral direction [78]. Furthermore, the preloaded force will wear out **the tip** quickly and cause contamination easily.

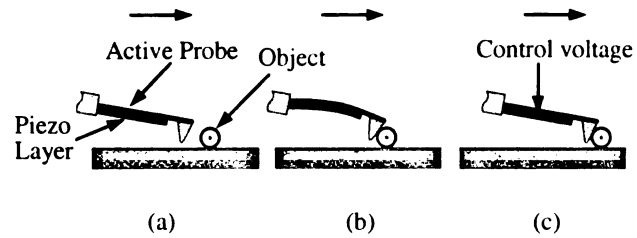


Figure 1.10. Schematic illustration of pushing a nano-object using the adaptable end effector.

Fortunately, these problems can be solved using the active probe (spring constant $k = 1-5 \text{ N/m}$) as an adaptable end effector for AFM based nanomanipulation. The adaptable end effector can be controlled to behave like a rigid cantilever, at the same time, the control signal, which is sensitive to the interaction force, can be used to reconstruct the force information for better haptic force feedback. Fig. 1.10 shows how an adaptable end effector works during pushing a nano-object. In Fig. 1.10. (a), the adaptable end effector moves toward the object in straight shape; In Fig. 1.10. (b), the effector touches the object and is bent by the interaction force; In Fig. 1.10. (c), a control voltage is applied to the piezo layer of the end effector to eliminate the bending caused by the interaction force. The cantilever backs to its straight shape and the object is pushed away.

It has to be mentioned that AFM probe needs to push the nano-objects in any **random** direction. When pushing direction is not in parallel with the direction of **cantilever**, the manipulation force will not only cause the cantilever to bend in normal **direction**, but also cause the cantilever to twist around the axis of the cantilever [85]. **Since** the cantilever is quite rigid in twisting mode, the twisting force will not be able to **twist** the cantilever much and affect the accuracy of manipulation. Therefore, it is not **necessary** to actively control the twisting. The only difficulty brought by the twisting **is that** the twisting signal is very difficult to measure. For the nanomanipulation **using a** soft traditional probe, a preload is needed to press the tip on the surface. The

preload causes huge friction force between tip and surface. Since the friction force will submerge the twisting force and the deflection force caused by objects during manipulation, the measured twisting signal is very noisy. In the nanomanipulation system using active probe, the control signal represents the deflection force, and the twisting signal from the photodiode represents the twisting force. Since the cantilever is controlled to keep straight and stay above the surface, the friction force between tip and sample surface is reduced significantly. Hence, the twisting force caused by manipulation can be easily measured.

In this research, an active AFM probe is used as an adaptable end effector for the AFM based nanomanipulation system. In order to actively control the flexible adaptable end effector, the mathematical model of the probe is required. Since the cantilever of the adaptable end effector is flexible and a distributed parameter system, it is modeled using the Euler-Bernoulli beam model [86], which has been widely studied to control flexible manipulators [87–91].

The Euler-Bernoulli equation governs the transverse vibration of a flexible beam. Consider the beam shown in Fig. 1.11(a), which undergoes transverse vibrations. since the width of the beam is much more significant than the thickness, the strain **a**long the width of the beam can be assumed to zero. Thus only transverse vibrations **o**f the beam will be analyzed and the torsional effects are ignored. To analyze the **d**ynamics of the beam, a small segment of this beam with length dx , at position x , **i**s **c**hopped out. The transverse deflection of the beam at position x and time t is **d**enoted by $w(x, t)$. The segment is subjected to a shearing force, $V(x)$, and a bending **m**oment, $M(x)$. On the opposite side of this segment, which corresponds to a position $x + dx$, the shearing force is $V(x + dx) = V(x) + \partial V/\partial x dx$. Likewise the moment **f**orce at the position $x + dx$ is $M(x + dx) = M(x) + \partial M/\partial x dx$. This is illustrated **i**n **F**ig. 1.11(b) where the term $\rho A dx \partial^2 w/\partial t^2$ is an inertial force, and ρ is the mass **d**ensity.

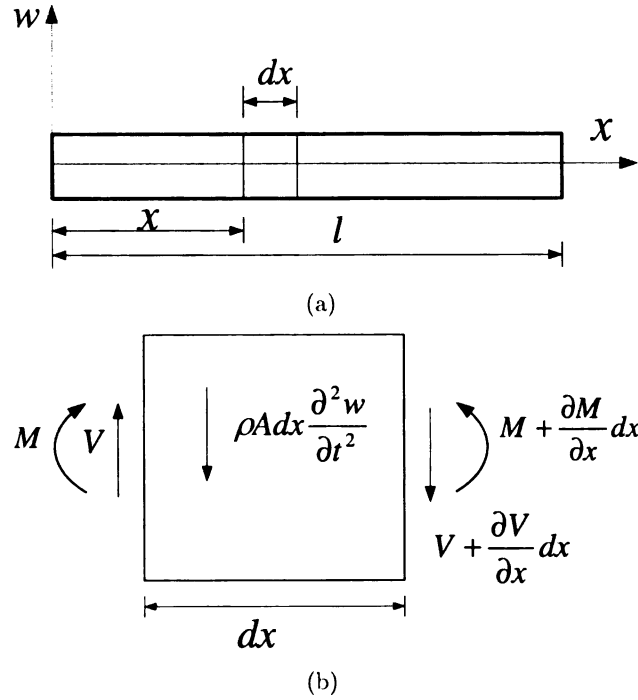


Figure 1.11. Flexible beam

The forces equilibrium condition in Fig. 1.11(b) gives,

$$V - \left(V + \frac{\partial V}{\partial x} dx\right) - \rho A dx \frac{\partial^2 w}{\partial t^2} = 0 \quad (1.3)$$

The moment equilibrium condition gives,

$$-V dx + \frac{\partial M}{\partial x} dx = 0 \quad (1.4)$$

The bending moment M is given as [86]

$$M = EI \frac{\partial^2 w}{\partial x^2} \quad (1.5)$$

Substituting (1.4) and (1.5) into (1.3) gives the Euler-Bernoulli equation [86];

$$EI \frac{\partial^4 w}{\partial x^4} + \rho A \frac{\partial^2 w}{\partial t^2} = 0 \quad (1.6)$$

1.2.4 Testing of CNT Infrared Sensors

The photoconductivity of CNTs has been extensively studied and different optoelectronic properties of CNTs has been tested and reported in the fields of Raman scattering [7], CNT light absorption [92–95], photoinduced molecular desorption [8, 96], fluorescence [95, 97], and electroluminescence [98]. The photoconductivity properties of CNTs have also been studied in various laboratories. As shown in Fig. 1.12, the temporal photocurrent response and the dependence of the photocurrent on the IR light intensity were studied in [9–11, 13, 33]. Moreover, as shown in Fig.1.13, the dependence of the photocurrent on the gate voltage has also been studied in [13].

So far most of the reported work focuses on studying the photoconductivity of CNTs, but few work has been done to study the photovoltaic effect of CNTs. Since a photovoltaic device is much more sensitive and has faster response speed than a photoconducting device, it is very important to study the photovoltaic effect of CNTs. More importantly, CNT based nanophotodiodes have the potential to be nanogenerators for driving nanodevices. As shown in Fig. 1.2, a p-n junction is created in a single CNT to form a p-n junction photodiode [14], and the I-V characteristic curves with different incident light intensity were measured. But since two bottom gates are needed in the device, it brings difficulties in fabricating such device in nanoscale. Hence it is necessary to further explore the photovoltaic effect of CNTs and develop a simpler design. It has been theoretically and experimentally proven that the CNT-metal contacts play an important role in the performance of CNT devices [41, 42, 99–103]. But few researchers studied the dependence of CNT photo-

behavior on the CNT-metal contact conditions. Thus the CNT-metal contact will be another study focus in this research.

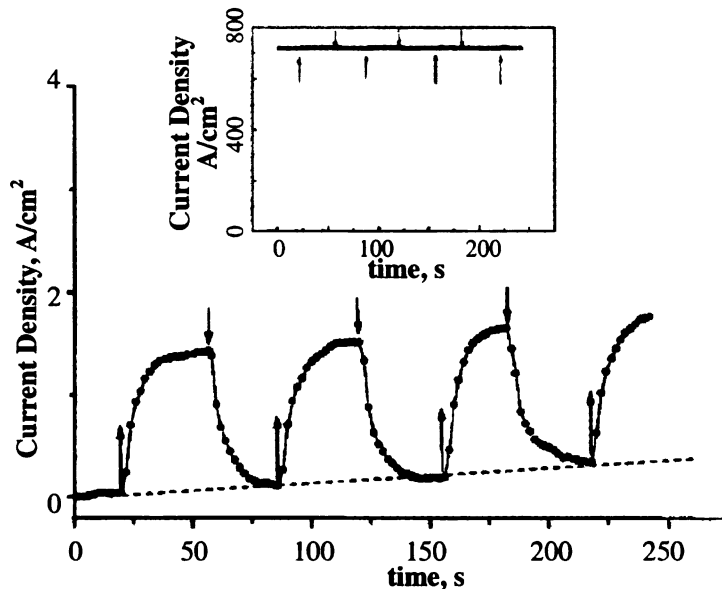


Figure 1.12. Temporal photocurrent response of a SWNT film. ([10])

In this research, we will focus on studying both photovoltaic and photoconducting properties of single SWNTs and MWNTs. Experimental testings on the temporal photoresponse and the I-V characteristic curves with different incident light intensity will be performed. Furthermore, the dependence of CNT's photobehavior on temperature, and the dependence of photocurrent on CNT-metal contact will also be studied. Multi-pixel CNT IR sensor array and multicolor CNT IR sensor will also be fabricated and tested.

1.3 Objectives and Challenges

The objective of this research is to develop single CNT based IR sensors including single pixel sensors, multi-pixel sensor arrays and multicolor sensors. The development involves not only the theoretical design of CNT IR sensors, but also

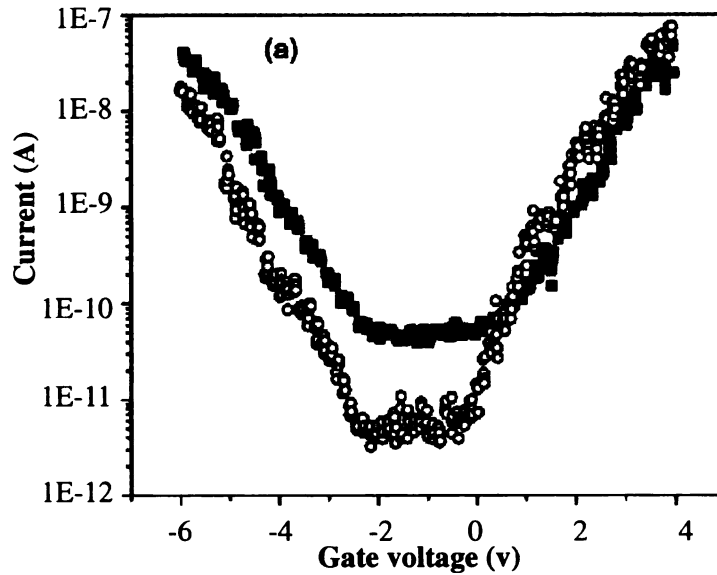


Figure 1.13. Gating characteristics of an ambipolar NT-FET with and without infrared illumination ([13])

experimental manufacturing and testing of CNT IR sensors. Though some work has been reported to study the photoconductivity of CNTs, the quantum efficiency is still too low and the fabrication process is inefficient and unreliable. And the multi-pixel CNT IR sensor and multicolor CNT IR sensor have not been demonstrated.

The main challenges involved in this research include:

- A well designed CNT IR sensor. Since the impedance of CNTs (especially semiconducting CNTs) can be up to giga- or tera-Ohms in general, the current signal will be very small. How to increase the photocurrent signal and effectively read it out are the main difficulties to consider during the design of the CNT sensors.
- An efficient and reliable nanomanufacturing process. Since a single CNT is desired to bridge the microelectrodes, the most difficult work in this research is how to deposit only one CNT onto the microelectrodes in an efficient and

controllable manner. There are some methods available to fabricate a single CNT based nanodevice. But there is no a solution to fabricate single CNT based nanodevice arrays at present.

- CNTs with appropriate bandgaps for MIR detection. One of the objectives of this research is to detect MIR using CNT sensors. Since most SWNTs have very thin diameters and large bandgaps, and most MWNTs have very large diameters and are metallic, it will be a challenge to get a CNT with an appropriate bandgap for MIR detection.

1.4 Organization of Dissertation

Design of the CNT based IR sensors is presented in Chapter 2, where the structures of the CNT sensors are discussed. Following the discussion of the design, the fabrication and assembly process for building single CNT based nanodevices is developed in Chapter 3. First the fabrication process is addressed. Then the key technology for assembling single CNT devices, the AFM based nanomanipulation system enhanced by an adaptable end effector, is developed and experimentally verified. After that, experiments are carried out to fabricate single CNT based IR sensors to show the efficiency of the developed fabrication process. After describing the fabrication and assembly process in Chapter 3, experimental testings of the fabricated CNT sensors are discussed in Chapter 4, where the performance of the single CNT based IR sensors are also evaluated and analyzed. Chapter 5 reports the fabrication and testing of multi-pixel CNT sensor array and multicolor CNT sensor. Finally, a summary of the developed methodologies and our contributions are provided in Chapters 6.

CHAPTER 2

Design of Carbon Nanotube based Infrared Sensors

The challenges of designing single CNT based infrared sensors lie in two aspects, the fabrication and the testing. Since the diameter of a CNT can be as small as sub-nanometer, the design of the sensor structure is essential for the fabrication process. An appropriate design can make it easier to assemble a single CNT onto the microelectrodes. Another challenge is how to improve the performance of the CNT sensors. Since the impedance of CNTs (especially semiconducting CNTs) is very huge in general, the current signal will be very small. How to increase the photocurrent signal and effectively read it out are the main difficulties to consider during the design of the CNT sensors.

2.1 Manufacturing Issues in Design

The structure of single CNT based IR sensor is shown in Fig. 2.1(a). It consists of two microelectrodes separated by a small gap and bridged by a single CNT. Fig. 2.1(b) shows the cross section of the microelectrodes. Since the CNT will be pushed onto the microelectrodes by AFM tip, a slope at the edge of the microelectrodes is necessary.

Fig. 2.2 illustrates pushing CNT onto the microelectrodes with different step profiles which are generated by different fabrication processes. CNT can easily be pushed onto the microelectrodes which are fabricated by lift off process rather than etching process. The CNT may get stuck at the edge of the microelectrode and cannot be pushed up onto the microelectrodes as shown in Fig. 2.2(a). Moreover, to make it easier to push CNTs onto the microelectrodes, the thickness of the microelectrodes has to be as thin as possible. Here the microelectrode is designed to be 30 nm thick.

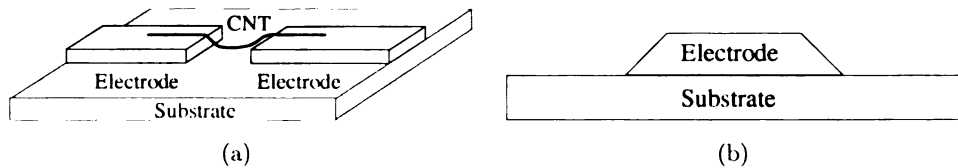


Figure 2.1. (a) Structure of the single CNT based infrared sensor. (b) Cross section of the microelectrodes.

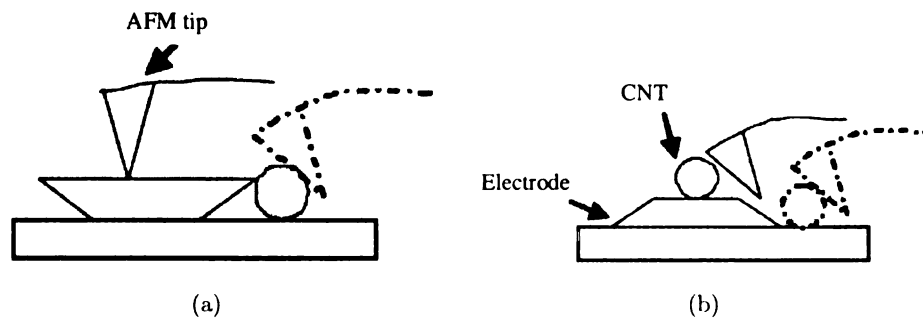


Figure 2.2. Illustrations of pushing CNT over the microelectrodes which are fabricated by (a) etching and (b) lift off process.

2.2 Diode based CNT Sensor

A semiconducting CNT can work as a photoconductor or a photodiode for photo detection. Due to its high dark current and big noise, a photoconductor normally has

a lower sensitivity than a photodiode. Therefore, a carbon nanotube Schottky diode will be designed for the infrared detection. Fig. 2.3 shows the energy band diagrams of the CNT-metal contact for n-type and p-type CNTs respectively. For n-type CNTs, a Schottky barrier is formed at the CNT-metal interface when $\phi_M > X_{CNT}$, where ϕ_M is the work function of the metal electrode, and X_{CNT} is the electron affinity of CNT. For p-type CNTs, a Schottky barrier is formed at the CNT-metal interface when $\phi_M < X_{CNT} + E_g$, where E_g is the bandgap of CNT. Since semiconducting CNTs normally are p-type in air due to the oxygen doping, the case of Fig. 2.3(b) is considered in this research. As shown in Fig. 2.3(b), there is a Schottky barrier at the CNT-metal interface which blocks the transportation of holes.

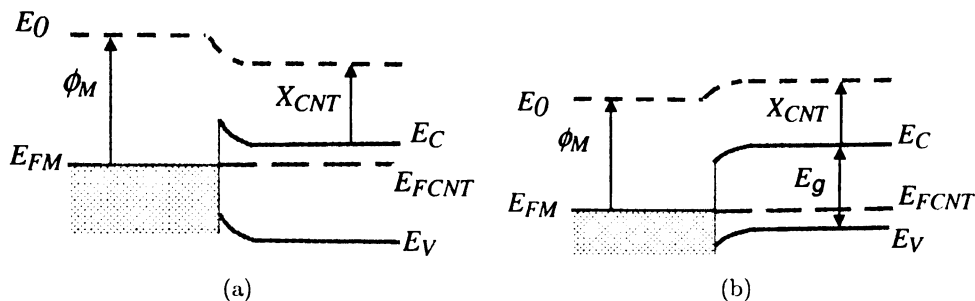


Figure 2.3. The energy band diagrams of the CNT-metal contact for (a) n-type CNTs and (b) p-type CNTs.

2.3 Optimizing the CNT Sensor

By choosing metals with different work functions as the microelectrodes, we can adjust the Schottky barrier at the CNT-metal interface. Two different designs are developed in this research to study the dependence of the photocurrent on the CNT-metal contact conditions. Fig. 2.4 shows the structure and the energy band diagram of CNT sensors with symmetric contacts, where both of the microelectrodes are made from a same material. As infrared photons hits the SWNT, the photons with energy

bigger than the band gap will excite electrons and holes inside the CNT to form electron-hole pairs. The electron-hole pairs will be separated by an external electrical field or the built-in field and contribute to the photocurrent. Since there is no built-in field outside the depletion regions, the electron-hole pairs will recombine quickly and do not contribute to the photocurrent. Only the electron-hole pairs generated at the depletion regions can form photocurrent. Hence, the total photocurrent under zero bias is calculated by $I_v = I_{v1} + I_{v2} = i_{h1} - i_{h2}$. As shown in Fig. 2.4(b), the holes generated at one Schottky barrier have to tunnel through another Schottky barrier to form a current. This significantly limits the magnitude of the photocurrents I_{v1} and I_{v2} . Moreover, since the CNT-metal contacts are symmetric, I_{v1} is very close to I_{v2} if the incident IR power intensity is same on the both electrodes. Thus the total photocurrent will be very small and becomes difficult to measure.

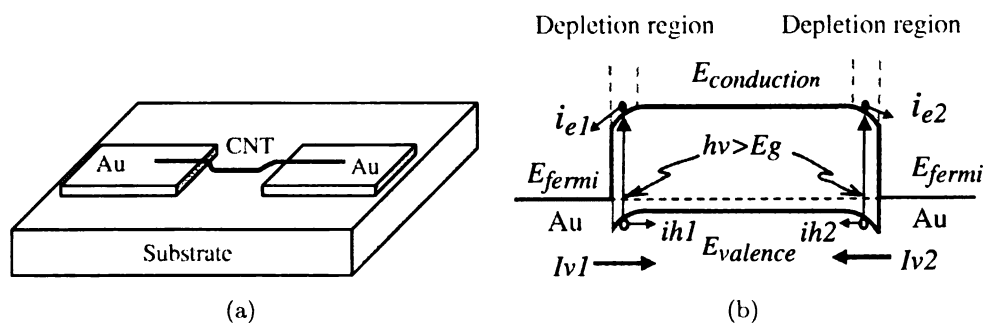


Figure 2.4. The single CNT based infrared sensors with symmetric contacts. (a) Structure of the CNT sensors. (b) Energy band diagram of the CNT sensors.

Fig. 2.5 shows the structure and the energy band diagram of CNT sensors with asymmetric contacts. By using different materials as the contact electrodes, asymmetric CNT-metal contacts are created to maximize the total photocurrent I_v . By lowering one of the Schottky barrier, the photogenerated holes at another barrier will be able to tunnel through this barrier easier. Thus the total photocurrent will be increased. Moreover, the total photocurrent will also be increased by enlarging the

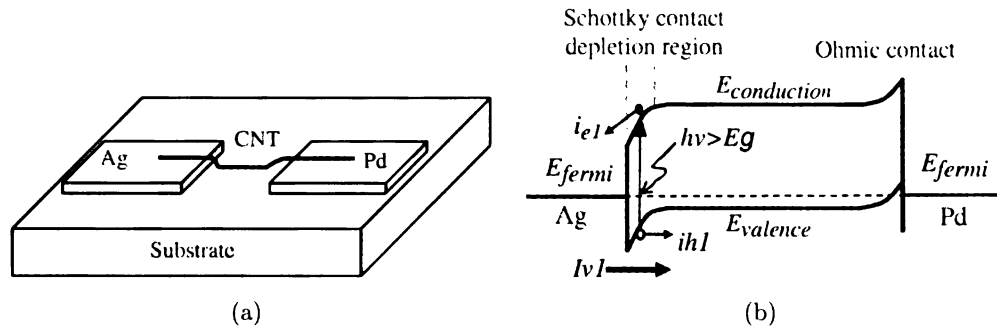


Figure 2.5. The single CNT based infrared sensors with asymmetric contacts. (a) Structure of the CNT sensors. (b) Energy band diagram of the CNT sensors.

difference between the photocurrents generated at the two barriers due to the asymmetry of the CNT-metal contacts. For example, as shown in Fig. 2.5(b), since many people have reported that Pd is the best materials to form an Ohmic CNT-metal contact [41,104], when silver (Ag) and palladium (Pd) are used as the contact materials, a Schottky contact is formed at the CNT-Ag interface and an Ohmic contact is formed at the CNT-Pd interface. In this way, the photocurrent $I_{v2} = 0$ and the total photocurrent I_v is maximized to I_{v1} . With the asymmetric CNT-metal contacts, the sensitivity and other performance of individual SWNT based IR detectors are expected to be further improved.

2.4 Chapter Summary

Design of the single CNT based infrared sensors is discussed in this chapter. Single CNT based Schottky photodiodes have been designed for infrared sensing. The shape of the microelectrode was specially designed for pushing CNT onto the microelectrodes. Structures with symmetric and asymmetric contacts have also been designed for studying the dependence of photocurrent on the CNT-metal contact conditions.

CHAPTER 3

Assembly of Carbon Nanotube based Infrared Sensors

Since a single CNT is desired to bridge the microelectrodes, the most difficult work in this research is how to deposit only one CNT onto the microelectrodes. As discussed in Chapter 1, the directly growth method cannot guarantee only growing one CNT between the microelectrodes, and the DEP deposition method normally brings multiple CNTs to the electrodes. Although the EBL fabrication method is able to form single CNT devices, the position of the CNT/device cannot be controlled, and the efficiency is low. AFM manipulation can position CNTs on the substrate surface, but the CNTs to be manipulated have to be close to the microelectrodes. Combining the advantages of DEP deposition and AFM manipulation, a nanomanufacturing process with which a single CNT can be manipulated to bridge a pair of microelectrodes was developed. The DEP method is used to trap one or several individual CNTs around the microelectrodes, then AFM is used to manipulate one of the CNTs to make connections with the microelectrodes and clean the rest CNTs away from the microelectrodes.

3.1 Development of the Fabrication Process for Single CNT based Nano-Devices

The structure of the individual CNT based IR sensor is shown in Fig. 3.1(a). A CNT IR sensor is composed of a pair of electrodes and a single CNT. Sensors are fabricated using standard photolithography process and AFM lithography process. An array of gold micro electrodes is fabricated on a substrate with the process shown in Fig. 3.1(b). After the connected electrodes are fabricated with the process of Fig. 3.1(b), as shown in Fig. 3.1(a), the AFM based nanomanipulation system is used to create a small gap with distance of 0.5 - 2 μm across the two electrodes. With the AFM system, the gap can be easily created and the width of gap can be controlled to vary from several tens of nanometers to several micrometers.

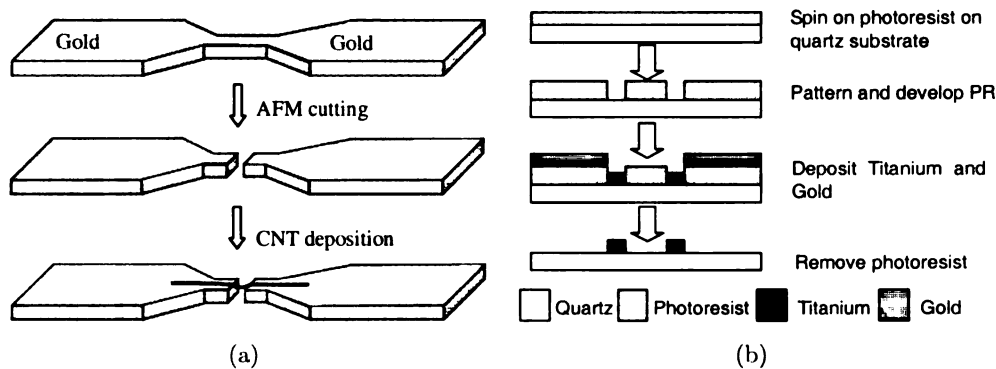


Figure 3.1. (a) The CNT assembly process. (b) The fabrication process of micro electrodes.

The MWNT in our experiments are obtained from Shenyang National Laboratory (SYNL) for Materials Science, China. It takes several steps to deposit an individual CNT onto the substrate. Fig. 3.2 shows the flow chart of the CNT deposition process. Firstly, the powdery CNTs are put into acetone and dispersed by ultrasonicator for 10-15 min to form CNT suspension. The concentration of CNTs in acetone is experi-

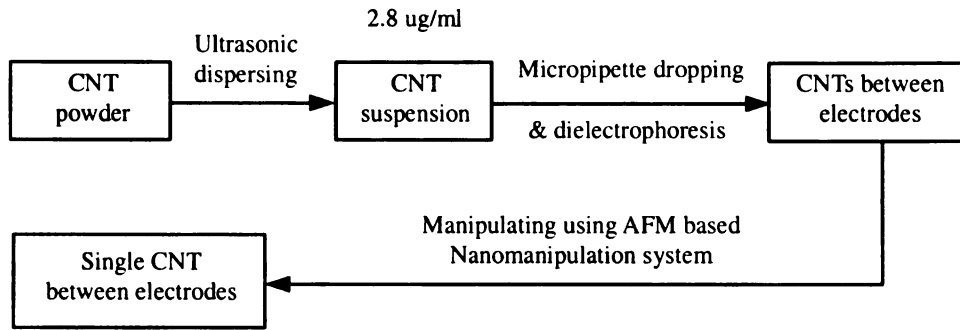


Figure 3.2. The CNT deposition process.

mentally optimized to $2.8 \mu\text{g/ml}$. Then a drop of $5 - 10 \mu\text{l}$ of the CNT suspension is dropped onto the substrate between the two electrodes. At the same time, a sine wave ac signal with the frequency of 10 kHz and the peak to peak amplitude of 1.5 to 2 V is applied between the two electrodes for several seconds. The dielectrophoresis force traps CNTs to the electrodes. Finally, the acetone on the substrate is evaporated. In the deposition process, the concentration of the CNT suspension, the frequency and the amplitude of ac signal are experimentally optimized to get the highest possibility to trap an individual CNT between the two electrodes. Even with those parameters experimentally optimized, it can not be guaranteed that only one CNT is trapped between the two electrodes and bridges them successfully. Normally, there are always some impurities or more than one CNT trapped between the electrodes. Furthermore, if only one CNT was successfully trapped between the electrodes, it might not connect the electrodes very well. Therefore, it is necessary to take another step to clean up the detector area and adjust the position of the CNT to make a connection. This final step is very critical and is called CNT assembly. An AFM based nanomanipulation system was developed to performe the CNT assembly.

3.2 Development of the AFM based Nanomanipulation System

The AFM based nano-robotic manipulation system with the augmented reality interface can provide the operator with real-time visual display and force feedback during nanomanipulation [77–79]. It consists of three subsystems: the AFM system, the augmented reality interface, and the real-time adaptable end effector controller.

As shown in Fig. 3.3, the AFM system includes the AFM head, signal access module (SAM), AFM controller, and the main computer. The SAM provides interfaces among the AFM head, AFM controller, and other devices. The AFM controller controls the AFM head through the SAM. It also connects to the main computer, which is responsible for running main control program and providing an interface for the imaging. The augmented reality interface consists of a haptic device and a nanomanipulation program running on a Windows PC. The nanomanipulation program provides an interactive interface for users. During manipulation, operators use the haptic device to input the tip position command and feel the real-time interaction force between the tip and the nano-objects. The real-time visual display is dynamic AFM images locally updated in video frame rate. The augmented reality interface also sends tip position command to the main computer. The real-time adaptable end effector controller subsystem includes a real-time linux system and a DAQ card. The adaptable end effector controller running in the real-time linux samples deflection signal of the cantilever through DAQ card and then outputs control signal to the adaptable end effector. At the same time, the control signal is also rendered to the haptic device to display the interaction force. These three subsystems communicate with each other through the Ethernet.

Fig. 3.4 shows the details of the control scheme of the nanomanipulation system using the adaptable end effector. The operating environment sends position command

to the AFM controller which controls the tip position. An active probe is used as the adaptable end effector and a control loop is introduced into the system to keep the adaptable end effector rigid during manipulation. During pushing, the adaptable end effector is controlled to keep straight by feeding back the deflection signal from the photodiode detector. At the same time, the control signal is also sent to the haptic device (*PhantomTM*) as a force signal through the operating environment.

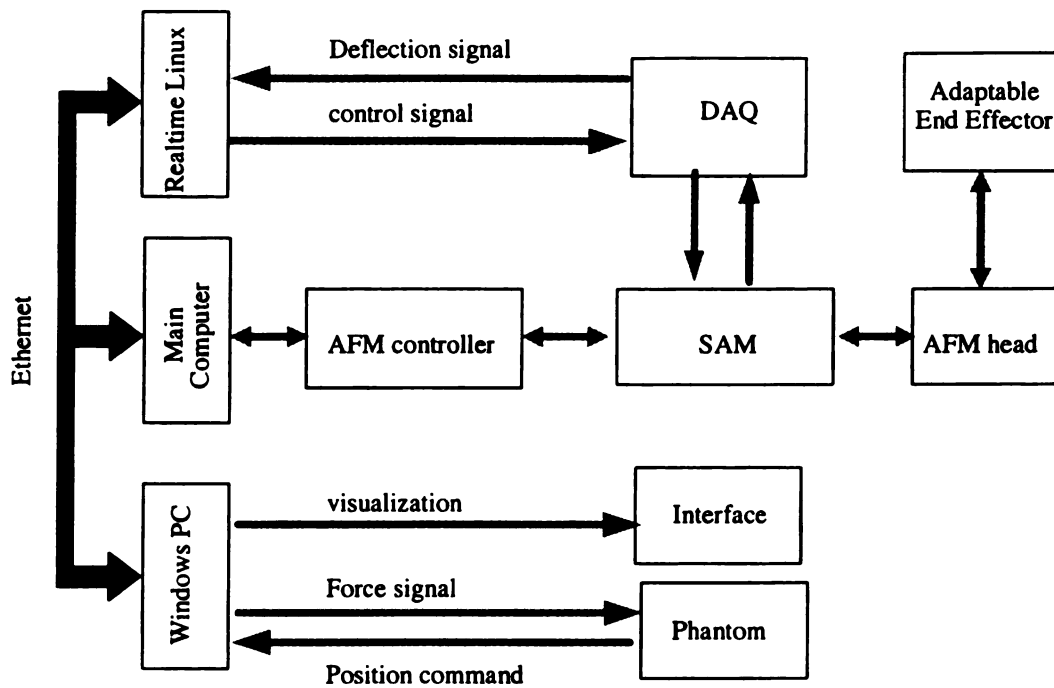


Figure 3.3. The setup of the AFM based nanomanipulation system using adaptable end effector.

3.2.1 Modeling of Adaptable End Effector

As shown in Fig. 3.5, the active probe is a MEMS device, micromachined from bulk silicon with a Zinc Oxide piezoelectric film patterned along a portion of a micro-

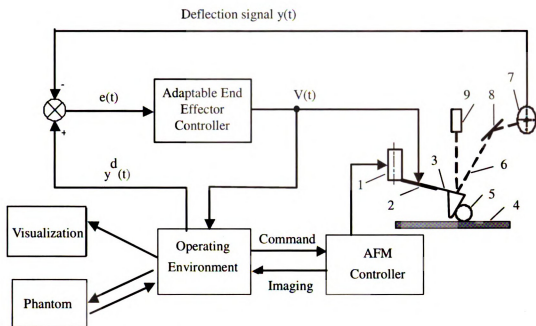


Figure 3.4. The control scheme of the AFM based nanomanipulation system using adaptable end effector. 1: Piezo tube. 2: Piezoceramic layer of the adaptable end effector. 3: Adaptable end effector. 4: Substrate surface. 5: Object. 6: Laser beam. 7: Quad-photodiode detector. 8: Mirror. 9: Laser gun.

cantilever [105]. The Active Probe was originally developed to improve the tapping mode imaging rate by dynamically mediating the resonant vibration of the AFM probe (Tapping Mode) while simultaneously positioning it vertically to track the sample topography [83, 84]. However, in this research, the active probe will be modelled as an adaptable end effector of the AFM based nanomanipulators.

It can be observed from Fig. 3.5 that the foremost Si part does not have ZnO layer bonded. Since the spring constant of a cantilever is in inverse proportion to the cube of the length of the cantilever, the Si part is even a little bit more rigid than the ZnO/Si part. The calculated spring constants of the Si part and ZnO/Si part are 76.1N/m and 71.3N/m respectively. Furthermore, when a force is applied



Figure 3.5. Adaptable end effector with an integrated Zinc Oxide piezoelectric actuator.

on the free end of a flexible beam, the beam has large deformation at the fixed end and little deformation near the free end. Therefore, the interaction force applied on the tip will cause the ZnO/Si part to deform more and cause less deformation on the Si part. Since the Si part is quite rigid, by controlling the shape of the ZnO/Si part, the stiffness of the cantilever can be controlled to change in the range of $1 - 76N/m$.

A sketch of the adaptable end effector is shown in Fig. 3.6. Since the width of the cantilever is much more significant than the thickness, the strain along the width of the cantilever can be assumed to be zero. Thus only transverse vibrations of the beam will be analyzed. The cantilever will be analyzed as two parts, Part I ($0 \leq x \leq l_1$) and Part II ($l_1 \leq x \leq L$). For all variables in this research, a superscript I indicates Part I, while a superscript II indicates Part II. Similarly, subscript b and p refers to the silicon beam layer and the piezoceramic layer respectively. For example, $(EI)^I$ is the effective bending stiffness of Part I, and $(EI)^{II}$ is the effective bending stiffness of Part II; E_b is the Young's modulus of the silicon layer, and E_p is the Young's modulus of the piezoceramic layer.

As shown in Fig. 3.6(b), there is a layer of piezoceramic under the silicon cantilever. There are also another two very thin metal layer absent in the figure which are used for electrical connection. The piezoceramic film is sandwiched between these

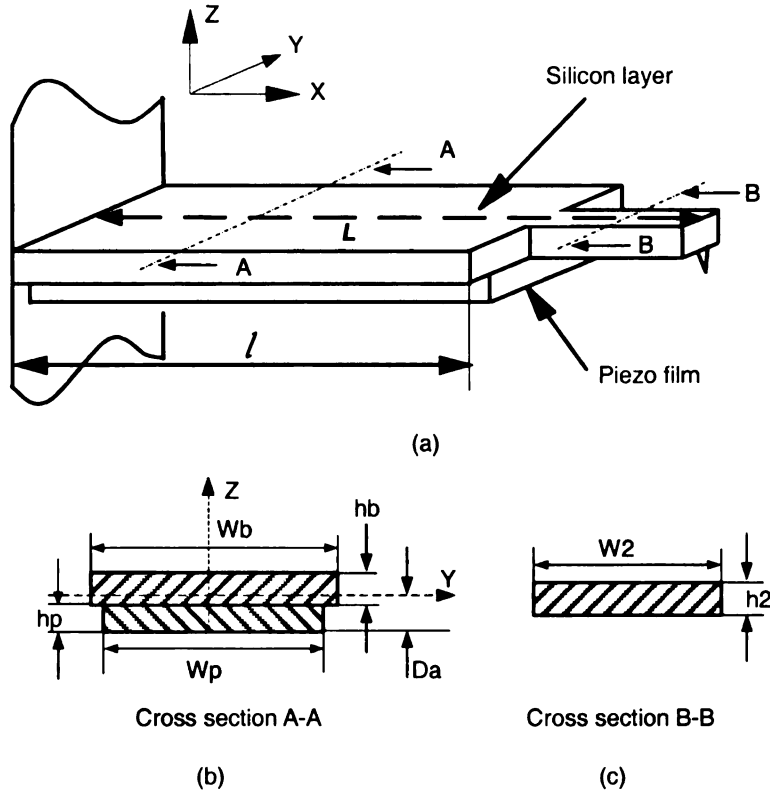


Figure 3.6. Adaptable end effector configuration.

two metal film. By applying a potential between these two metal film, the piezoceramic film is driven to extend or contract along the length of the cantilever. Since these layers are tightly bonded together and the structure is asymmetric in Z direction, extending or contracting the piezoceramic film will cause the whole cantilever to bend up or down.

When an active voltage $V(x, t)$ is applied to the piezoceramic film, the strain ε_a induced in the piezoceramic film is given by [87]:

$$\varepsilon_a(x, t) = V(x, t) \times \frac{d_{31}}{h_p} \quad (3.1)$$

where ε_a is the induced strain in the piezoceramic film, V is the voltage applied on the piezoceramic layer, d_{31} is the appropriate static piezoelectric constant that relates the electric field applied across the piezoceramic layer to the resulted strain, and h_p is the thickness of the piezoceramic layer. Since the piezoceramic layer has uniform geometry along its length, $V(x, t)$ is replaced by $V(t)$ in the following analysis.

The location of the neutral axis at the cross section A-A, as shown in Fig. 3.6(b), is given by:

$$D_a = \frac{E_p h_p^2 W_p + E_b h_b^2 W_b + 2E_b W_b h_b h_p}{2(E_b W_b h_b + E_p W_p h_p)} \quad (3.2)$$

where E is the Young's modulus, h is the thickness of the layers and W is the width of the layers.

Suppose a positive voltage is applied and the cantilever is driven to bend up as shown in Fig. 3.7(a). To analyze the stress inside the cantilever, a small piece of the cantilever with length dx is chopped out, as shown in Fig. 3.7(b). $d\theta$ is the bending angle of this small piece and is given by

$$d\theta = \frac{\partial^2 w(x, t)}{\partial x^2} \quad (3.3)$$

where $w(x, t)$ is the transverse deflection of the cantilever. In the piezoceramic layer, the stress $\sigma_p(x, z, t)$ is given by [106]:

$$\sigma_p(x, z, t) = E_p \cdot [\varepsilon(x, z, t) - \varepsilon_a(x, t)] \quad (3.4)$$

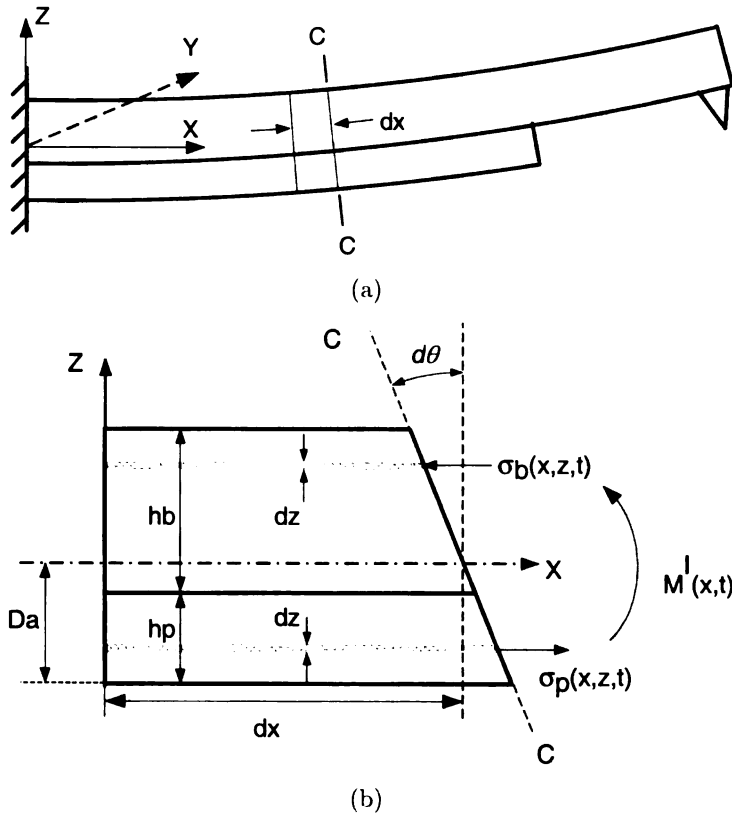


Figure 3.7. Diagram of the cantilever under bending.

where ε is the strain caused by the deflection of the beam and is different for each z position. In the silicon layer, as shown in Fig. 3.7(b), the stress σ_b is given by:

$$\sigma_b(x, z, t) = E_b \cdot \varepsilon(x, z, t) \quad (3.5)$$

At position z , the deformation of the cantilever in the x direction is equal to $d\theta \cdot z$. Then the strain $\varepsilon(x, z, t)$ is

$$\varepsilon(x, z, t) = d\theta \cdot z/dx \quad (3.6)$$

The stress σ_b and σ_p generate two moments M_b and M_p in the cross-section C-C,

which can be calculated as

$$\begin{aligned} M_b &= \sigma_b(x, z, t) \cdot dA \cdot z = \sigma_b(x, z, t) dz W_b z \\ M_p &= \sigma_p(x, z, t) \cdot dA \cdot z = \sigma_p(x, z, t) dz W_p z \end{aligned} \quad (3.7)$$

By integrating these two moments along the z direction, the overall moment $M^I(x, t)$ in the cross-section C-C can be derived as

$$\begin{aligned} M^I(x, t) &= \int_{-D_a}^{-D_a+h_p} \sigma_p(x, t) W_p z dz + \int_{-D_a+h_p}^{-D_a+h_p+h_b} \sigma_b(x, t) W_b z dz \\ &\quad \text{for } 0 \leq x \leq l_1 \end{aligned} \quad (3.8)$$

Substituting (3.1) - (3.7) into (3.8) gives

$$M^I(x, t) = (EI)^I \cdot \frac{\partial^2 w(x, t)}{\partial x^2} - C_a \cdot V(t) \quad (3.9)$$

where $(EI)^I$ is the effective bending stiffness at the section A-A for part I, and C_a is a constant which depends on the geometry and materials of the beam. $(EI)^I$ and C_a are given by

$$(EI)^I(x, t) = E_p W_p h_p \cdot (1/3 * h_p^2 + D_a^2 - h_p D_a) + \\ E_b W_b h_b [\frac{1}{3} h_b^2 + h_p^2 + D_a^2 + h_b h_p - 2h_p D_a - h_b D_a]$$

$$C_a = E_p \cdot d_{31} \cdot W_p \cdot \frac{h_p - 2D_a}{2}$$

On cross section B-B, as shown in Fig. 3.6.c, the moment of part II, M^{II} , can be derived in the same way as M^I . M^{II} is given by

$$M^{II}(x, t) = (EI)^{II} \cdot \frac{\partial^2 w(x, t)}{\partial x^2} \quad (3.10)$$

where $(EI)^{II}$ is the effective bending stiffness at the section B-B and given by

$$(EI)^{II} = E_b W_2 h_2^3 / 12$$

Considering part I ($0 \leq x \leq l_1$) and part II ($l_1 \leq x \leq L$) of the cantilever respectively, and combining (3.9) and (3.10) with a conventional Euler-Bernoulli beam analysis yields the equations of motion for transverse vibrations $w(x, t)$ of the cantilever. The governing equations are

$$\left\{ \begin{array}{l} \frac{\partial^2}{\partial x^2}[(EI)^I \frac{\partial^2 w(x,t)}{\partial x^2} - C_a V(t)] + \rho^I A^I \frac{\partial^2 w(x,t)}{\partial t^2} = 0 \\ \text{for } 0 \leq x \leq l_1 \\ \\ (EI)^{II} \frac{\partial^4 w(x,t)}{\partial x^4} + \rho^{II} A^{II} \frac{\partial^2 w(x,t)}{\partial t^2} = 0 \text{ for } l_1 \leq x \leq L \end{array} \right. \quad (3.11)$$

with the boundary conditions

$$\left\{ \begin{array}{l} w(0, t) = 0, \\ w'(0, t) = 0, \\ (EI)^I w''(l_1, t) - C_a V(t) = (EI)^{II} w''(l_1, t), \\ (EI)^I w'''(l_1, t) = (EI)^{II} w'''(l_1, t), \\ (EI)^{II} w''(L, t) = 0, \\ (EI)^{II} w'''(L, t) = 0. \end{array} \right. \quad (3.12)$$

where

$$\rho^I = (\rho_p W_p h_p + \rho_b W_b h_b) / (W_p h_p + W_b h_b),$$

$$\rho^{II} = \rho_b,$$

$$A^I = W_p h_p + W_b h_b,$$

$$A^{II} = W_b h_b,$$

$$w'(x, t) = \partial w(x, t) / \partial x,$$

$$w''(x, t) = \partial^2 w(x, t) / \partial x^2,$$

$$w'''(x, t) = \partial^3 w(x, t) / \partial x^3,$$

$$w''''(x, t) = \partial^4 w(x, t) / \partial x^4.$$

and ρ is the density of the layers; A is the cross-sectional area of the layers.

Since the applied voltage $V(t)$ is spatially uniform along the length of the cantilever, the spatial derivative of V , which is the input of the system described by the first equation of (3.11), equals to zero. Now the applied voltage $V(t)$ only has effect on the third equation of the boundary conditions of (3.12). Thus, the system is simplified to a linear distributed parameter system that is actuated only at the interior boundary, $x = l_1$. These partial differential equations can not be directly used for traditional controller design. In the following, the Lagrange method is used to obtain a decoupled ordinary differential equation to describe the system in order for controller design.

The kinetic energy of the beam is given by

$$T = \frac{1}{2} \int_0^{l_1} \rho^I A^I \dot{w}^2(x, t) dx + \frac{1}{2} \int_{l_1}^L \rho^{II} A^{II} \dot{w}^2(x, t) dx \quad (3.13)$$

where \dot{w} is the derivative of w with respect to time t . The potential energy of the beam is given by

$$P = \frac{1}{2} \int_0^{l_1} \frac{1}{(EI)^I} [(EI)^I \frac{\partial^2 w(x, t)}{\partial x^2} + C_a V(t)]^2 dx + \frac{1}{2} \int_{l_1}^L (EI)^{II} \left(\frac{\partial^2 w(x, t)}{\partial x^2} \right)^2 dx \quad (3.14)$$

Using the assumed mode-summation method, the solution of (3.11) can be expressed by

$$\begin{cases} w(x, t) = \sum_{i=1}^{\infty} \phi_i^I(x) q_i(t) & \text{for } 0 \leq x \leq l_1 \\ w(x, t) = \sum_{i=1}^{\infty} \phi_i^{II}(x) q_i(t) & \text{for } l_1 \leq x \leq L \end{cases}$$

where $q_i(t)$ is the modal coordinate, and $\phi_i(x)$ is the mode shape which has the following form

$$\phi_i^k(x) = A_i^k \sin \beta_i^k x + B_i^k \cos \beta_i^k x + C_i^k \sinh \beta_i^k x + D_i^k \cosh \beta_i^k x$$

where $k = I, II$

The coefficients A_i, B_i, C_i, D_i are determined to satisfy the boundary conditions given by (3.12).

Substituting (3.15) into (3.13) and (3.14), and then by using the Lagrange equation and augmenting proportional damping (damping coefficient ζ_i), the governing equations can be expressed by decoupled ordinary differential equation for each mode of the cantilever as follows.

$$\ddot{q}_i + 2\zeta_i\omega_i\dot{q}_i + \omega_i^2q_i = -\frac{C_aV(t)}{I_i} \int_0^{l_1} \frac{\partial^2\phi_i^I}{\partial x^2} dx$$

for $i = 1, 2, \dots, \infty$ (3.15)

where ω_i is the eigenfrequency of each mode, and I_i is the generalized mass, defined as follows.

$$I_i = \int_0^{l_1} (\phi_i^I)^2 \rho^I A^I dx + \int_{l_1}^L (\phi_i^{II})^2 \rho^{II} A^{II} dx$$

3.2.2 Control of Adaptable End Effector

In order to keep the adaptable end effector straight during manipulation, a LQR controller is designed in this research to control the adaptable end effector. An advantage of the LQR control method is the linearity of the control law, which leads to easy analysis and practical implementation. Another advantage is its good disturbance rejection and tracking performance and stability. This control algorithm is a state feedback controller and requires a complete knowledge of the whole states for each

time instance. However, only the measurement of the tip displacement is available in this system and no other states are measurable, a full order observer is then required to estimate all of the states.

The goal of the controller is to eliminate the deformation caused by the interaction force between the tip and the manipulated object. In other words, it is desired to have $w(L, t)$, the transverse deflection at the end of the cantilever, equal to zero. By defining $w(L, t)$ as the output $y(t)$, the following equation can be derived from (3.15)

$$y(t) = w(L, t) = \sum_{i=1}^{\infty} \phi_i^{II}(L) \cdot q_i(t) \quad (3.16)$$

A state space model of the system can be obtained using the finite dimensional approximation of the model. Since the higher frequency modes tend to damp out faster and have less effect on the dynamics of the cantilever, only the first N modes are considered in the controller. The state equation for the system is then given as:

$$\begin{cases} \dot{x} = Ax + Bu \\ y = Cx + Du \end{cases} \quad (3.17)$$

where

$$\begin{aligned}
x &= \left[q_1 \ q_2 \ \dots \ q_N \ \dot{q}_1 \ \dot{q}_2 \ \dots \ \dot{q}_N \right]_{1 \times 2N}^T \\
A &= \begin{bmatrix} \mathbf{0}_{N \times N} & & & \mathbf{I}_{N \times N} \\ -\omega_1^2 & & -2\zeta_1\omega_1 & \\ & \dots & & \dots \\ & & -\omega_N^2 & \\ & & & -2\zeta_N\omega_N \end{bmatrix} \\
B &= [\mathbf{0}_{1 \times N} \ -C_a/I_1 \int_0^{l_1} \partial^2 \phi_1^I / \partial x^2 dx \ \dots \\ &\quad -C_a/I_N \int_0^{l_1} \partial^2 \phi_N^I / \partial x^2 dx]^T \\
C &= \left[\phi_1(L) \ \dots \ \phi_N(L) \ \mathbf{0}_{1 \times N} \right] \\
D &= 0, \quad u = V(t)
\end{aligned} \tag{3.18}$$

Since the controller will be implemented on computer, the continuous model has to be discretized with sampling and command updates at intervals T . In addition we assume that a zero-order hold at the controller output will produce a piecewise constant command $u(t) = u(kT)$ for $kT \leq t < (k+1)T, k = 0, 1, \dots, \infty$. The discrete-time state space model is given by

$$\begin{cases} x(k+1) = \Phi x(k) + \Gamma u(k) \\ y(k) = Cx(k) \end{cases} \tag{3.19}$$

In state feedback, the control input takes the form

$$u(k) = -Kx(k) \tag{3.20}$$

Therefore choosing K corresponds to choosing the closed loop system poles to give the desired response. To help choosing appropriate values of K , several optimal control techniques have been developed. The basic idea behind these techniques is that a cost function is defined and then a controller is formed that minimizes this cost function. In this research, the LQR method is used to optimize the value of K . The discrete-time cost function is defined as [107]

$$J(t) = \sum_{k=0}^{\infty} [x(k)^T Q x(k) + u(k)^T R u(k)] \quad (3.21)$$

Here, $Q = Q^T \geq 0$ and $R = R^T > 0$ are weighting matrices which can be used to define the importance of individual states and control inputs.

Since the modal coordinates and their derivatives are chosen as states and they are unmeasurable in this system, a full order state-estimator is constructed as,

$$\hat{x}(k+1|k) = (\Phi - LC)\hat{x}(k|k-1) + Ly(k) + \Gamma u(k) \quad (3.22)$$

where L is the observer gain matrix, and the notation $\hat{x}(k+1|k)$ denotes that the estimate of $x(k+1)$ is made using measurements available at time k . By choosing L appropriately, \hat{x} approaches x exponentially since the estimation error is,

$$\begin{aligned} e(k+1|k) &= x(k+1) - \hat{x}(k+1|k) \\ &= (\Phi - LC)e(k|k-1) \end{aligned} \quad (3.23)$$

The dynamics of the observer are given by the poles of $(\Phi - L * C)$. Since the dynamics of the estimator should be much faster than the system itself, the poles of the observer have to be placed at least three to five times farther to the left than the dominant poles of the system. With the state-estimator, we can obtain an output-feedback controller using the estimated state \hat{x} instead of the true state x .

$$u(k) = -K\hat{x}(k) \quad (3.24)$$

Using this feedback, the closed loop system now becomes

$$\begin{bmatrix} x(k+1) \\ \hat{x}(k+1) \end{bmatrix} = \begin{bmatrix} \Phi & -\Gamma K \\ LC & \Phi - LC - \Gamma K \end{bmatrix} \begin{bmatrix} x(k) \\ \hat{x}(k) \end{bmatrix} + \begin{bmatrix} BG \\ BG \end{bmatrix} r \quad (3.25)$$

The structure of the controller is shown in Fig. 3.8. The term G is a constant gain, and is included to achieve asymptotic tracking of a step input.

The existence and stability of the steady-state LQR solution has been proven in [108] and [109]. For a LQR problem with $R > 0$, and $Q = C^T C$, where the pair (Φ, C) is detectable and the pair (Φ, Γ) is stabilizable, it follows that a solution to the steady-state LQR problem exists. In particular, there exists a unique positive semidefinite solution W to the discrete algebraic Riccati equation

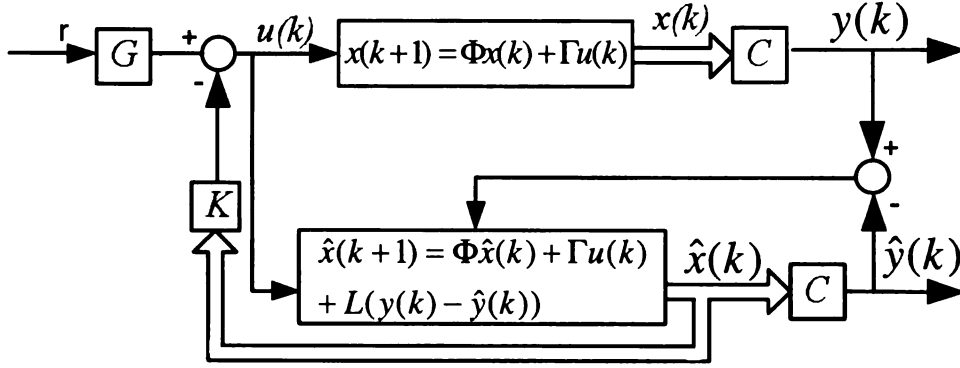


Figure 3.8. Controller block diagram.

$$W = Q + \Phi^T W \Phi - \Phi^T W \Gamma [R + \Gamma^T W \Gamma]^{-1} \Gamma^T W \Phi \quad (3.26)$$

and if

$$K = (R + \Gamma^T W \Gamma)^{-1} \Gamma^T W \Phi \quad (3.27)$$

then the closed loop system (3.25) is asymptotically stable.

3.2.3 Experimental Implementation

The experiments on the AFM based nanomanipulation system were performed at stable room temperature. As introduced in Fig. 3.4, the nanomanipulation system mainly consists of a NanoScope IV Atomic Force Microscope (Digital Instruments Inc., Santa Barbara, CA) and some peripheral devices including an optical microscope, a haptic device (Phantom), a Multifunction Data Acquisition (DAQ) card NI PCI-6036E (National Instruments), and three computers.

System Identification

In the experiments, an active probe DMAPS (Veeco Instruments), which has been introduced in Section III, was used as the adaptable end effector. The tip displacement is obtained from AFM's photodiode sensor.

The parameters of the adaptable end effector are given in Table 3.1. These parameters are obtained from the manufacturer's specification sheets or from the materials handbook.

Table 3.1. Cantilever parameters

Parameters	Values	Parameters	Values
l_1	$374\mu m$	L	$500\mu m$
h_p	$3.5\mu m$	h_b	$4\mu m$
w_p	$250\mu m$	w_b	$250\mu m$
w_2	$51\mu m$	h_2	$4\mu m$
E_p	$1.2 \times 10^{11} N/m^2$	E_b	$1.69 \times 10^{11} N/m^2$
ρ_p	$5.2 \times 10^3 Kg/m^3$	ρ_b	$2.33 \times 10^3 Kg/m^3$
d_{31}	$3.7 \times 10^{-12} m/V$	k	$1 - 5 N/m$

The damping coefficients for each mode are identified experimentally. They are adjusted to get a best match in the frequency response of the theoretical model and the experimental data. The damping coefficients for the first two modes are listed in Table 3.2.

To experimentally verify the accuracy of the cantilever model, an excitation step voltage of $-5V$ is applied to the piezo actuator, and then the vibration of the cantilever tip is measured and analyzed. Fig. 3.9 shows the measured tip displacement in the experiment. It is shown that the tip is driven to $-100nm$ and then keeps oscillating around that point until settling down. To identify the frequency components

Table 3.2. Damping constants

Mode	Theoretical frequency (KHZ)	Damping coefficients
1	49.2	0.005
2	216.3	0.007

of the vibration, the fast-Fourier transform (FFT) is taken to compute the power spectral density, a measurement of the energy at various frequencies. The frequencies of the vibration can be easily identified from the power spectral density plot as shown in Fig. 3.9. It can also be observed from Fig. 3.9 that the first mode dominates the response of the cantilever over other higher modes.

The natural frequencies of the cantilever can also be obtained numerically using the modal analysis method. The experimentally obtained modal frequencies are compared with the theoretically determined modal frequencies in Table 3.3. It can be seen that the theoretical values are in good agreement with the experimental values. This confirms that the theoretical model is accurate enough to predict the modal frequencies and can be used for controller design.

Table 3.3. Modal frequencies (kHz)

Mode	Theoretical frequency	Experimental frequency
1	49.2	49.8
2	216.3	216.0
3	374.4	372.5

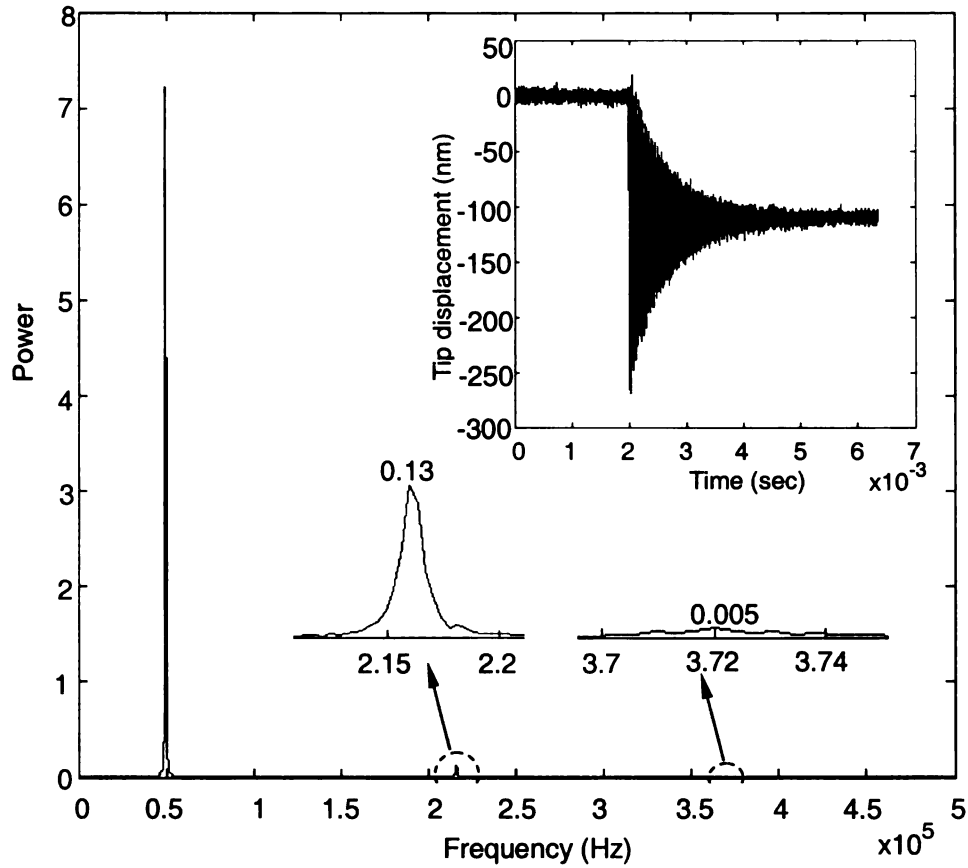


Figure 3.9. Measured tip vibration of the cantilever without closed-loop control.

Implementation of the controller

The LQR control law has been implemented with the parameters in Table 3.1. From Fig. 3.9, it can be seen that only the first modes dominates the response of cantilever during free vibration. Therefore only the first mode is considered in controller design. Thus the modes number N equals to 1. The weighting matrices were chosen by the Bryson's rule [110] and a trial-and error iterative design procedure. The resulting weighting matrices are:

$$\begin{aligned} Q &= \text{diag}(100 \ 1.5), \\ R &= 0.001 \end{aligned} \tag{3.28}$$

Then the gain K can be calculated:

$$K = [1.1830 \times 10^6 \ 5] \tag{3.29}$$

The real-time implementation of this controller is performed using an x86 based PC running Linux operating system. The RTAI [111] (Real-time Applications Interface) patch is used to provide POSIX compliant, real-time functionality to the Linux OS.

To illustrate the effectiveness of the controller, closed-loop trajectory tracking experiments were carried out. The best effort has been made to tune the parameters of the LQR controller to get a best tracking performance. Fig. 3.10 shows the tracking responses of a sine wave and a triangular wave respectively. The results shows that the tip can be controlled to follow the desired trajectory very well. The amplitude of the error for sine wave tracking is 10 *nm*. The closed-loop trajectory tracking experiments were also performed with a simple PD controller. The best effort has also been made to tune the parameters of the PD controller to get a best tracking performance. Fig. 3.11 shows the tracking responses with the PD controller. The amplitude of the error for sine wave tracking is 20 *nm*. By comparing these two experimental results. It can be seen that the tracking errors of the LQR controller are smaller than those of the PD controller.

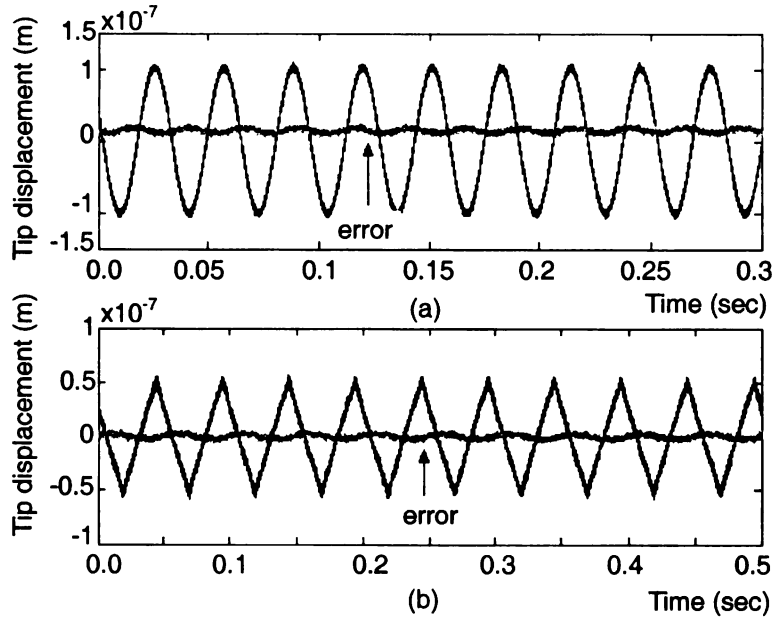


Figure 3.10. Tracking response of (a) a sine wave and (b) a triangular wave. The controller is LQR controller.

Experiments of tracking a square wave are also performed. Fig. 3.12. (a) and (b) show the tracking responses of a square wave with the PD controller and the LQR controller respectively. It can be observed that the settle down time of the LQR controller (0.4 millisecond) is smaller than the settle down time of the PD controller (0.7 millisecond). As shown in Fig. 3.12. (c), by zooming into 0.016 sec in Fig. 3.12. (b), the settle down time of the closed-loop system with LQR controller is only 0.4 millisecond. It is much smaller than the settle down time of the open-loop system, which can be estimated as 3 millisecond from the insert of Fig. 3.9. Hence, the LQR controller does improve the dynamic performances of the cantilever.

It has to be mentioned that the noise of the measurement is quite large due to the characteristics of the photodiode. From the insert of Fig. 3.9, it can be calculated that the amplitude of the noise is more than seven percent of the signal. Undoubtedly, the noise will affect the control effect. Another factor reducing the performance of the

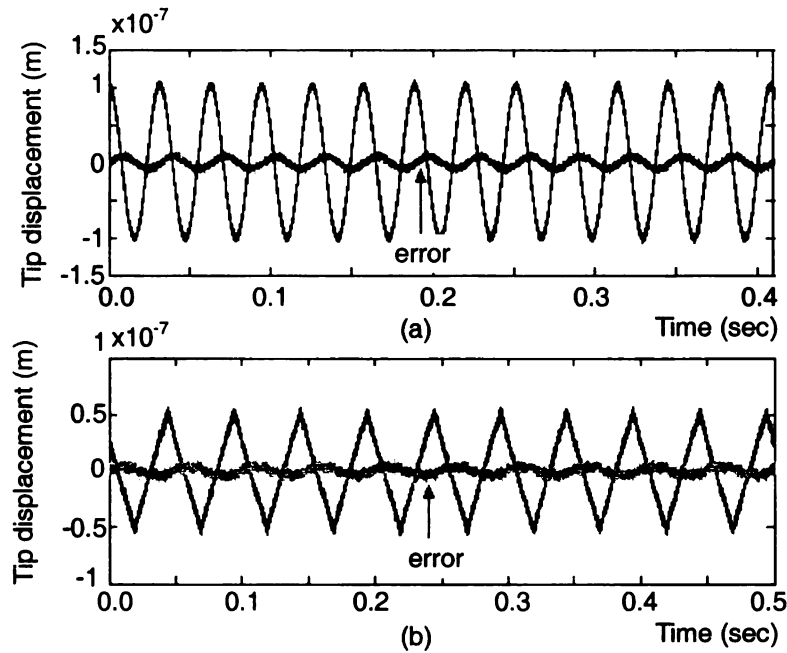


Figure 3.11. Tracking response of (a) a sine wave and (b) a triangular wave. The controller is a PD controller.

controllers is the relatively low sampling rate of the real-time linux system, which can only reach 70 KHz. However, the frequency of the first mode is around 50 KHz. Since only less than two control inputs can be applied on the cantilever during one vibration period, it is really difficult to get good control effect. That is the reason that the LQR controller, designed after a PD controller, does not improve the performance much. The large overshoot of the step response is also due to the low sampling rate. However, it can be reduced significantly by including input shaping [112] in the controller. The step response of the LQR controller with zero vibration input shaping is shown in Fig. 3.13.

3.2.4 Experimental Results on Manipulating Nano-Objects

In this section, nanomanipulation experiments using the adaptable end effector were performed to verify the effectiveness of the controller and the efficiency of the

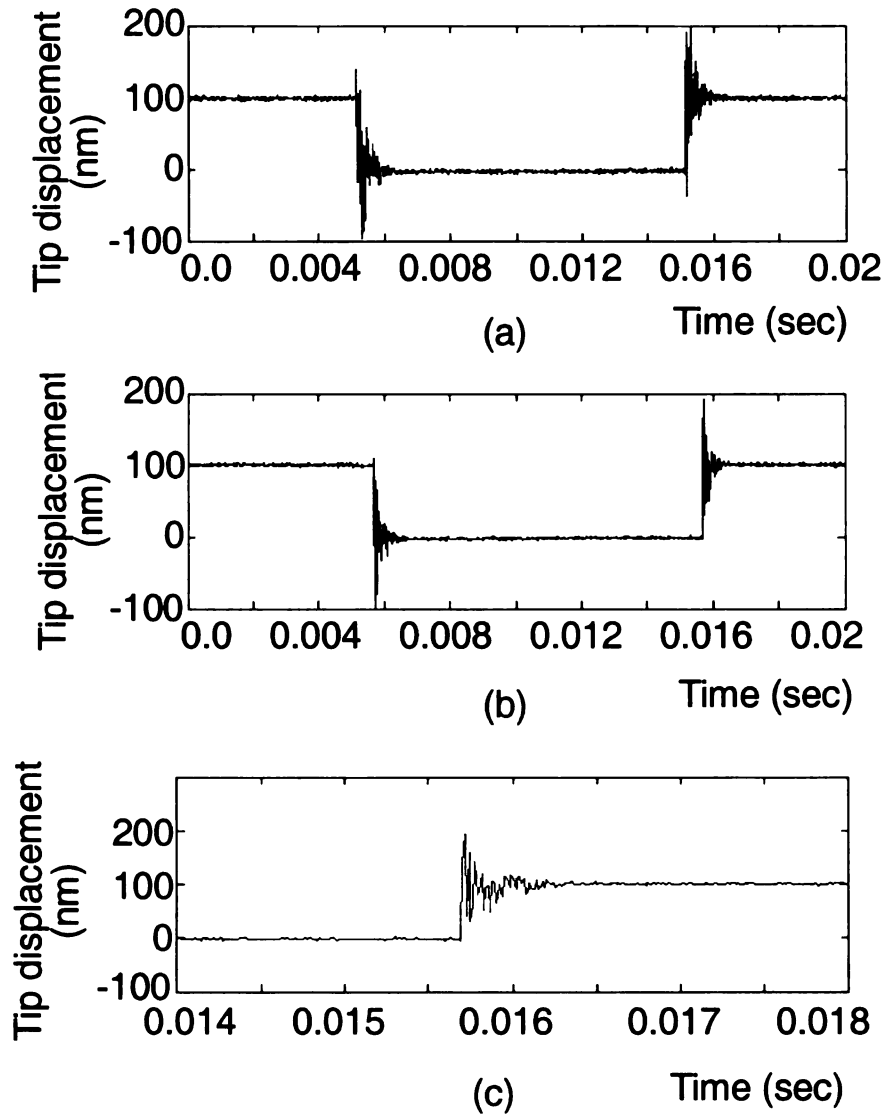


Figure 3.12. (a) Tracking response of a square wave with PD controller. (b) Tracking response of a square wave with PD controller. (c) Zoom in around 0.016 sec in (b).

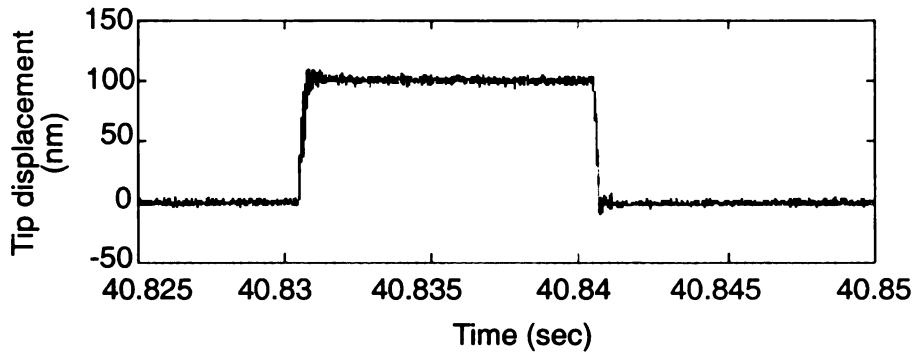


Figure 3.13. Tracking response of a square wave with the LQR controller and input shaping

system.

Fig. 3.14. (a) shows an AFM image of a silver nanowire with length of $1.9\mu\text{m}$ and diameter of 120nm . An adaptable end effector (spring constant $k = 1\text{-}5\text{ N/m}$) was used to push this silver rod. Fig. 3.14. (b) shows the AFM image by a new scan after pushing. It can be seen that the silver nanowire was pushed to the desired position successfully. Fig. 3.14. (c) shows the control signal and the response of tip. The AFM tip was driven to float on the top of the sample surface at $t = 19\text{sec}$. After that, the controller started at $t = 21\text{sec}$. The AFM tip also began to move toward the nanowire and then hit the nanowire at $t = 30\text{sec}$. Then, at $t = 37\text{sec}$, the silver nanowire was pushed to the desired position. Finally, the tip was lifted up and the controller was turned off. From Fig. 3.14. (d), it can be seen that the deflection signal is almost flat which means that the cantilever was controlled to keep straight during manipulation. The two small peaks are due to turning on and off the controller. It can also be observed from Fig. 3.14. (c) that there is substantial increase of control signal after the tip touched the rod. Thus, the interaction force can be easily reconstructed from the control signal. The force feeling from the haptic device is much better than that using the traditional cantilever.

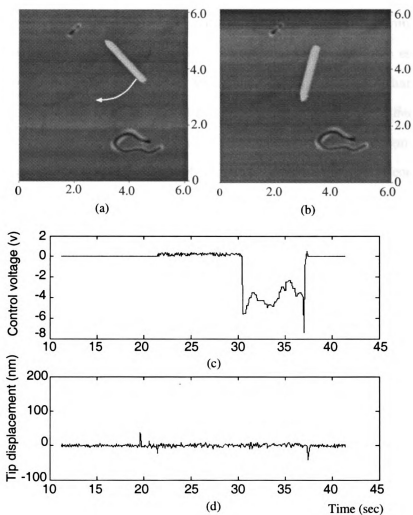


Figure 3.14. Pushing a silver nanowire with an adaptable end effector. (a) The AFM image of a silver nanowire with length of $1.9\mu\text{m}$ and diameter of 120nm . The scanning range is $6\mu\text{m} \times 6\mu\text{m}$. (b) The AFM image by a new scan after pushing. (c) The control voltage applied on the adaptable end effector. (d) Tip displacement signal measured by the photodiode sensor.

To quantitatively show that using adaptable end effector does improve the efficiency of the nanomanipulations, a set of experiments were carried out and analyzed. Manipulations using a soft probe (Model: OTR8-35, Veeco Instruments, $k = 0.57$ N/m) with/without preload, a rigid probe (Model: TESP, Veeco Instruments, $k = 20-80$ N/m) with/without preload and an actively controlled adaptable end effector (DMASP, Veeco Instruments, $k = 1-5$ N/m) are conducted for more than 10 times respectively. Fig. 3.15 shows successful rates of manipulations using different probe by counting the successful manipulations. It can be observed that the rigid probe has higher successful rate than the soft probe when no preload applied. It consists with the analysis in introduction. By applying a preload, both manipulations using the soft probe and the rigid probe get higher successful rates. It is also shown that both the manipulations using the adaptable end effector and the rigid probe (with preload) reach the high successful rate of 90% . Therefore, the efficiency of nanomanipulation is improved using an adaptable end effector.

To prove the high sensitivity of the adaptable end effector, another set of experiments were performed and the force feedback signals are analyzed. Since the successful rate of the manipulations using the soft probe without preload is too low, it is meaningless to analyze the sensitivity of the soft probe without preload. Therefore, soft tip without preload will not be discussed in the following discussion.

First, a probe is used to push a nanowire with length of l_1 . The change of the signal (it can be the deflection of the traditional cantilever or the control signal of the adaptable end effector) caused by the interaction force is denoted as ΔS_1 . Then, the same probe is used to push another longer nanowire with length of l_2 . The change of the signal is denoted as ΔS_2 . Based on the assumption that nanowires with different length will cause different manipulation force, the ratio of ΔS_2 over ΔS_1 should

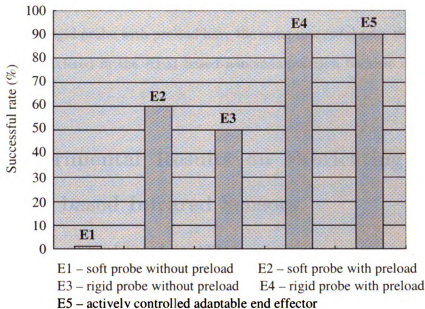


Figure 3.15. Successful rates of manipulations using different probe

represent the sensitivity of the probe. Hence, a metric S can be used to evaluate the sensitivity.

$$S = \frac{\Delta S_2}{\Delta S_1} \quad (3.30)$$

Two nanowires with length of $l_1 = 2\mu\text{m}$ and $l_2 = 4\mu\text{m}$ are pushed by different probes for multiple times. Then for each manipulation, the value of S is calculated. Except the adaptable end effector, the manipulations using other probes (soft probe with preload, rigid probe with/without preload) have the values of S around 1, which means the cantilever is not sensitive to changes of the interaction force. At the same time, ΔS_1 and ΔS_2 of these manipulations are also very small. This makes it difficult to measure changes of the signal. For the manipulations using adaptable end effector, much larger ΔS_1 and ΔS_2 are obtained from the control signal, and the value of S

is in the range of 1.2 – 1.8. Therefore, even manipulations using the adaptable end effector and the rigid probe with preload have the same successful rate, the adaptable end effector is preferred in the AFM based nanomanipulation because of its higher force sensitivity.

3.3 Experimental Results on Fabricating Single CNT based Infrared Sensors

The effectiveness and reliability of the AFM based nanomanipulation method using adaptable end effector have also been proved by practical applications. This system has been employed to manipulate the carbon nanotubes (CNT) onto some nano-electrical devices to build nano-sensors. Fig. 3.16 shows the process of manipulating a CNT onto a pair of gold electrodes to form a connection. Fig. 3.16. (a) shows the AFM image before manipulation. There are two CNTs in the image, a longer one and a shorter one. The longer one will be pushed onto the electrodes to form the connection, and the shorter one will be pushed away. Fig. 3.16. (b) shows the image from a new AFM scan after manipulation. Fig. 3.17 shows the process of manipulating another CNT onto electrodes. With this system, the nanomanipulation and nanoassembly is not difficult anymore. It becomes more deterministic and more reliable. Fig. 3.18 shows another four assemble results of CNT based nano-sensors.

3.4 Chapter Summary

The fabrication and assembly process for building single CNT based nanodevices is presented in this chapter. Firstly the fabrication process is addressed, where the DEP deposition method is used to attract individual CNTs to the microelectrodes, then the AFM manipulation method is employed to manipulate a single CNT to

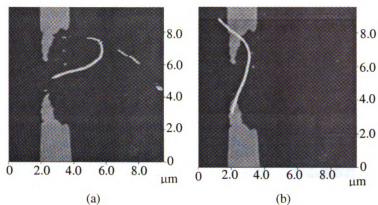


Figure 3.16. Manipulating a CNT onto a pair of gold electrodes. (a) The AFM image before manipulation. (b) The image from a new AFM scan after manipulations.

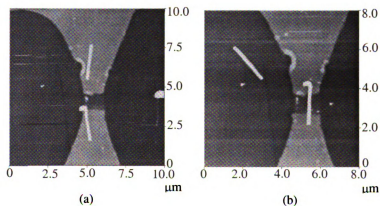


Figure 3.17. Manipulating a CNT onto a pair of gold electrodes. (a) The AFM image before manipulation. (b) The image from a new AFM scan after manipulations.

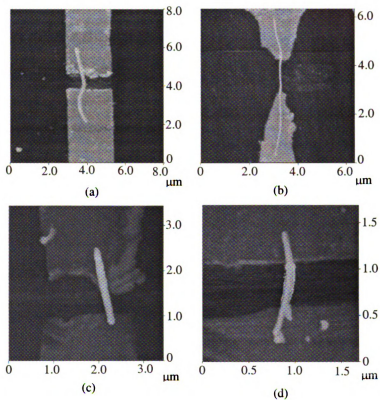


Figure 3.18. Four different results of pushing CNT onto gold electrodes.

bridge the microelectrodes and clean the rest CNTs and particles away. Then the key technology for assembling single CNT devices, the AFM based nanomanipulation system enhanced by an adaptable end effector, is introduced and experiments for verifying the manipulation system are discussed. Finally, experiments of fabricating single CNT based infrared sensors are presented to show the efficiency of the developed fabrication process.

CHAPTER 4

Testing of Single CNT based IR Sensors

As a promising one dimensional nanomaterial, CNT has been extensively studied for electronic and photonic applications. However, the reported results have shown a big variance on the electronic properties of CNTs. It is necessary to have a reliable testing procedure as well as testing environment for characterizing the CNT based IR sensors. In this chapter, the development of a cryogenic IR sensor testing system will first be presented. Then the experimental testing and characterization of CNT IR sensors will be discussed.

4.1 Development of the Testing System

An IR sensor testing system is developed to test the sensor in different environments. As shown in Fig. 4.1, the SWNT based IR sensor testing system includes four major components: sensor chamber, lens, IR source and the signal measurement module. The sensor chamber is electrically and thermally shielded to decrease the background noise. The IR light from the IR source is focused onto the CNT sensor by the IR lens. By using a NIR laser as IR source, the system can be used for NIR testing. The system

can also be used for MIR testing with a blackbody IR source. The photocurrent signal is measured by the signal measurement module through the electrical feedthroughs.

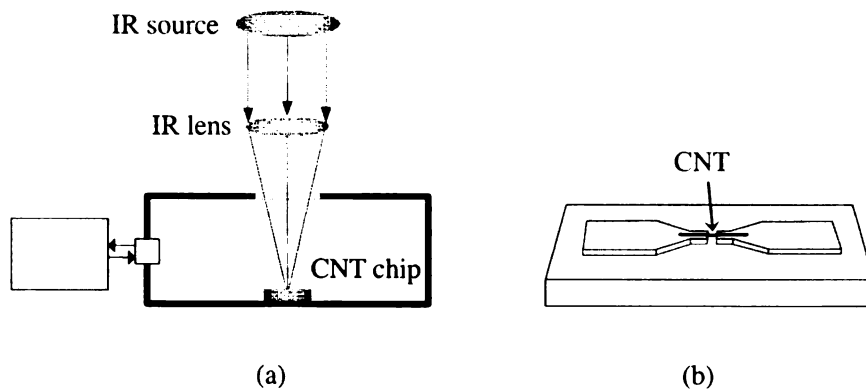


Figure 4.1. (a) The SWNT IR detection system. (b) The structure of the CNT chip.

To test the MIR response of the CNT IR sensors, a cryogenic MIR testing system has been developed as shown in Fig. 4.2. The MIR source is an Oriel 67030 blackbody (Newport Corp.) with a temperature range of $50^{\circ}C$ to $1050^{\circ}C$. Filters with different spectrum are used to get IR light with different wavelenghtes. The lens focuses IR onto the CNT sensor, which is mounted inside a cryogenic cooling chamber. The sensor temperature can vary from room temperature to $-196^{\circ}C$. With the cryogenic cooling system, the CNT sensor can be characterized at different temperature as well as different gas environment.

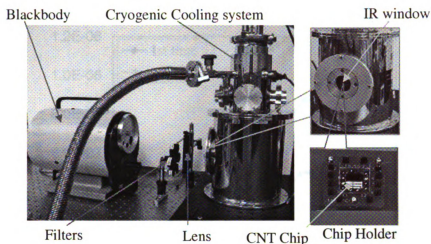


Figure 4.2. The cryogenic MIR testing system.

4.2 Individual Multi-Walled Carbon Nanotube based IR Sensors

4.2.1 Bandgap Engineering of MWNTs

Since it is difficult to guarantee the properties of each individual CNT from the synthetic point of view. Therefore, the simplest way is to modify them using the electrical shell breakdown process [113] after CNT based devices are fabricated by using AFM nanomanipulation system. By applying a bias voltage on the MWNT and controlling the current, the outer layers of the MWNT can be broken at certain current. Fig. 4.3 shows the first two measurements of the I-V curve of a MWNT device. It is found that the currents suddenly dropped at a certain threshold voltage and increased again. This was caused by the burning of the MWNT walls which contributed to the conduction. Fig. 4.4 shows the I-V curve of the device after three breakdowns. It can be seen that the metallic MWNT became semiconductive one after two breakdowns.

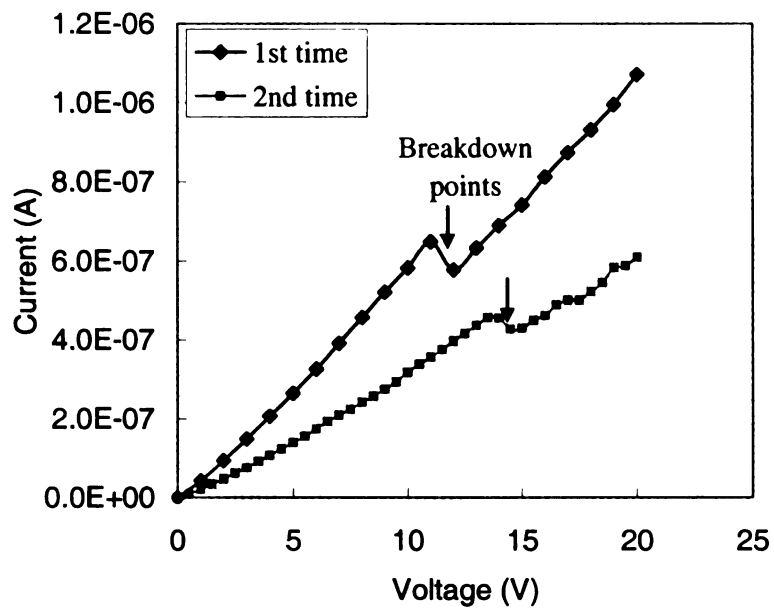


Figure 4.3. I-V curves of a single MWNT device.

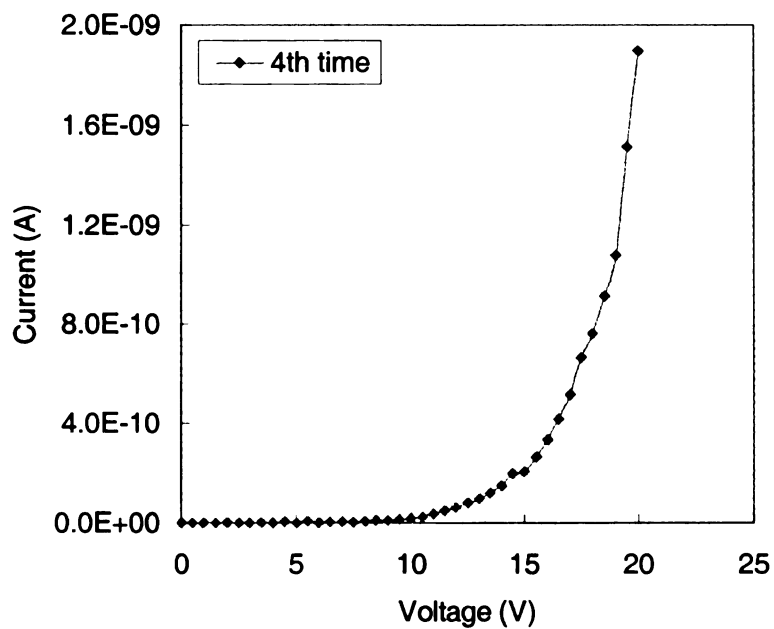


Figure 4.4. I-V curve of the single MWNT device after three breakdowns.

4.2.2 Experimental Testing of MWNT Sensors

The AFM image of the MWNT IR sensor is shown in Fig. 4.5. The diameter of the MWNT on the chip is around 65 nm. Due to the large diameter, the MWNT have a very small bandgap. Hence the MWNT-metal contacts are quasi-Ohmic contacts with small barriers. The I-V curve of this device is shown in Fig. 4.6. Temporal photocurrent response was tested with a NIR laser source, which has a wavelength of 830 nm and power of 30 mW. Fig. 4.7 shows the temporal IR response with a bias voltage of $-0.1 V$ while the IR source was switched on/off periodically. The current decreased as the IR source was switched on. Fig. 4.8 shows the temporal IR response with a bias voltage of $0.1 V$. The current increased as the IR source was switched on. Fig. 4.9 shows the plot of the photocurrent (the current change ΔI when IR is on) as a function of the bias voltage. It can be seen that the MWNT works as a photosensitive resistor. This is caused by the photoinduced carrier concentration change in the CNT. When the IR irradiates the CNT, photons will excite electrons and holes inside the CNT and raise the carrier concentration. It can also be seen that the photoinduced current change ($1.4 \mu A$ at $V_{bias} = 0.1 V$) is quite big compared with the reported photocurrent of SWNTs ($0.25 nA$ at $V_{bias} = -3 V$ [13]). Since a MWNT has bigger diameter and multiple walls, it can absorb photons more effectively than SWNTs. Hence MWNT sensors are expected to have a higher quantum efficiency than SWNT sensors. The quantum efficiency of this device is calculated as $\sim 30\%$, which is much higher than the reported values ($< 10\%$) of SWNT devices.

Individual MWNT based IR sensors were fabricated and tested in research. The electrical shell breakdown technique was used to modify the electrical properties of the MWNT after CNT devices were fabricated. Experiments were carried out to exam the electrical properties and photoresponse of the single MWNT based IR sensors. The results show that the MWNT based IR sensor has higher photocurrent and quantum efficiency than the SWNT sensors. However, the detectivity of the MWNT IR sensor

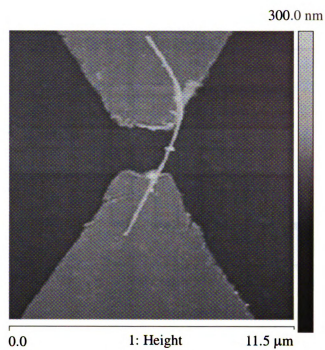


Figure 4.5. AFM image of the MWNT IR sensor.

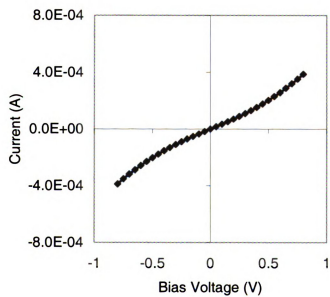


Figure 4.6. I-V curve of the MWNT IR sensor.

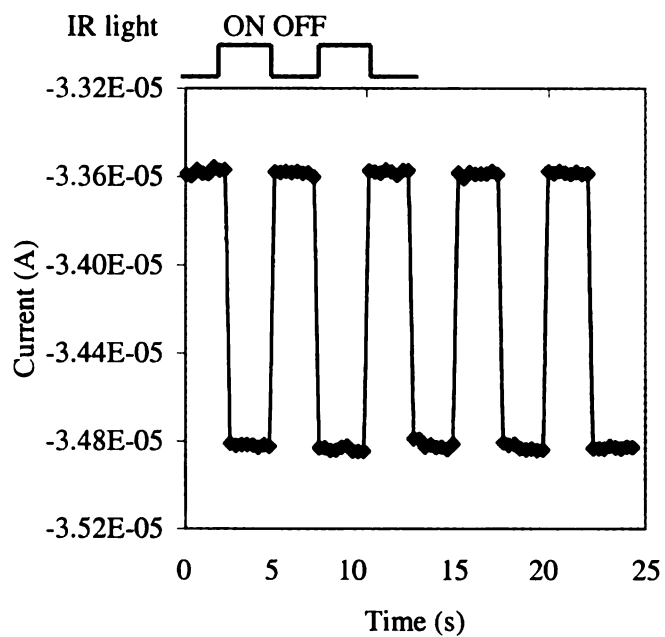


Figure 4.7. Temporal photoresponse of the MWNT IR sensor. The bias voltage across the electrodes is -0.1 V .

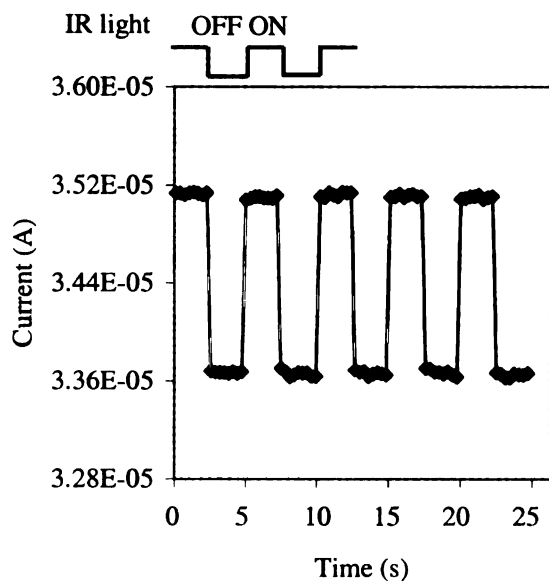


Figure 4.8. Temporal photoresponse of the MWNT IR sensor. The bias voltage across the electrodes is 0.1 V .

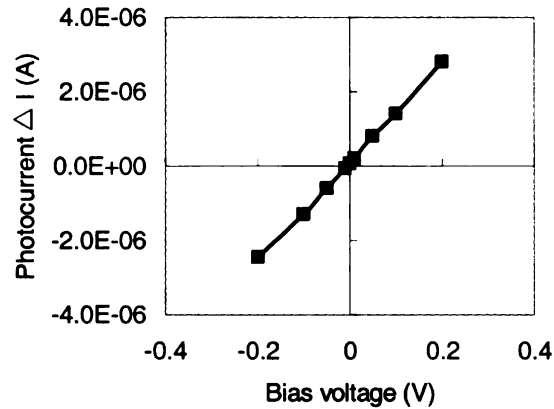


Figure 4.9. The plot of photocurrent vs. bias voltage.

is still smaller than traditional IR sensors due to the high noise and short absorption depth caused by its small diameter.

4.3 Individual Single-Walled Carbon Nanotube based IR Sensors with Symmetric Structure

The SWNTs used in our experiments were obtained from BuckyUSA, Inc. It takes several steps to deposit an individual CNT onto the substrate. Firstly, the powdery CNTs are put into acetone and ultrasonicated for 10-15 min to form CNT suspension. Then a droplet of the CNT suspension is dropped onto the substrate between the two microelectrodes. At the same time, a sine wave AC signal with frequency of 10 kHz and peak to peak amplitude of 1.5 V is applied between the two microelectrodes for 3-5 seconds to generate the dielectrophoretic force to trap CNTs to the microelectrodes. During the deposition process, the concentration of the CNT suspension, the frequency and the amplitude of the AC signal are experimentally optimized to achieve optimal possibility to trap an individual CNT between two microelectrodes. Even with those parameters experimentally optimized, it can not be guaranteed that only one CNT is trapped between the two microelectrodes and bridges them success-

fully. Normally, there are some impurities or more than one CNT trapped between the microelectrodes. Furthermore, if only one CNT is successfully trapped between the microelectrodes, it might not bridge the microelectrodes very well. Therefore, it is necessary to take another step to clean up the microelectrodes gap area and adjust the position of the CNT to make the connection. This final step is very critical and is termed CNT assembly. The AFM based nanomanipulation system [78] is employed to perform the CNT assembly.

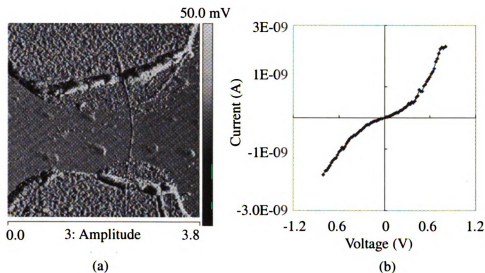


Figure 4.10. (a) AFM image of an individual SWNT based photodiode with symmetric Au electrodes. (b) I-V curve of the CNT photodiode.

We first fabricated individual SWNT based Schottky photodiodes with symmetric gold (Au) contacts. The AFM image of a SWNT device is shown in Fig. 4.10(a). The diameter of the SWNT on the chip is 1.7 nm . As shown in Fig. 4.10(b), its I-V characteristic curve is symmetric due to the symmetry of the CNT-metal contacts. Although Au has a high work function of 5.2 eV , due to the work function reduction at Au surface caused by the contaminants [114] and the low interaction energy between CNTs and Au [115], the CNT-Au contact is a Schottky contact with a small barrier rather than an Ohmic contact. Since the carriers can easily tunnel through the small

barriers, the current increases quickly even at a very low reverse bias voltage. Hence the I-V curve in Fig. 4.10(b) did not show a very low reverse current.

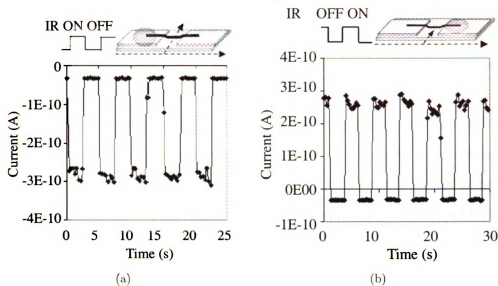


Figure 4.11. Temporal photocurrent response of the SWNT photodiode with a zero bias voltage. (a) IR irradiates the left electrode. (b) IR irradiates the right electrode.

We tested the photovoltaic effect of the CNT based Schottky photodiode with a zero bias voltage applied across the CNT. The current signal was measured with a Keithley 6487 Picoammeter. The IR source was a near-IR laser (UH5-30G-830-PV, World Star Tech.) with a wavelength of 830nm and a power of 30mW. A zero bias voltage was applied on the CNT photodiode and the current was monitored while the IR source was periodically switched on and off. Fig. 4.11(a) shows the temporal IR response when the IR spot center was on the left electrode. The current decreased when the IR source was on. Fig. 4.11(b) shows the temporal IR response when the IR spot center was on the right electrode. The current increased when the IR source was on. The negative dark current was caused by the output error of the voltage source.

As shown in the top image of Fig. 4.12, the IR spot was moved from left to right

following the microelectrodes. The plot of the photocurrent (the current increment when the IR is on) as a function of the IR spot center position is shown in Fig. 4.12. It can be seen that the photocurrent changed from negative to positive continuously as the IR spot moved from left to right. Since the device was zero biased, the photocurrent must be generated by the photovoltaic effect. If the photocurrent was caused by the conductance change due to heating effect or photoconduction effect, it would not be able to change from positive to negative when the IR spot moved from left to right. The reason photocurrent changed from positive to negative was because the CNT formed Schottky diodes at both electrodes and they were connected reversely. When the IR spot center was on the left electrode, the diode at this electrode dominated and the photocurrent was negative. When the IR spot center moved to another electrode, the diode at that electrode dominated and the photocurrent became positive. Since the IR energy was normally distributed, the photocurrent was maximized at the point where the difference between the light intensity at these two CNT-Au interfaces was maximum rather than at the point where the spot center was at one of the CNT-Au interface. Hence the distance between the two photocurrent peaks was $30 \mu m$, though the distance between the two microelectrodes was only $2 \mu m$. Since it is impossible to only focus light onto one microelectrode during real applications, the intensity of the incident light at these two CNT-electrode interfaces will be very close. Hence the photocurrents generated at the two interfaces will cancel each other and the measurable signal will be very weak, which limits the efficiency and sensitivity of the symmetric CNT based photodiode. Furthermore, since there are two Schottky diodes, the electrons and holes generated at each diode had to tunnel through another Schottky barrier to form a current. This also limited the efficiency and sensitivity.

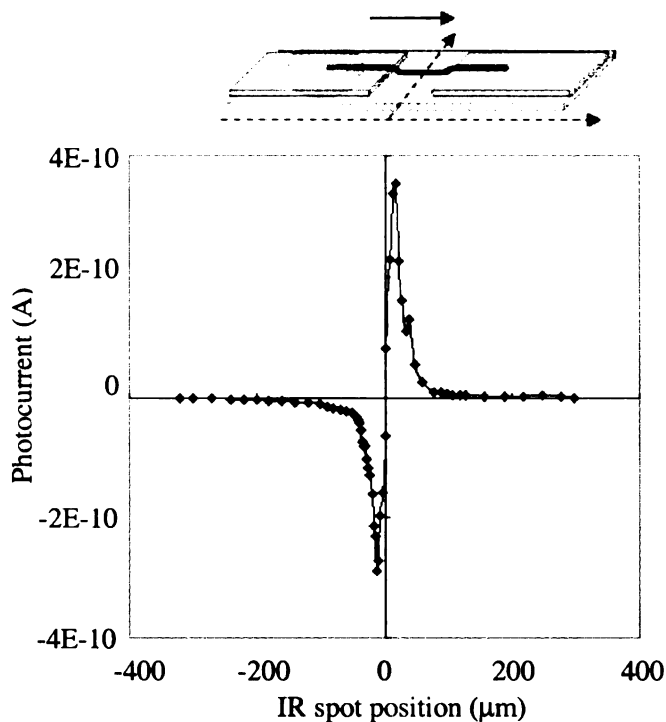


Figure 4.12. The plot of the photocurrent as a function of the IR spot position.

4.4 Individual Single-Walled Carbon Nanotube based IR Sensors with Asymmetric Structure

To improve the performance of the SWNT photodiode, we designed an asymmetric structure which used different materials as the contact electrodes to create Schottky barrier at one electrode and ohmic contact at another electrode. Consequently the photocurrent generated at the Schottky barrier will not be canceled, and it does not need to tunnel through another Schottky barrier. For example, palladium (Pd) has a work function as high as 5.1 eV and was reported to be the best metal to form an Ohmic contact with CNT [41,99,104], whereas titanium (Ti) has a lower work function of 4.3 eV and forms Schottky barrier with CNT [41]. When Ti and Pd are used as the contact materials, a Schottky contact is formed at the CNT-Ti interface and an Ohmic

contact is formed at the CNT-Ti interface. In this way, the photocurrent generated at the CNT-Pd interface is zero and the total photocurrent is maximized to equal the photocurrent generated at the CNT-Ti contact. Hence, with the asymmetric contacts, the efficiency and sensitivity of individual SWNT based photodiodes can further be improved. To compare with the experimental results of the symmetric Au-Au structure, we used Ti and Au to make an asymmetric photodiode. Since the work function of Au is quite high, the Schottky barrier at the CNT-Au interface is very small and the photocurrent generated at the CNT-Au interface will not neutralize as much the photocurrent generated at the CNT-Ti interface.

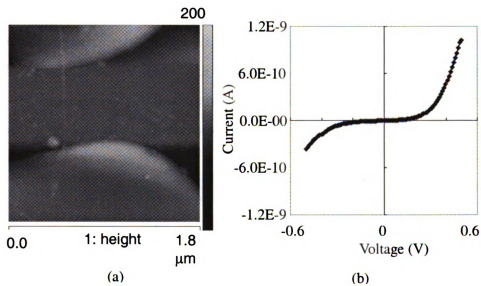


Figure 4.13. (a) AFM image of an individual CNT photodiode with asymmetric Ti-Au electrodes. (b) I-V curve of the asymmetric CNT photodiode.

Fig. 4.13(a) shows a CNT photodiode with asymmetric Ti-Au electrodes. As shown in Fig. 4.13(b), its I-V curve illustrates a Schottky diode behavior. Since the Schottky barrier became higher as well as thinner with a reverse bias voltage and a low reverse bias could make it thin enough for carriers to tunnel through, the saturation current increased dramatically at a low reverse bias voltage. Fig. 4.14(a) shows the

plot of its photocurrent as a function of the IR spot position. It can be observed that the photocurrent was only $-2 \times 10^{-12} \text{ A}$ when the IR spot was on CNT-Au interface, and the photocurrent was $1.3 \times 10^{-10} \text{ A}$ when the IR spot was on CNT-Ti interface. There are two reasons for the asymmetry of the photocurrent. Firstly, since the built-in potential at the CNT-Ti interface is stronger than the one at the CNT-Au interface, there will be more electron-hole pairs generated at the CNT-Ti interface. Secondly, since the barrier height at the CNT-Ti interface is higher than the one at the CNT-Au interface, the electrons and holes generated at the CNT-Au interface are more difficult to tunnel through the barrier at the CNT-Ti interface to form photocurrent. But the electrons and holes generated at the CNT-Ti interface can tunnel through the CNT-Au barrier relatively easier. Hence, a higher photocurrent will be generated at the CNT-Ti interface when both microelectrodes are evenly illuminated. In this way, the measurable signal was much stronger than the symmetric CNT photodiode. Hence the efficiency and sensitivity were also improved.

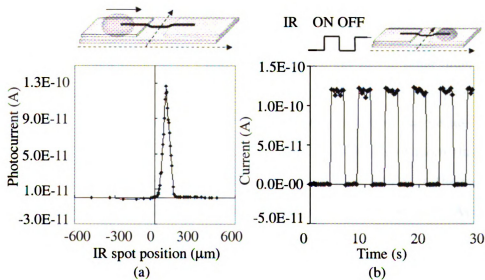


Figure 4.14. (a) The photocurrent as a function of the IR spot position. (b) Temporal photocurrent response of the photodiode with asymmetric electrodes. The device was zero biased. The IR power was 30 mW.

Fig. 4.14(b) shows the temporal photocurrent response of the asymmetric CNT photodiode with a zero bias voltage when the IR spot was on Ti electrode. The current increased from $1.2 \times 10^{-13} A$ to $1.3 \times 10^{-10} A$ when the IR was switched on. For the symmetric photodiode as shown in Fig. 4.11(b), the current increased from $-3.4 \times 10^{-11} A$ to $2.8 \times 10^{-10} A$ when the IR was switched on. We can see that the symmetric CNT photodiode has a higher photocurrent than the asymmetric one. This is due to the variety in the properties of the CNTs for these two devices. Normally, different CNTs from the same production batch may have a variation of 1 to 2 orders in photocurrent. Although this symmetric device has a higher photocurrent, it also has a higher dark current due to low barrier height at CNT-Au interface. Its signal to dark current ratio (SDR) is only 9.2, which makes it difficult to detect low intensity IR light. We also tried to fabricate symmetric CNT photodiode with Ti electrodes. Larger barrier height at CNT-Ti interface leads to a much smaller dark current. Since there are two CNT-Ti Schottky barriers, the large barrier height also makes it difficult for electrons and holes generated at one barrier to tunnel through another barrier, which causes a very small or even zero photocurrent. Since an asymmetric CNT photodiode has a low dark current and a big photocurrent at the same time, it has much higher SDR than a symmetric CNT photodiode. The asymmetric photodiode presented here has a SDR of 1.08×10^3 , which is two orders of magnitude higher than the SDR of the symmetric device. Based on our testings of more than fifty similar devices, normally symmetric CNT photodiodes have a SDR in the range of 0.1 - 10, whereas the asymmetric CNT photodiodes have a SDR over 1000. As shown in Fig. 4.15, we also measured the I-V characteristic curves of the asymmetric CNT photodiode. The I-V curve shifted downwards as the IR power increased, which is a typical behavior of the traditional photodiode.

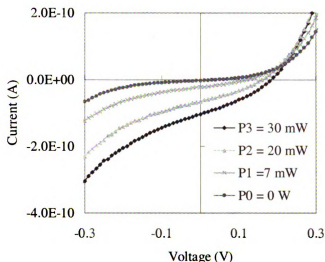


Figure 4.15. I-V characteristic curves of the asymmetric CNT photodiode. P_0 - P_3 represent different IR powers.

4.5 Sensing Middle IR Using CNT Based IR Sensors

A MIR sensing material has to have a bandgap smaller than the energy of MIR photons. But the small bandgap causes a large thermal noise and the traditional MIR sensing system has to work at ultra-low temperature to decrease the thermal noise. Hence a cryogenic cooling system is normally required. However, cryogenic cooling system severely limited the applications of MIR sensing systems and hindered their advancement. As a 1-D material, CNT has some unique properties such as wide range of band gaps, and reduced carrier scattering, etc. As a result, CNT based IR sensors have the potential to work at room temperature or moderate low temperature with a high quantum efficiency, which is difficult for other MIR sensing materials to implement. Therefore the MIR response of the CNT based IR sensors is investigated in this section. However, since SWNT normally has a thin diameter, its bandgap is too large to detect MIR. Fortunately, MWNTs may have much smaller bandgap

than SWNTs because of their large diameter. Hence it is possible to detect MIR using MWNTs. Moreover, as discussed in section 4.2.1, the advantage of bandgap tunability makes MWNT a perfect material for building MIR sensors.

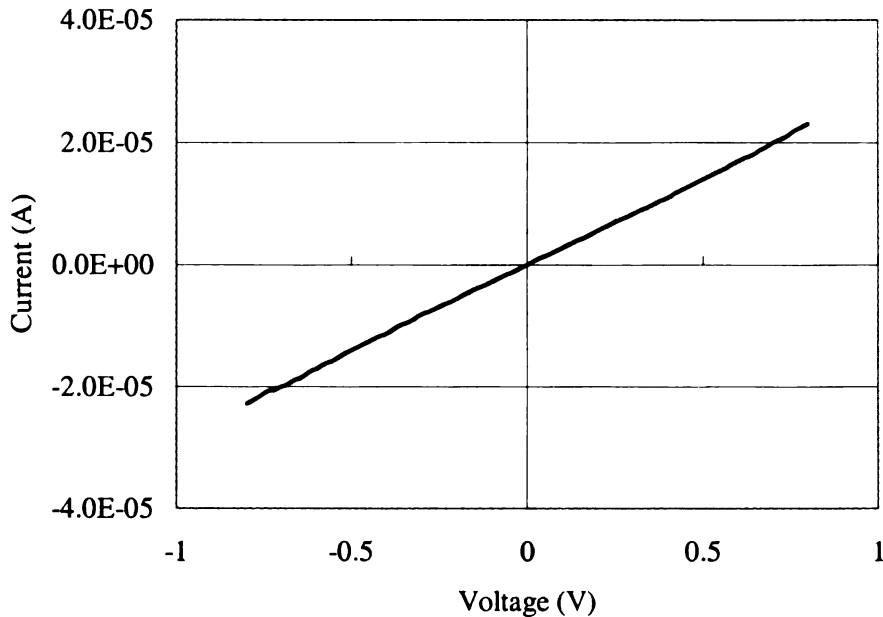


Figure 4.16. I-V characteristic curve of a MWNT MIR sensor

The I-V characteristic curve of a MWNT device is shown in Fig. 4.16. It can be seen that the I-V curve shows a metallic behavior. This MWNT device has been tested with both NIR and MIR. However, none of them could be detected. The reason is that the MWNT was too thick and its bandgap was almost zero. Hence the MWNT was a metallic CNT which made it insensitive to IR light. To make the MWNT device sensitive to MIR, its bandgap had to be adjusted such that the MWNT became a semiconducting CNT. By using the technology developed in section 4.2.1, the outer layers of the MWNT was electrically removed and the MWNT became a semiconducting CNT. Fig. 4.17 shows the I-V curve of the MWNT device after first breakdown. It can be observed that the I-V curve became curving. That was because that the semiconducting MWNT formed barriers at the MWNT-metal interfaces.

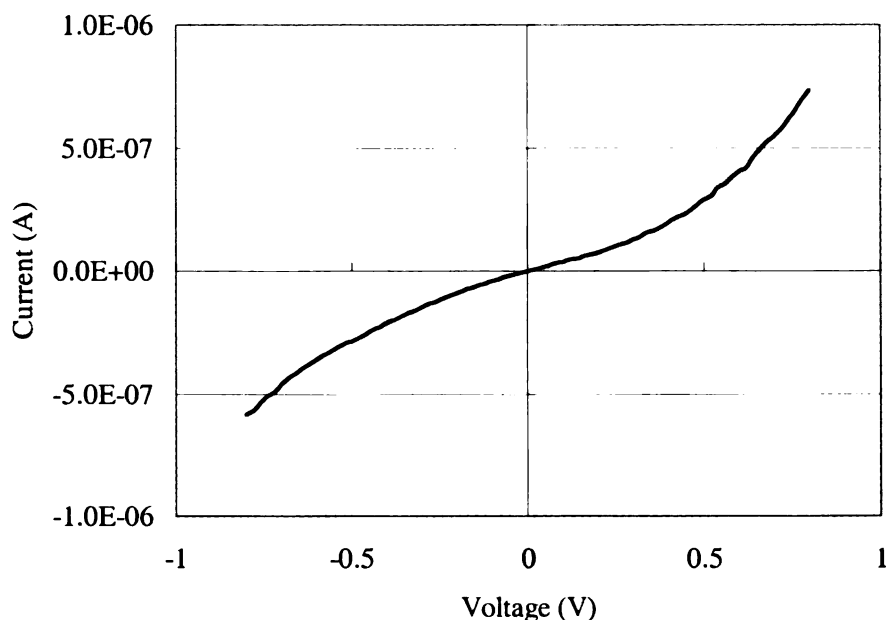


Figure 4.17. I-V characteristic curve of the MWNT MIR sensor after first breakdown

After the MWNT was tuned to a semiconducting MWNT, the NIR photoresponse was first tested. Fig. 4.18 shows the temporal photoresponse of the MWNT sensor when a NIR laser was periodically switched on and off. It can be observed that photocurrent responded to the IR illumination very quickly. During the measurement, a zero bias voltage was applied on the MWNT pixel. It means that the detected photocurrent was a short circuit current. Hence the MWNT should work as a photovoltaic device here. After taking measurements with the NIR, the MIR has also been tested by using a blackbody as the MIR source. An IR filter with a spectral range around $3 \mu m$ was used to block IR light with other wavelenghtes. However, there was no any signal detected when the MIR was switched on and off. Since the power density of the blackbody emission was much lower than the NIR laser, it was possible that the MIR signal had been submerged by noise.

To lower the noise and decrease dark current, the bandgap engineering process was carried out again to adjust the MWNT bandgap. Fig. 4.19 shows the I-V curve of the MWNT sensor after second breakdown. Obviously, the amplitude of the

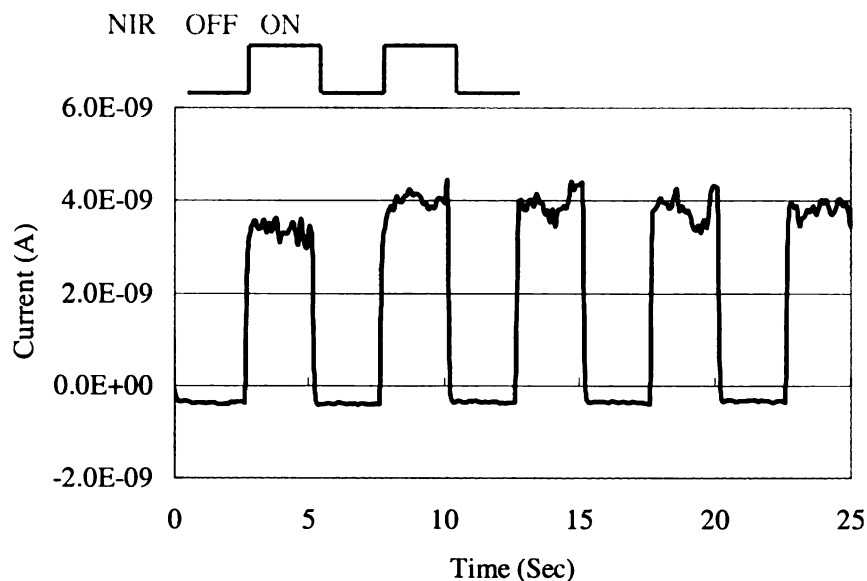


Figure 4.18. Temporal photoresponse of the MWNT sensor to NIR

current became much smaller and the I-V curve behaved like a diode. The reason is that the bandgap of the MWNT became larger after the second breakdown process. Hence the Schottky barriers at MWNT-metal interfaces also increased, which caused smaller noise level and dark current. After lowering the noise level and dark current, the MWNT was used to detect MIR again. Fig. 4.20 shows the temporal response of the MWNT sensor when the MIR was periodically switched on and off by using a mechanical chopper. It can be observed that the MIR response was quite different with the NIR response. When then MIR was turned on/off, the current suddenly increased/decreased and then gradually got back to the dark current level. This is because the MWNT formed two reversely connected Schottky barrier at MWNT-metal contacts. When the MWNT device was illuminated by IR, both Schottky diode generated electrons and holes. However, since there were two reversely connected Schottky diode, the photogenerated charges at one Schottky diode had to go through another one to form a photocurrent. Since the incident power density of the NIR was big enough to generate sufficient charges at each Schottky barrier and form a

large open circuit voltage at each Schottky diode, the photogenerated charges at one diode were able to tunnel through another diode and formed a photocurrent. That is why the photocurrent could keep its value after the NIR was switched on. But for the MIR, the incident power density was much smaller and could not generate enough charges at the Schottky diode to form a big open circuit voltage. Hence the photogenerated charges at one diode could not get through another diode to form a photocurrent. And the two Schottky barriers worked like two capacitors. When the MIR was switched on, the capacitors got charged and there was a suddenly current increase. But as time going, the charging current gradually reduced to zero. When the MIR was switched off, the capacitors discharged and there was a suddenly current decrease. And the discharging current gradually reduced to zero.

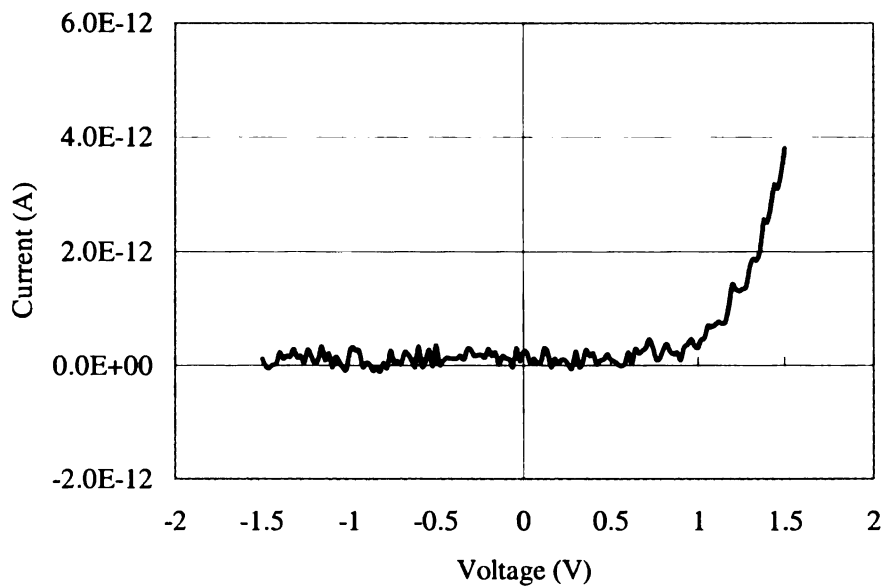


Figure 4.19. I-V characteristic curve of the MWNT MIR sensor after second breakdown

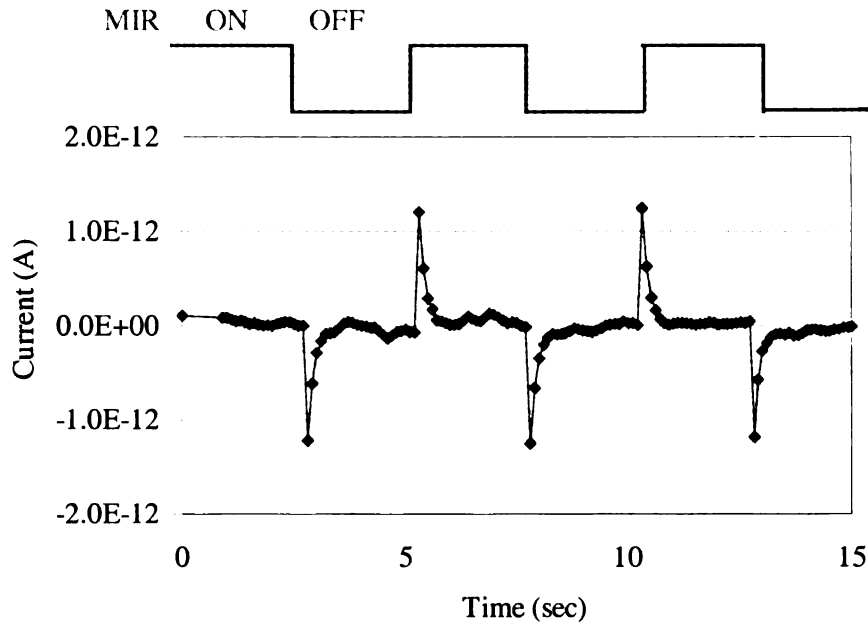


Figure 4.20. Temporal photoresponse of the MWNT sensor to MIR

4.6 Temperature Dependence of CNT Based IR Sensors

As a 1-D material, CNT has some unique properties such as wide range of band gaps, and reduced carrier scattering, etc. As a result, CNT based IR sensors have the potential to work at room temperature or moderate low temperature with a high quantum efficiency, which is difficult for other MIR sensing materials to implement. Hence it is important to characterize the CNT sensors at different temperatures.

Fig. 4.21 shows the I-V characteristic curves of a MWNT sensor at different temperatures. It can be observed that the dark current significantly dropped when the temperature was lowered to 200 K. Since this device was assembled by pushing the MWNT onto microelectrodes, the pushing process might induced defects on the MWNT and the contact condition might be bad as well. Hence the significant current drop upon temperature decrease might be because that the defects and contact

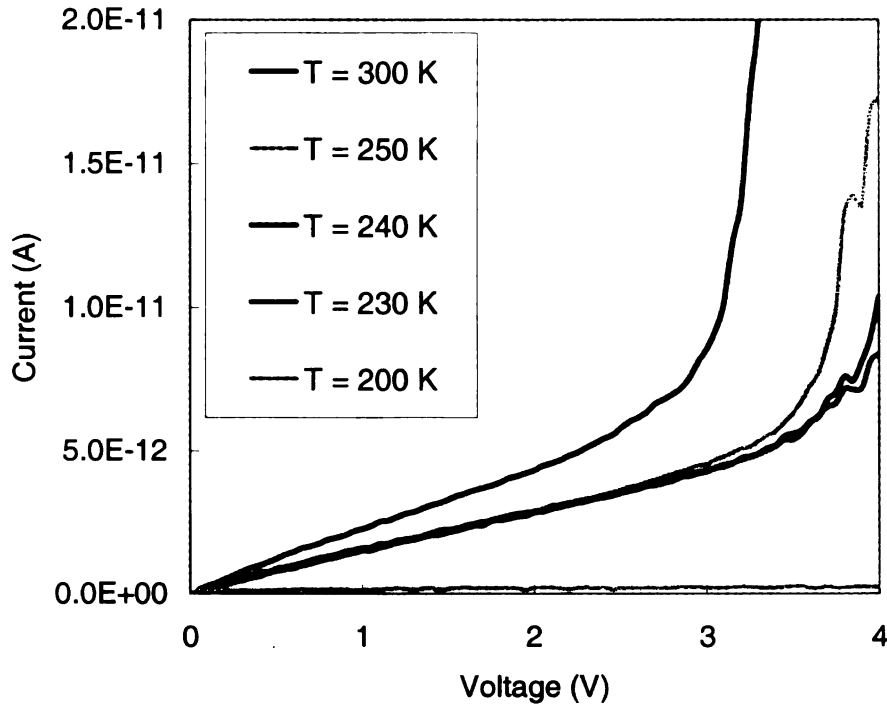


Figure 4.21. I-V characteristic curves of a MWNT sensor at different temperatures. The sensor was assembled through nanomanipulation.

condition became worse when the temperature was decreased. To verify this analysis, another MWNT sensor was assembled without nanomanipulation. The MWNT was directly deposited onto the microelectrodes through DEP deposition. Since no nanomanipulation was involved during the device fabrication, the defects on CNT should be minimized and the contact condition should be improved. The I-V curves of this MWNT sensor was also tested at different temperatures as shown in Fig. 4.22. It can be seen that the I-V curve did not change much when the temperature was lowered from 300 K to 180 K. Hence how to reduce the defects and improve the contact condition is an important issue for the CNT based nanodevices. A CNT IR sensor packaging process has been developed in [116]. After assembling a CNT onto the microelectrodes, the CNT device will be packaged for keeping good contact between CNT and microelectrodes. First of all, the CNT chip will be annealed in a

vacuum oven at $300\text{ }^{\circ}\text{C}$ to improve the contact between CNT and microelectrodes right after the fabrication. The defects induced during nanomanipulation can also be reduced through the annealing process. After that, a layer of parylene will be coated on the top of CNT to fix it and isolate it from environmental uncertainties.

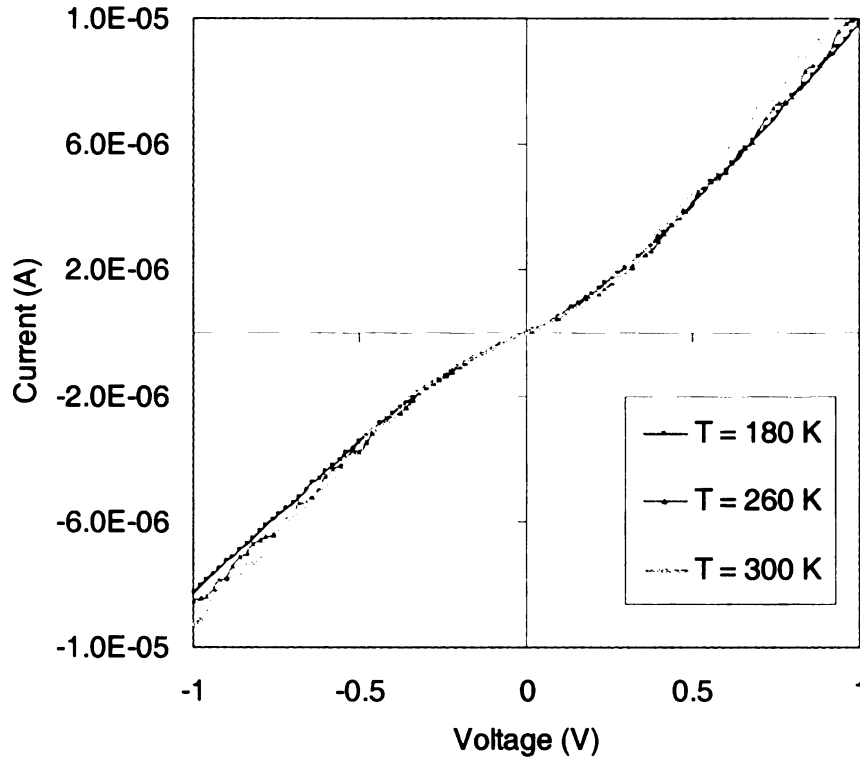


Figure 4.22. I-V characteristic curves of a MWNT sensor at different temperatures. The sensor was assembled without nanomanipulation.

4.7 Performance Evaluation and Analysis

IR response of the CNT based IR sensors have been experimentally tested in previous sections. Fig. 4.11 shows the temporal photoresponse of the symmetric CNT IR sensor when IR spot was on different locations. Fig. 4.12 shows the photocurrent of the symmetric CNT IR sensor as a function of the IR spot position. It can be ob-

served that the photocurrent changed from negative to positive continuously as the IR spot moved from left to right. Since the device was zero biased, the photocurrent must be generated by the photovoltaic effect. If the photocurrent was caused by the conductance change due to heating effect or photoconduction effect, it would not be able to change from positive to negative when the IR spot moved from left to right. Fig. 4.15 further proved this analysis with the perfect photodiode I-V characteristic curves. Based on this analysis, following sections evaluate some important properties of CNT based IR sensors, including response time, photocurrent, dark current, quantum efficiency and etc.

Response Time

To test the response time, the temporal photocurrent response of a SWNT device was measured with a sampling rate of 10 *kHz*, as shown in Fig. 4.23. Since it takes time to do integral at low current measurement range, the sampling rate will be very low in this situation. To reach the high sampling rate in this experiment, the current was measured by the Agilent 4156C with a current measurement range of 100 *nA*. But because the signal is at nano-ampere scale, the noise level became high in this result. From the plot it can be seen that the current increased immediately once the IR was switch on. The response time was at 100 μs level. Since the sampling time was 100 μs , it is possible that the response time was less than 100 μs .

Photocurrent and Dark Current

Since the CNT-metal contacts of the CNT based IR sensor are Schottky contacts, the photocurrent of the CNT sensor is calculated with a Schottky diode model by the following equation

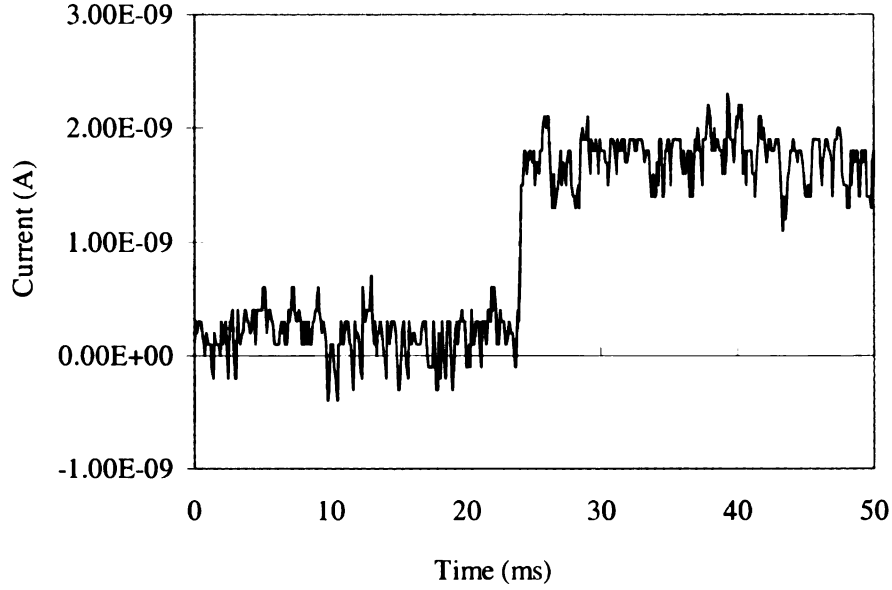


Figure 4.23. Temporal NIR photocurrent response of an individual SWNT IR sensor measured at high sampling rate

$$J_{ph} = (1 - R)qF_{pg}\eta \quad (4.1)$$

where R is the energy loss of photons due to reflection and absorption, q is the charge of electron, F_{ph} is the photon flux density, and η is the quantum efficiency of the Schottky diode. The spatial optical power distribution of the laser (PV-UH5-30G-830, World Star Tech.) is a Gaussian distribution. Hence, by assuming the laser spot center to be at one electrode, the optical power at the two electrodes can be calculated by Gaussian distribution equation. Let the total power be P , the power P_1 at the electrode where the spot center is located at is given by:

$$P_1 = 1/\sqrt{2\pi}P = 0.3989P \quad (4.2)$$

Assume that the laser spot size is $60 \mu m$ and the optical power at the edge is around $1 - 2\%$ of the total power. Let $x = 0$ at the spot center, the position of the spot edge ($x = 30 \mu m$) can be normalized as $x = 2.5$. Since the distance between the two electrodes is $3 \mu m$, x is normalized as $x_b = 0.25$ at the second electrode. Hence the optical power P_2 at the second electrode is calculated as:

$$P_2 = 1/\sqrt{2\pi} \exp(-x_b^2/2)P = 0.3867P \quad (4.3)$$

With equation 4.1, the photocurrent of a CNT sensor with symmetric gold electrodes (annotated by Au-Au) is calculated by:

$$\begin{aligned} J_{ph}(Au - Au) &= (1 - R)q(P_1\eta_{Au} - P_2\eta_{Au}) \\ &= (1 - R)qP(0.012\eta) \end{aligned} \quad (4.4)$$

For a CNT sensor with asymmetric gold-titanium electrodes (annotated by Au-Ti), the photocurrent is:

$$\begin{aligned} J_{ph}(Ti - Au) &= (1 - R)q(P_1\eta_{Ti} - P_2\eta_{Au}) \\ &= (1 - R)qP(0.3989\eta_{Ti} - 0.3867\eta_{Au}) \end{aligned} \quad (4.5)$$

Where the quantum efficiency is given by

$$\eta = 1 - \frac{\exp(-\alpha W_d)}{1 + \alpha L_p} \quad (4.6)$$

where α is the optical absorption coefficient, L_p is the diffusion length of holes, W_d is the depletion width of the Schottky barrier at CNT-metal interface. Here we suppose $\eta_{Ti} \approx 100 - 200\% \eta_{Au}$, then

$$\begin{aligned} J_{ph}(Ti - Au) &= (1 - R)q(P_1\eta_{Ti} - P_2\eta_{Au}) \\ &= (1 - R)qP\eta_{Au}(0.0122 \sim 0.4111) \end{aligned} \quad (4.7)$$

Hence the ratio of the photocurrent of asymmetric CNT sensors to the photocurrent of symmetric CNT sensors is

$$\frac{J_{ph}(Ti - Au)}{J_{ph}(Au - Au)} = \frac{(1 - R)qP\eta_{Au}(0.0122 \sim 0.4111)}{(1 - R)qP\eta_{Au}0.0122} = 1 \sim 33 \quad (4.8)$$

Our experimental results show a value of $J_{ph}(Ti - Au) \setminus J_{ph}(Au - Au)$ around 10, which is in the range of the theoretically estimated values. The dark current of a Schottky diode is calculated by

$$J_s = A^{**}T^2 e^{-q\phi_b/kT} \quad (4.9)$$

where A^{**} is the effective Richardson's constant, ϕ_b is the zero-bias barrier height, and n is the ideality factor. For a p-type CNT, the barrier height ϕ_b can be calculated by

$$\phi_b = X + E_g - \phi_m \quad (4.10)$$

Where X and E_g are the electron affinity and bandgap of CNT, respectively. ϕ_m is the work function of contact metal. Substituting equation 4.10 into 4.9, we can get

$$J_s = A^{**}T^2 e^{q(\phi_m - X - E_g)/kT} \quad (4.11)$$

Equation 4.11 shows that a contact metal with smaller work function will leads to a smaller dark current. It explains why the asymmetric Ti-Au CNT sensors have smaller dark current than the symmetric Au-Au sensors.

Quantum Efficiency

The quantum efficiency is defined as

$$QE = \frac{n_E}{n_p} \quad (4.12)$$

where n_E is the number of collected electrons, and n_p is the number of absorbed photons. The number of collected electrons can be calculated by

$$n_E = \frac{I_{ph}}{q} \quad (4.13)$$

where I_{ph} is the photocurrent and q is the electron charge. Using the photocurrent measured in section 4.4, n_E can be calculated as

$$n_E = \frac{I_{ph}}{q} = \frac{1.3 \times 10^{-10}}{1.6022 \times 10^{-19}} = 8.114 \times 10^8 S^{-1} \quad (4.14)$$

The number of photons absorbed by CNT is given by

$$n_p = \frac{P/A \times A_s}{E_{photon}} \quad (4.15)$$

where $P = 30mW$ is the total power of the IR source, $A = \pi(100\mu m)^2$ is the area of the IR spot, $A_s = (\text{length of CNT}) \times (\text{diameter of CNT})$ is the sensing area of the CNT sensor, E_{photon} is the photon energy and is given by

$$E_{photon} = h \times \frac{C}{\lambda} \quad (4.16)$$

where $h = 6.626 \times 10^{-34} J \cdot S$, is Plank's constant. $C = 3 \times 10^8 m \cdot S^{-1}$ is the light velocity. $\lambda = 830nm$ is the wavelength of the IR light. Hence, the number of absorbed photon is

$$\begin{aligned}
n_p &= \frac{30mW/[\pi \times (100\mu m)^2] \times (1.5nm \times 2.5\mu m)}{6.626 \times 10^{-34}J \cdot S \times [3 \times 10^8m \cdot S^{-1}]/830nm} \\
&= 1.495 \times 10^{10}S^{-1}
\end{aligned} \tag{4.17}$$

Then the quantum efficiency can be calculated as

$$QE = \frac{n_E}{n_p} = \frac{8.114 \times 10^8 S^{-1}}{1.495 \times 10^{10} S^{-1}} = 5.43\% \tag{4.18}$$

This value is consistent with the previous reported results [13, 117, 118]. Table 4.1 shows the quantum efficiency of different IR materials. It can be seen that the quantum efficiency of SWNT is still lower than other well developed IR materials. The low quantum efficiency of the SWNT is due to its thin diameter. Most of the photons which reach the SWNT surface will pass through the SWNT wall without exciting the electron-hole pairs. Hence, further study on the structure of CNT based IR sensors is expected for improving the quantum efficiency.

Table 4.1. Quantum efficiency of different IR materials

	Wavelength (μm)	Quantum efficiency
Quantum Well Infrared Photodetector	3-20	0.32
Quantum Dot Infrared Photodetector	4.7-5.2	0.0002
InSb	3-5	0.3-0.8
SWNT	2.2	0.054

4.8 Chapter Summary

The development of a cryogenic IR sensor testing system and testings of different single CNT based IR sensors are discussed in this chapter. Both MWNT sensors and SWNT sensors have been tested and evaluated. MWNT sensors showed a higher quantum efficiency and bigger photocurrent than SWNT sensors. But the dark current of MWNT sensors was also much higher than the dark current of SWNT sensors. Hence the SWNT sensors were studied to get a higher signal-to-dark current ratio. SWNT sensors have been fabricated with symmetric structure and asymmetric structure respectively. Experimental testing results show that the asymmetric CNT-metal contacts can improve the performance of the photodiodes by increasing the SDR up to two orders of magnitude higher than the symmetric ones. Hence, SWNT has strong potential for applications of NIR detection. With its bandgap tunability, MWNTs have been studied for MIR detection. By electrically removing the outer layers of a MWNT, the bandgap of the MWNT was adjusted and the IR response was tested. Detection of MIR using MWNT IR sensor has been demonstrated in this chapter.

CHAPTER 5

Multi-Pixel CNT Sensor Array

Different technologies have been developed for IR detection, such as uncooled microbolometer [119], quantum dot photodetector [120], etc. IR focal plane arrays (IRFPAs) have also been fabricated based on those technologies [121, 122]. However, the low resolution is still a major difficulty for IRFPAs. Due to the fabrication difficulties and the thermal crosstalk between adjacent pixels, the pixel pitch of the traditional IRFPAs is limited to be around several tens of micrometers [122, 123]. Hence, it is necessary to explore the possibility of reaching smaller pixel pitch using new nanotechnology and nanomaterials such as CNT. In this study, a CNT based three-pixel IR sensor with $10\ \mu\text{m}$ pixel pitch will be fabricated and tested. With the technologies to fabricate multi-pixel CNT sensor array, CNT based multi-color IR sensor will also be fabricated by assembling CNTs with different diameter onto the adjacent pixels.

5.1 Fabrication of Single CNT based IR Sensor Array

Though much work has been done on the photoconductivity of CNTs, few researchers successfully fabricated CNT based multi-pixel sensors, which is important for CNT's further application in IR sensing. As discussed in Chapter 1, current available methods have their shortcomings in terms of repeatability, mass production, and ability in eliminating uncertainties. It is difficult to fabricate CNT based sensor array in a reliable and controllable manner with those methods. In this study, an automated nanomanufacturing process is developed for building single CNT based multi-pixel IR sensors.

Fig. 5.1 shows the developed automated nano-manufacturing process for single CNT sensor arrays. Firstly, the microelectrodes with a submicrometer gap are fabricated with the photolithography method. Then the automated DEP deposition system is used to deposit individual CNTs around each pixel. After trapping one or more individual CNTs around each pixel, the AFM based nanorobotic manipulation will be performed to re-position the CNTs to make connections with microelectrodes and push the rest CNTs away. Detailed DEP deposition process and AFM manipulation process have been discussed in Chapter 3.

The structure of a single pixel CNT based IR sensor is shown in Fig. 5.2(a). Fig. 5.2(b) shows the 3D AFM image of a three-pixel CNT IR sensor array without CNT deposited. The pixel pitch of each pixel is $10\ \mu m$. A single CNT will be assembled onto each pair of microelectrodes to make a connection with the automated nanomanufacturing process.

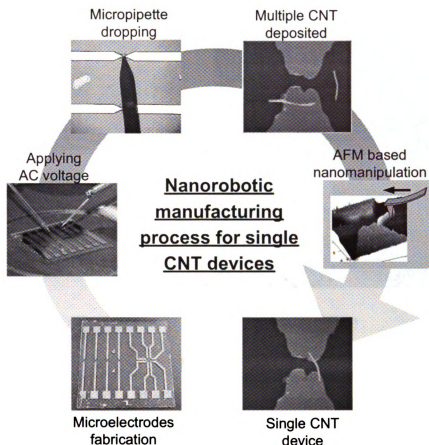


Figure 5.1. Nano-manufacturing process for single CNT based nanodevices.

5.2 Testing of Multi-Pixel CNT Sensor Array

The SWNT in our experiments was obtained from BuckyUSA, Inc., and synthesized by the arc discharge method. The current signal from the sensor was measured with an Agilent 4156C Precision Semiconductor Parameter Analyzer. The IR response of the CNT sensor was measured with a near-IR laser (UH5-30G-830-PV, World Star Tech) with a wavelength of 830 nm and power of 30 mW.

Fig. 5.3 shows the AFM image of a three-pixel CNT IR sensor array. Single-walled carbon nanotubes (SWNTs) were assembled to each pixel using the developed nanomanufacturing process.

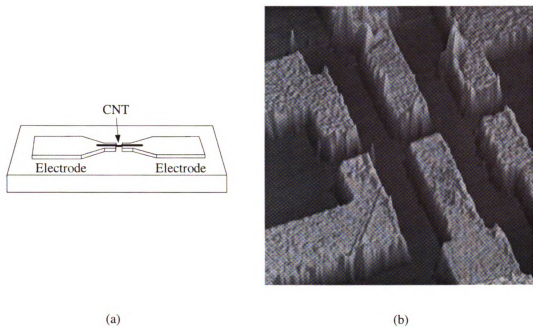


Figure 5.2. (a) The structure of a single pixel CNT IR sensor. (b) The 3D AFM image of a three-pixel CNT IR sensor array.

First of all, the I-V characteristic curves of each pixel were measured as shown in Fig. 5.4. It can be seen that the I-V behavior of each pixel varies because of the nonuniformity of CNTs. Therefore, it is necessary to normalize the photocurrent of each pixel into a same scale for comparison. By scanning the IR spot around each pixel, the maximum photocurrent $I_{ph,i}^{max}$ (where $i=1,2,3$ is the index of pixels) of that pixel was measured when the IR spot was aligned to the pixel. For each pixel, the photocurrent $I_{ph,i}$ can be normalized by the equation $I_{ph_norm,i} = I_{ph,i}/I_{ph,i}^{max}$. As shown in Fig. 5.5, the temporal photocurrent responses of each pixel were tested while the IR spot was on each pixel respectively. Fig. 5.6 shows the photocurrent responses while the IR spot was on pixel 1 and the IR source was periodically switched on and off. The photocurrent of pixel 1 $I_{ph_norm,1}$ was at its maximum value and the photocurrent of pixel 2 and 3 ($I_{ph_norm,2}$ and $I_{ph_norm,3}$) were getting smaller as the pixels were getting away from the IR spot. Since all the pixels were zero biased

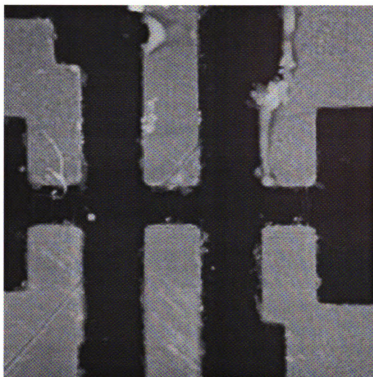


Figure 5.3. The AFM image of the three-pixel CNT IR sensor.

during IR measurements, the photocurrents were generated by the photovoltaic effect, which is caused by the Schottky contact at CNT-metal interface. As shown in Fig. 5.7, $I_{ph_norm_2}$ increased to around 1 and the photocurrent of pixel 1 and 3 became smaller because the IR spot was on pixel 2. The reason that the photocurrent of pixel 1 and 3 did not become zero is that the diameter of the IR spot was big enough to cover all three pixels. Fig. 5.8 shows the photocurrents while the IR spot center was on pixel 3. $I_{ph_norm_3}$ increased to around 1 while $I_{ph_norm_1}$ and $I_{ph_norm_2}$ getting smaller. These IR response measurements verified that the CNT IR sensor array is able to detect the spatial variance of incident IR power density with a small pixel pitch.

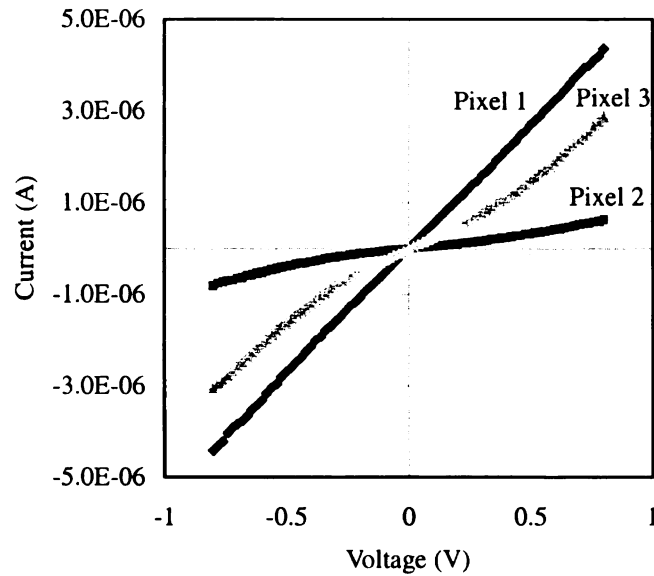


Figure 5.4. I-V curves of the three pixels.

5.3 CNT based Multi-color IR Sensors

Multicolor (multispectral) IR sensing is very important to advanced IR sensor systems in the applications of remote sensing, environment monitoring, medical diagnostics, as well as defense and aerospace applications. An IR sensor with multicolor capability can offer a better target discrimination, tracking, and identification, as well as temperature determination. Multicolor IR sensors are also very useful in industry for gas

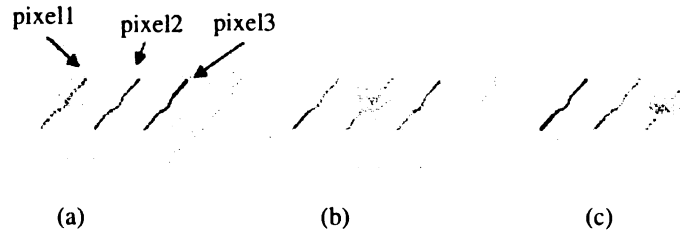


Figure 5.5. Illustration of the photocurrent measurements. IR spot was on (a) pixel 1, (b) pixel 2 and (c) pixel 3 respectively.

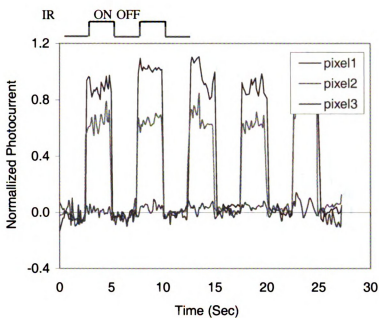


Figure 5.6. Temporal photocurrent response of each pixels while the IR spot was on pixel 1 (Fig. 5.5(a)).

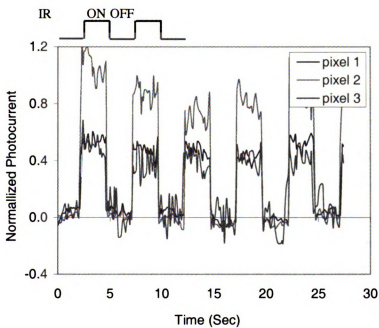


Figure 5.7. Temporal photocurrent response of each pixels while the IR spot was on pixel 2 (Fig. 5.5(b)).

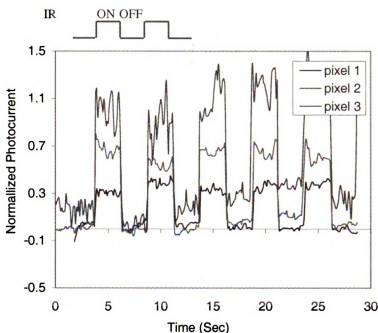


Figure 5.8. Temporal photocurrent response of each pixels while the IR spot was on pixel 3 (Fig. 5.5(c)).

leakage detection, chemical analysis, and for environmental sensing and control. As the IR technology continues to advance, there is a growing demand of multicolor IR sensors for advanced IR sensor systems. However, the difficulties in fabricating multicolor IR sensors have hindered its development and applications. The traditional multicolor IR sensors can be classified into two categories based on their structures. The first type of multicolor IR sensor is fabricated by building multiple IR sensing layers using different materials which are sensitive to IR with different wavelengths. Another type of multicolor IR sensor consists of multiple IR sensors which can detect light with different lengths. And a prism system is used to diffract light with desired wavelength to the corresponding sensor. Obviously, the available multicolor IR systems are complicated and difficult to make. As one of the promising nanomaterials that shows strong potential in IR detection, CNT has the advantage of bandgap tunability, which makes it a perfect material for multicolor detection.

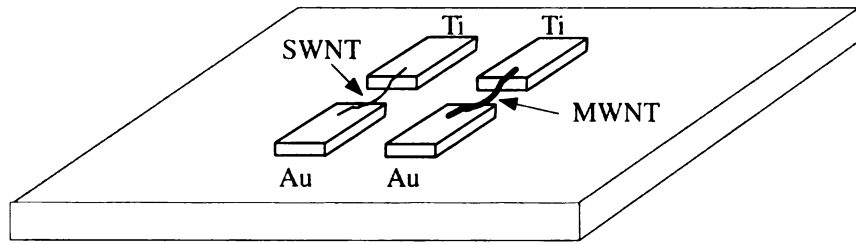


Figure 5.9. Structure of the multicolor CNT IR sensor

As discussed in Chapter 4.2.1, the diameter of a MWNT can be adjusted by electrically breaking down the outer layers. Since the bandgap of a semiconducting MWNT is reversely proportional to its diameter, the bandgap of a MWNT can be increased by breaking outer layers. Hence, a multicolor IR sensor can be fabricated from MWNT arrays by electrically tuning the bandgap of certain pixels. Since this fabrication process involves only one IR material, and the bandgap tuning process can be performed at the device level, the fabrication of multicolor IR sensor becomes much easier.

Fig. 5.9 shows the structure of the CNT based multicolor IR sensor. It consists of two pairs of microelectrodes. Here the asymmetric structure is used to improve the sensitivity as discussed in Chapter 2.3. One pair of the microelectrodes is bridged by a semiconducting SWNT and another is bridged by a metallic MWNT. Since the SWNT has a bandgap in the near IR band, it is used to detect IR. By electrically removing the outer layer of the metallic MWNT, the MWNT can be tuned into a semiconducting MWNT with small bandgap. By controlling the bandgap tuning process, we can get an appropriate bandgap for detecting MIR. Obviously, we can also put a MWNT on another pixel. Then we can have the bandgap of both pixels tunable. It provides more flexibility for building multicolor IR sensors.

With the same procedure of fabricating multi-pixel CNT IR sensors, we have fabricated prototype of the multicolor CNT IR sensor by depositing a SWNT on one pixel

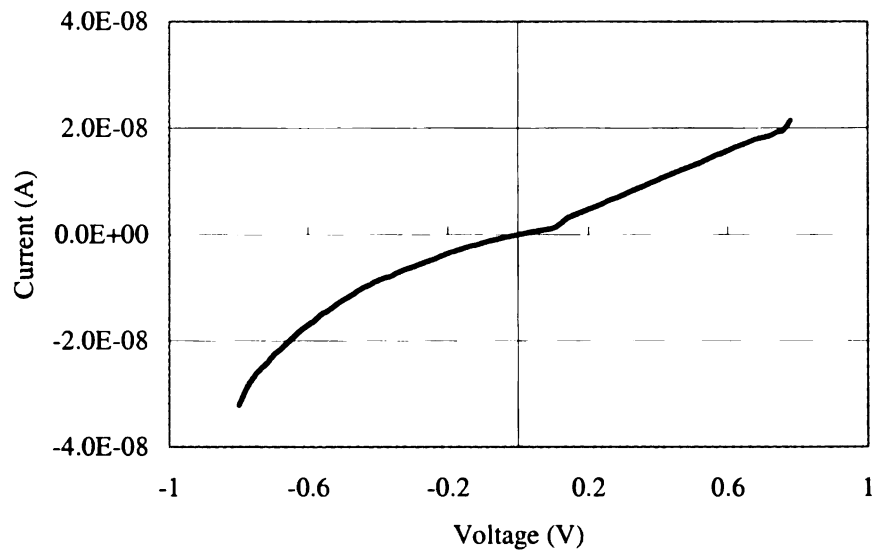


Figure 5.10. I-V characteristic curve of the SWNT pixel of the multicolor CNT IR sensor

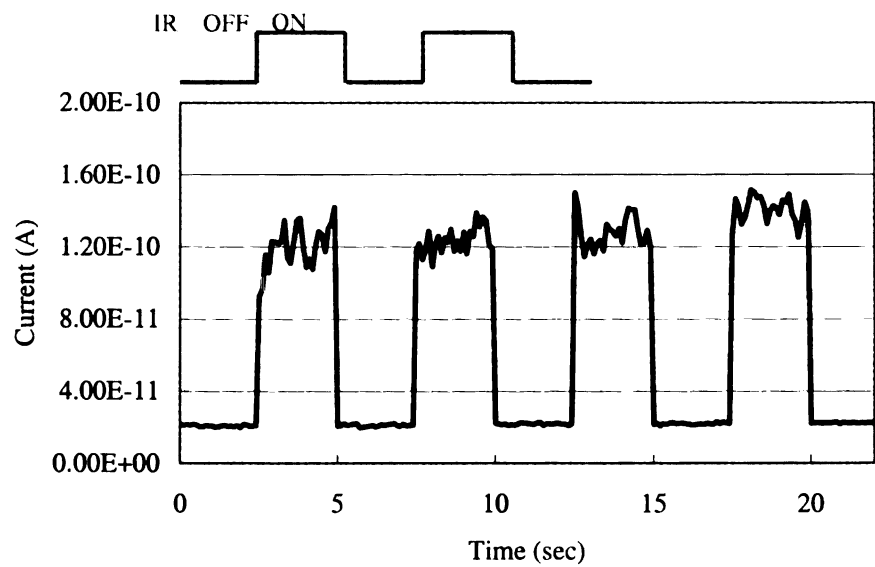


Figure 5.11. NIR response of the SWNT pixel of the multicolor CNT IR sensor

and a MWNT on the adjacent pixel. Both the SWNT and the MWNT were obtained from BuckyUSA, Inc. First of all, we tested the SWNT pixel. Since the semiconducting SWNT formed Schottky barriers at the CNT-metal interface. As shown in Fig. 5.10, the I-V curve of the SWNT pixel behaves like two reversely connected Schottky diodes. The photobehavior of the SWNT pixel was tested with the same procedure as discussed in Chapter 4. Fig. 5.11 shows the temporal photoresponse of the SWNT pixel. A NIR laser (UH5-30G-830-PV, World Star Tech) with a wavelength of 830 *nm* and power of 30 *mW* was used as the IR source. The laser source was periodically switched on and off, and no bias voltage was applied across the SWNT pixel. It can be observed that the photocurrent immediately increased/decreased when the NIR was switched on/off. The SWNT pixel has also been tested for MIR band with a blackbody (Oriol 67030). However, since the bandgap of the SWNT was too large to detect MIR photons, there was no any signal detected.

The electronic and photonic properties of the MWNT pixel has also been tested. Fig. 5.12 shows the I-V characteristic curve of the MWNT pixel. It can be seen that the MWNT showed a metallic behavior and the resistance was quite small. Since a metallic MWNT would not form Schottky barriers at the MWNT-metal contacts, the MWNT pixel could not detect any IR light. Experiments has been carried out to test the photoresponse of this MWNT pixel with both NIR and MIR. But there was no any signal detected. To active this MWNT pixel for IR detection, the MWNT bandgap engineering process discussed in Chapter 4.2.1 has been performed to adjust the electronic and photonic properties of the MWNT. By electrically burning the outer layers of the MWNT, the bandgap of the MWNT became bigger and its I-V curve became more semiconducting. Fig. 5.13 shows the I-V characteristic curve of the MWNT pixel after bandgap engineering. Since the MWNT became semiconducting and formed Schottky barrier at the MWNT-metal interfaces, the MWNT pixel behaved like two reversely connected Schottky diode.

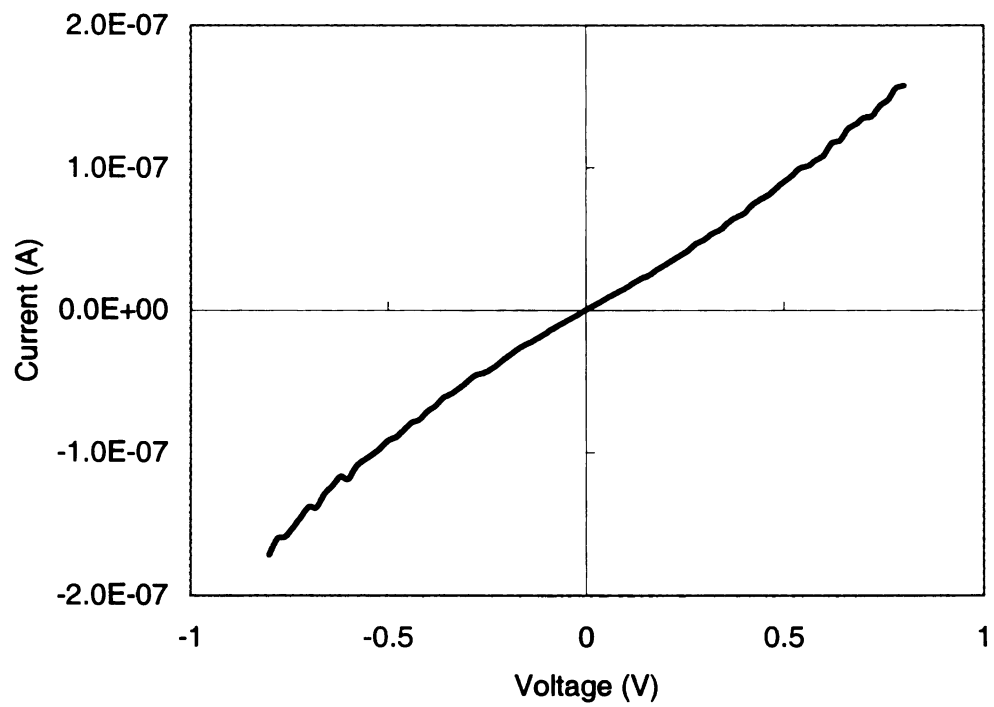


Figure 5.12. I-V characteristic curve of the MWNT pixel of the multicolor CNT IR sensor

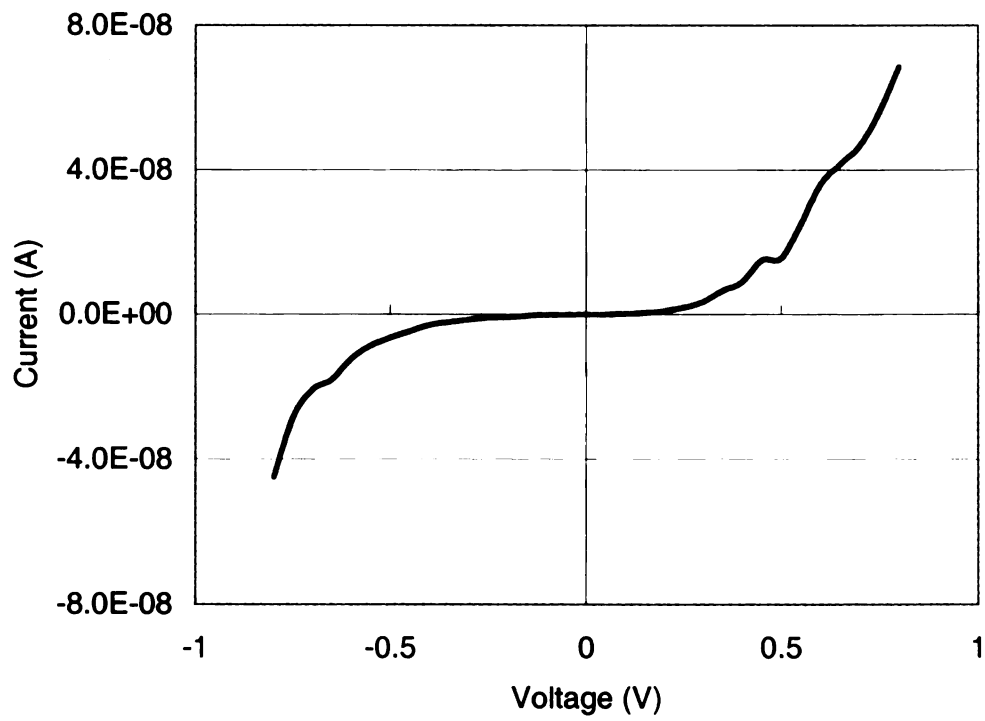


Figure 5.13. I-V characteristic curve of the MWNT pixel after breaking down outer layers

After tuned the bandgap of the MWNT pixel, experiments was carried out to test the photoresponse of the MWNT pixel. First of all, NIR laser source was used for the IR testing. Fig. 5.14 shows the temporal IR response of the MWNT pixel when the NIR laser was periodically switch on and off. It can be observed that the photocurrent responses to the IR illumination very quickly. During the measurement, a zero bias voltage was applied on the MWNT pixel. It means that the detected photocurrent was a short circuit current. Hence the MWNT should work as a photovoltaic device here. After taking measurements with the NIR, the MIR has also been tested by using a blackbody as the MIR source. An IR filter with a spectral range around $3 \mu m$ was used to block IR light with other wavelengthes. Fig. 5.15 shows the temporal response of the MWNT pixel when the MIR was periodically switched on and off by using a mechanical chopper. It can be observed that the MIR response was quite different with the NIR response. When then MIR was turned on/off, the current suddenly increased/decreased and then gradually got back to the dark current level. As discussed in Chapter 4, this is because the MWNT formed Schottky barrier at the contact of both end with the metal electrodes. The two Schottky diodes reversely connected. When the MWNT device was illuminated by MIR, both Schottky diode generated electrons and holes. However, since there were two reversely connected Schottky diode, the photogenerated charges at one Schottky diode had to go through another one to form a photocurrent. Since the incident power density of the NIR was big enough to generate sufficient charges at each Schottky barrier and form a big open circuit voltage at each Schottky diode, the photogenerated charges at one diode were able to tunnel through another diode and formed a photocurrent. That is why the photocurrent could keep its value after the NIR was switched on. But for the MIR, the incident power density was much smaller and could not generate enough charges at the Schottky diode to form a big open circuit voltage. Hence the photogenerated charges at one diode could not get through another diode to form a

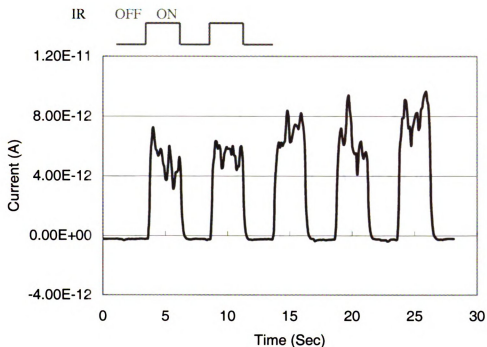


Figure 5.14. NIR response of the MWNT pixel of the multicolor CNT IR sensor

photocurrent. And the two Schottky barriers worked like two capacitors. When the MIR was switched on, the capacitors got charged and there was a suddenly current increase. But as time going, the charging current gradually reduced to zero. When the MIR was switched off, the capacitors discharged and there was a suddenly current decrease. And the discharging current gradually reduced to zero.

5.4 Chapter Summary

A three-pixel CNT based IR sensor array with $10\ \mu\text{m}$ pixel pitch has been fabricated using the developed nanomanufacturing process. The experimental testing on the electronic and photonic properties of each pixel shows that CNT formed a Schottky junction with the contact metal. And the photovoltaic effect of each Schottky junction was used to detect IR. It has also been shown that the CNT sensor array is able to

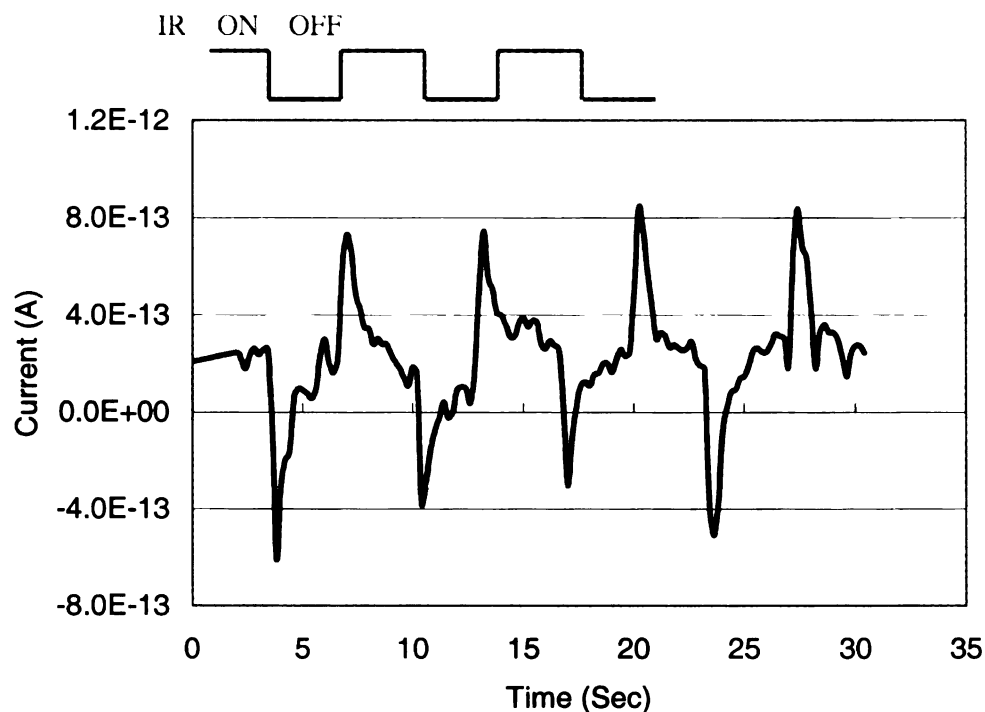


Figure 5.15. MIR response of the MWNT pixel of the multicolor CNT IR sensor

detect spacial variance of incident IR power density and has small thermal cross talk between adjacent pixels, which makes CNT a promising material for high resolution IRFPAs. More importantly, the fabrication of the single CNT based IR sensor array demonstrated the strong ability of the nanomanufacturing system. As the first CNT based IR sensing array, it is also a significant advancement in the application of the CNT based nanodevices.

With the technologies for fabricating multi-pixel CNT sensor array, CNT based multi-color IR sensors have also been demonstrated by having two pixels which can detect IR with different wavelenghtes. With its small diameter and relatively large bandgap, a SWNT was used for NIR detection. Since the bandgap of CNT is reversely proportional to its diameter, the bandgap of a MWNT can be tuned by electrically breaking its outer layers. With the bandgap tunability, a MWNT has been successfully engineered from a metallic MWNT into a semiconducting MWNT for MIR de-

tection. This multicolor CNT IR sensor first demonstrated the application of CNTs in multicolor detection. It further demonstrated that CNTs have strong potential for applications in the area of remote sensing, environment monitoring, defense and aerospace applications, and etc.

CHAPTER 6

Conclusions

As the traditional silicon based semiconductor industry faces increasing technological and financial challenges on the way to further scaling down, new technologies and concepts have to be developed and assessed. Nanotechnology is such a candidate and is likely to be the engine for the future advancement in the fields of electronics, energy science, biomedical science, materials, and etc. Nanomanufacturing and nanoelectronic devices are two of most important subdivisions of nanotechnology.

In this research, a nanomanufacturing process, which is able to fabricate single CNT as well as other nanomaterials (such as nanowire, DNA, nanoparticle, etc.) based nanodevices, was designed and experimentally tested. This technology will greatly facilitate researcher's exploration in the nano world by providing an efficient and reliable manner to handle nanomaterials and build nanodevices. With this technology, single CNT based infrared sensors have been designed and implemented. CNT sensors with different CNT-metal contacts have been fabricated and tested. The studies of CNT-metal contacts and the CNT based Schottky diode not only help improve the performance of CNT based infrared sensors, but also are important for other CNT based nanoelectronic devices which utilize the CNT Schottky diode.

With the asymmetric CNT-metal contact structure, SWNT devices have been

fabricated and characterized. SWNTs show a strong potential for applications of NIR detection and solar collection. Since SWNTs are limited by their thin diameters to detect NIR or lights with shorter wavelength, MWNTs have been studied for MIR detection. A bandgap engineering technology has been developed to adjust the bandgap of a MWNT by electrically removing outer layers of the MWNT. With this technology, detection of MIR using MWNT sensors have been demonstrated in this thesis. It is the first single CNT device which is able to detect MIR.

Moreover, CNT based multipixel IR sensor arrays have been fabricated and tested. The CNT multipixel IR sensor array shows promising properties such as small pixel pitch and low crosstalk. It is also the first time that a CNT device array can be fabricated in a reliable and controllable manner, which means the number of CNTs on each pixel, and the properties of each CNTs can be controlled during the fabrication process. With the bandgap engineering technology and the ability to build CNT device array, a CNT based multicolor IR sensor has also been firstly demonstrated. The CNT based multicolor IR sensor further expands CNT's application into those fields which need advanced IR sensor systems for a better target discrimination, tracking, and identification, as well as temperature determination.

6.1 Major Contribution

In summary, this thesis has developed a nanomanufacturing system, which is a significant contribution in handling nanomaterials and building nanodevices. It provides a reliable and efficient way for assemble nanodevices, especially CNT and nanowire based nanodevices. This nanomanufacturing system enables the fabrication of single CNT/nanowire based nanodevice arrays, which was difficult to achieve with other nanofabrication methods.

Moreover, as another main contribution, CNTs have been thoroughly studied for

IR detection. The role of CNT-metal contacts in the CNT based IR sensors was firstly studied for thoroughly understanding photodetection theory of CNT IR sensors and improving the performance of CNT IR sensors. Based on the study of CNT-metal contacts, the signal-to-dark current ratio as well as quantum efficiency have been significantly improved with an asymmetric structure.

The third major contribution is that a bandgap engineering process has been developed to tune the bandgap of MWNTs for MIR detection. Quantum detection of MIR using individual MWNT was first demonstrated in this dissertation. The individual MWNT based MIR sensor has much higher sensitivity and faster response speed than the previously reported MWNT film based MIR bolometer.

The last major contribution is that single CNT based multipixel IR sensor array and multicolor IR sensor have been firstly demonstrated in the world. CNTs have shown a strong potential of applications in the fields of solar collection, remote sensing, environmental monitoring, medical diagnostics, as well as defense and aerospace applications.

6.2 Future Research

The future research will focus on two directions. Firstly, it is necessary to further improve the quantum efficiency of the CNT based IR sensors. As discussed in Chapter 4, though the developed CNT IR sensor dramatically outperformed the other reported results, its quantum efficiency is still difficult to compete with traditional IR materials. Further studies on the CNT itself and sensor structure are necessary to improve the performance of CNT based IR sensors. Another future research direction will be developing real IRFPAs. This dissertation has demonstrated the CNT based three-pixel IR sensor arrays. But it is still far away from real IRFPA applications. Hence it is necessary to further improve the nanomanufacturing technologies to make high

density IRFPAs.

REFERENCES

Author's Publications

1. Jiangbo Zhang, Ning Xi, Hongzhi Chen, Wai Chiu King Lai, Guangyong Li, U.C. Wejinya, Design, Manufacturing and Testing of Single Carbon Nanotube Based Infrared Sensors, *IEEE Trans. Nanotechnology*, *accepted for publication*, 2008.
2. Jiangbo Zhang, Ning Xi, Hongzhi Chen, Wai Chiu King Lai, Guangyong Li, U.C. Wejinya, Photovoltaic Effect in Single Carbon Nanotube Based Schottky Diodes, *Int. J. of Nanoparticles*, *accepted for publication*, 2008.
3. Jiangbo Zhang, Ning Xi, Lianqing Liu, Hongzhi Chen, King W.C. Lai, Guangyong Li, Atomic Force Microscope Based Nano Robotic System for Nanomanipulation, *IEEE Nanotechnology Magazine*, *accepted for publication*, 2008.
4. U. C. Wejinya, Ning Xi, Yantao Shen, King W. C. Lai, Jiangbo Zhang, An Efficient Approach of Handling and Deposition of Micro and Nano Entities Using Sensorized Microfluidic End-Effector System, *Sensor and Actuators*, *accepted for publication*, 2008.
5. Lianqing Liu, Yilun Luo, Ning Xi, Jiangbo Zhang, Guangyong Li, Sensor Referenced Real-Time Videolization of Atomic Force Microscopy for Nano Manipulations, *IEEE/ASME transactions on mechatronics*, *accepted for publication*, 2008.
6. W. C. King Lai, Ning Xi, Jiangbo Zhang, Hongzhi Chen, Yilun Luo, Uchekukwu C. Wejinya, Automated Nanomanufacturing System to Assemble Carbon Nanotube Based Devices, *International Journal of Robotics Research*, *accepted for publication*, 2008.
7. Jiangbo Zhang, Ning Xi, and King Lai, Single Carbon Nanotube Infrared Detectors, *Nanotechnology*, *SPIE Newsroom (newsroom.spie.org)*, Jan. 5, 2007.
8. Jiangbo Zhang, Ning Xi, Guangyong Li, Ho-Yin Chan, and U.C. Wejinya, Adaptable End Effector for Atomic Force Microscopy Based Nanomanipulation, *IEEE Transactions on Nanotechnology*, 5(6):628-642, 2006

9. Jiangbo Zhang, Ning Xi, Hongzhi Chen, King W.C. Lai, Yilun Luo, Carbon Nanotube based Infrared Detector Array, *IEEE International Conference on Nanotechnology, accepted, 2008*
10. Jiangbo Zhang, King W.C. Lai, Jeffri Narendra, Ning Xi, Timothy Grotjohn, Jes Asmussen, Computer Integrated Plasma Nano Manufacturing Workcell, *IEEE International Conference on Nanotechnology, accepted, 2008*
11. Jiangbo Zhang, Ning Xi, Hongzhi Chen, and King W. C. Lai, Fabrication and Experimental Testing of Individual Multi-walled Carbon Nanotube (CNT) based Infrared Sensors, *Proceeding of the 6th IEEE International Conference on Sensors*, Oct. 28 - 31, 2007, Atlanta, GA.
12. Lianqing Liu, Ning Xi, Yilun Luo, Jiangbo Zhang, and Guangyong Li, Sensor Referenced Guidance and Control for Robotic Nanomanipulation, *Proceeding of the IEEE/RSJ 2007 International Conference on Intelligent Robots and Systems*, Oct. 29 Nov. 2, 2007, San Diego, CA.
13. Lianqing Liu, Jiangbo Zhang, Guangyong Li, and Ning Xi, On-line Sensing and Display in Atomic Force Microscope Based Nanorobotic Manipulation, *Proceeding of the 2007 IEEE/ASME International Conference on Advanced Intelligent Mechatronics*, Sept. 4-7, 2007, ETH Zrich, Switzerland
14. Jiangbo Zhang, Ning Xi, King W. C. Lai, Hongzhi Chen, Yilun Luo, and Guangyong Li, Single Carbon Nanotube based Photodiodes for Infrared Detection, *Proceeding of the 7th IEEE International Conference on Nanotechnology*, Aug. 2 - 5, 2007, Hong Kong.
15. Lianqing Liu, Ning Xi, Yilun Luo, Jiangbo Zhang, and Guangyong Li, Real-time Position Error Detecting in Nanomanipulation Using Kalman Filter, *Proceeding of the 7th IEEE International Conference on Nanotechnology*, Aug. 2 - 5, 2007, Hong Kong.
16. King W. C. Lai, Ning Xi, Jiangbo Zhang, Guangyong Li, and Hongzhi Chen, Packaging Carbon Nanotube Based Infrared Detector, *Proceeding of the 7th IEEE International Conference on Nanotechnology*, Aug. 2 - 5, 2007, Hong Kong.
17. Guangyong Li, Lianqing Liu, Ning Xi, Jiangbo Zhang and King W. C. Lai, Study of DNA Properties under Controlled Conditions Using AFM Based Nano-Robotics, *Proceeding of the 7th IEEE International Conference on Nanotechnology*. August 2-5, 2007, Hong Kong.
18. Lina Hao, Jiangbo Zhang, and Ning Xi, A Controller for Adaptable End Effector of the AFM Based Nano-Robotic System, *Proceeding of the 7th IEEE International Conference on Nanotechnology*, Aug. 2 - 5, 2007, Hong Kong.

19. Lina Hao, Jiangbo Zhang and Ning Xi, Optimal Periodic-Output-Feedback Control of Active AFM Probe for Nanomanipulation, *Proceeding of the European Control Conference 2007*, July 2-5, 2007, Kos, Greece
20. Jiangbo Zhang, Ning Xi, Hongzhi Chen and King W.C. Lai, Efficient readout for carbon nanotube (CNT)-based IR detectors, *Proc. SPIE Int. Soc. Opt. Eng.* 6737, 673711 (2007).
21. Ning Xi, Jiangbo Zhang, Harold Szu, and Guangyong Li, Nanorobot assembly of Carbon Nanotubes for Mid-IR sensor, *Proc. SPIE Int. Soc. Opt. Eng.* 6576, 65760K (2007)
22. Jiangbo Zhang, Ning Xi and King W.C. Lai, Performance Evaluation and Analysis for Carbon Nanotube (CNT) based IR Detectors, *Proc. SPIE Int. Soc. Opt. Eng.* 6542, 65421N (2007)
23. Lina Hao, Jiangbo Zhang, and Ning Xi, The Infinite Dimensional Control of Flexible Cantilevers in AFM Based Nanomanipulation, *Proceeding of the 2nd IEEE International Conference on Nano-Micro Engineered and Molecular Systems*, Jan. 16-19, 2007, Bangkok, Thailand
24. Jiangbo Zhang, Ning Xi, Hoyin Chan, and Guangyong Li, Single Carbon Nanotube based Infrared Sensor, *Proc. SPIE Int. Soc. Opt. Eng.* 6395, 63950A (2006)
25. Jiangbo Zhang, Ning Xi, Hoyin Chan, Guangyong Li, Single Carbon Nanotube Based Ion Sensor for Gas Detection, *Proceeding of the 6th IEEE International Conference on Nanotechnology*, June 17-20, 2006, Cincinnati, Ohio
26. Ho-Yin Chan, Ning Xi, Jiangbo Zhang, Guangyong Li, Nanoassembly and Packaging of Single Carbon Nanotube Based Transistors, *Proceeding of the 6th IEEE International Conference on Nanotechnology*, June 17-20, 2006, Cincinnati, Ohio
27. Jiangbo Zhang, Ning Xi, Guangyong Li, Sensing in the Nano-environment based on High Order Harmonic Modes of Flexible Arm, *Proceeding of the 4th IFAC Symposium on Mechatronic Systems*, Sept. 12-14, 2006, Heidelberg, Germany
28. Jiangbo Zhang, Ning Xi, Guangyong Li, Chanmin Su, Atomic Force Microscopy Sensing Using Multiple Modes, *Proceeding of the IEEE/RSJ 2006 International Conference on Intelligent Robots and Systems*, Oct. 9-15, 2006, Beijing, China
29. U.C. Wejinya, Yantao Shen, Ning Xi, Jiangbo Zhang, Microfluidic end effector for manufacturing of nano devices, *Proceeding of the 2006 IEEE International Conference on Robotics and Automation*, May 15-19, 2006, Orlando, Florida

30. Ho-Yin Chan, Ning Xi, Jiangbo Zhang, Guangyong Li, Tuning Semiconducting Properties of Single Carbon Nanotube for Fabrication of Nano Devices, *Proceeding of the 1st IEEE International Conference on Nano-Micro Engineered and Molecular Systems*, Jan. 18-21, 2006, Zhuhai, China
31. Jiangbo Zhang, Ning Xi, Guangyong Li, Optimal Control of Flexible End Effector in AFM based Nanomanipulation, *Proceeding of the 2005 IEEE/RSJ International Conference on Intelligent Robots and Systems*, Aug. 2-6, 2005, Edmonton, Canada.
32. Ho-Yin Chan, Ning Xi, Jiangbo Zhang, Guangyong Li, A deterministic process for fabrication and assembly of single carbon nanotube based devices, *Proceeding of the 5th IEEE International Conference on Nanotechnology*, July 11-15, 2005, Nagoya, Japan
33. Jiangbo Zhang, Guangyong Li, Ning Xi, Modeling and Control of Active End Effector for the AFM Based Nano Robotic Manipulators, *Proceeding of the 2005 IEEE International Conference on Robotics and Automation*, April 18-22, 2005, Barcelona, Spain.
34. Heping Chen, Ning Xi, Guangyong Li, Jiangbo Zhang, Prokos, M., Planning and Control for Automated Nanorobotic Assembly, *Proceeding of the 2005 IEEE International Conference on Robotics and Automation*, April 18-22, 2005, Barcelona, Spain.
35. Guangyong Li, Ning Xi, A. Saeed, Heping Chen, Jiangbo Zhang, W.J. Li, C.K.M. Fung, R.H.M. Chan, Mingjun Zhang, Tzyh-Jong Tarn, Experimental studies of DNA electrical properties using AFM based nano-manipulator, *Proceeding of the 4th IEEE Conference on Nanotechnology*, August 17-19, 2004, Munic, Germany

BIBLIOGRAPHY

BIBLIOGRAPHY

- [1] Sumio Iijima. Helical microtubules of graphitic carbon. *Nature*, 354:56–58, 1991.
- [2] Adrian Bachtold, Peter Hadley, Takeshi Nakanishi, and Cees Dekker. Logic circuits with carbon nanotube transistors. *Science*, 294:1317–1320, 2001.
- [3] Derycke V, Martel R, Appenzeller J, and Avouris P. Carbon nanotube inter- and intramolecular logic gates. *Nano Letters*, 1:453–456, 2001.
- [4] Dong Qian, Gregory J Wagner, Wing Kam Liu, Min-Feng Yu, and Rodney S Ruoff. Mechanics of carbon nanotubes. *Applied Mechanics Reviews*, 55:495–533, 2002.
- [5] Paul L. McEuen, Michael S. Fuhrer, and Hongkun Park. Single-walled carbon nanotube electronics. *IEEE Transactions on Nanotechnology*, 1:78–85, 2002.
- [6] Q Z Xue. Model for the effective thermal conductivity of carbon nanotube composites. *Nanotechnology*, 17:1655–1660, 2006.
- [7] M.S. Dresselhaus, G. Dresselhaus, A. Jorio, A.G. Souza Filho, and R. Saito. Raman spectroscopy on isolated single wall carbon nanotubes. *Carbon*, 40:2043–2061, 2002.
- [8] Robert J. Chen, Nathan R. Franklin, Jing Kong, Jien Cao, Thomas W. Tombler, Yuegang Zhang, , and Hongjie Dai. Molecular photodesorption from single-walled carbon nanotubes. *Appl. Phys. Lett.*, 79:2258–2260, 2001.
- [9] Akihiko Fujiwara, Yasuyuki Matsuoka, Hiroyoshi Suematsu, Naoki Ogawa, Kenjiro Miyano, Hiromichi Kataura, Yutaka Maniwa, Shinzo Suzuki, and Yohji Achiba. Photoconductivity in semiconducting single-walled carbon nanotubes. *Jpn. J. Appl. Phys.*, 40:L1229–L1231, 2001.
- [10] I. A. Levitsky and W. B. Euler. Photoconductivity of single-wall carbon nanotubes under continuous-wave near-infrared illumination. *Appl. Phys. Lett.*, 83:1857–1859, 2003.

- [11] Liyue Liu and Yafei Zhang. Multi-wall carbon nanotube as a new infrared detected material. *Sensors and Actuators A*, 116:394-397, 2004.
- [12] Kannan Balasubramanian, Yuwei Fan, Marko Burghard, Klaus Kern, Marcel Friedrich, Uli Wannek, and Alf Mews. Photoelectronic transport imaging of individual semiconducting carbon nanotubes. *Appl. Phys. Lett.*, 84:2400-2402, 2004.
- [13] M. Freitag, Y. Martin, J. A. Misewich, R. Martel, and Ph. Avouris. Photoconductivity of single carbon nanotubes. *Nano Letters*, 3:1067-1071, 2003.
- [14] Ji Ung Lee. Photovoltaic effect in ideal carbon nanotube diodes. *Appl. Phys. Lett.*, 87:073101, 2005.
- [15] A. Mohite, S. Chakraborty, P. Gopinath, G. U. Sumanasekera, and B. W. Alphenaar. Displacement current detection of photoconduction in carbon nanotubes. *Appl. Phys. Lett.*, 86:06114, 2005.
- [16] Hongjie Dai. Carbon nanotubes: Synthesis, integration, and properties. *Acc. Chem. Res*, 35:1035-1044, 2002.
- [17] M. Dresselhaus, G. Dresselhaus, and Phaedon Avouris (Eds.). *Carbon Nanotubes: Synthesis, Structure, Properties and Application*. Springer, Berlin, 2001.
- [18] J. W. Mintmire, B. I. Dunlap, and C. T. White. Are fullerene tubules metallic? *Phys. Rev. Lett.*, 68:631 - 634, 1992.
- [19] M. S. Dresselhaus, G. Dresselhaus, and Riichiro Saito. Carbon fibers based on c60 and their symmetry. *Phys. Rev. B*, 45:6234 - 6242, 1992.
- [20] Phaedon Avouris. Carbon nanotube electronics. *Chemical Physics*, 281:429-445, 2002.
- [21] Philip G. Collins and Phaedon Avouris. Carbon fibers based on c60 and their symmetry. *Scientific American*, 283:62-29, 2000.
- [22] H. Dai. Carbon nanotubes: opportunities and challenges. *Surf. Sci.*, 500:218-241, 2002.
- [23] Markus Ahlskog, Pertti Hakonen, Mikko Paalanen, Leif Roschier, and Reeta Tarkiainen. Multiwalled carbon nanotubes as building blocks in nanoelectronics. *Journal of Low Temperature Physics*, 124:335-352, 2001.
- [24] B. Q. Wei, R. Vajtai, and P. M. Ajayan. Reliability and current carrying capacity of carbon nanotubes. *Appl. Phys. Lett.*, 79:1172-1174, 2001.

- [25] N. Srivastava and K. Banerje. Performance analysis of carbon nanotube interconnects for vlsi applications. In *Proc. of the 2005 IEEE/ACM Int. Conf. on Computer-aided design*, pages 383–390, San Jose, CA, 2005.
- [26] S. J. Wind, J. Appenzeller, and Ph. Avouris. Lateral scaling in carbon-nanotube field-effect transistors. *Phys. Rev. Lett.*, 91(5):058301, Jul 2003.
- [27] S. Hasan, S. Salahuddin, M. Vaidyanathan, and M. A. Alam. High-frequency performance projections for ballistic carbon-nanotube transistor. *IEEE Transactions on Nanotechnology*, 5:14–22, 2006.
- [28] J. Appenzeller, Yu-Ming Lin, J. Knoch, Zhihong Chen, and P. Avouris. Comparing carbon nanotube transistors - the ideal choice: A novel tunneling device design. *IEEE Transactions on Electron Devices*, 52:2568–2576, 2005.
- [29] S. J. Wind, J. Appenzeller, R. Martel, V. Derycke, and Ph. Avouris. Vertical scaling of carbon nanotube field-effect transistors using top gate electrodes. *Applied Physics Letters*, 80:2002, 3817–3819.
- [30] D. V. Singh, K. A. Jenkins, J. Appenzeller, D. Neumayer, A. Grill, and H.-S. P. Wong. Frequency response of top-gated carbon nanotube field-effect transistors. *IEEE Transactions on Nanotechnology*, 3:383–387, 2004.
- [31] Z. Chen, J. Appenzeller, Y.-M. Lin, J. Sippel-Oakley, A. G. Rinzler, J. Tang, S. J. Wind, P. M. Solomon, and Ph. Avouris. An integrated logic circuit assembled on a single carbon nanotube. *Science*, 311:1735, 2006.
- [32] Marcus Freitag, Vasili Perebeinos, Jia Chen, Aaron Stein, James C. Tsang, James A. Misewich, Richard Martel, and Phaedon Avouris. Hot carrier electroluminescence from a single carbon nanotube. *Nano Letters*, 4:1063–1066, 2004.
- [33] Shaoxin Lu and Balaji Panchapakesan. Photoconductivity in single wall carbon nanotube sheets. *Nanotechnology*, 17:1843–1850, 2006.
- [34] Nathan R. Franklin, Qian Wang, Thomas W. Tomblor, Ali Javey, Moonsub Shim, and Hongjie Dai. Integration of suspended carbon nanotube arrays into electronic devices and electromechanical systems. *Appl. Phys. Lett.*, 81:913–915, 2002.
- [35] Pengfei Qi, Ophir Vermesh, Mihai Grecu, Ali Javey, Qian Wang, Hongjie Dai, Shu Peng, and K. J. Cho. Toward large arrays of multiplex functionalized carbon nanotube sensors for highly sensitive and selective molecular detection. *Nano Lett.*, 3:347–351, 2003.

- [36] Alireza Nojeh, Ant Ural, R. Fabian Pease, and Hongjie Dai. Electric-field-directed growth of carbon nanotubes in two dimensions. *J. Vac. Sci. Technol. B*, 22:3421–3425, 2004.
- [37] Jingqi Li, Qing Zhang, Dajiang Yang, and Jingze Tian. Fabrication of carbon nanotube field effect transistors by ac dielectrophoresis method. *Carbon*, 42:2263–2267, 2004.
- [38] Sebastian Taeger, Daniel Sickert, Petar Atanasov, Gerald Eckstein, and Michael Mertig. Self-assembly of carbon nanotube field-effect transistors by ac-dielectrophoresis. *phys. stat. sol. (b)*, 243:3355–3358, 2006.
- [39] S. Banerjee, B. White, L. Huang, B.J. Rego, S. O’Brien, and I.P. Herman. Precise positioning of carbon nanotubes by ac dielectrophoresis using floating posts. *Appl. Phys. A*, 86:415–419, 2007.
- [40] P. Makaram, S. Selvarasah, X. Xiong, C.-L. Chen, A. Busnaina, N. Khanduja, and M. R. Dokmeci. Three-dimensional assembly of single-walled carbon nanotube interconnects using dielectrophoresis. *Nanotechnology*, 18:395204, 2007.
- [41] Zhihong Chen, Joerg Appenzeller, Joachim Knoch, Yu ming Lin, and Phaedon Avouris. The role of metal-nanotube contact in the performance of carbon nanotube field-effect transistors. *Nano Letters*, 5:1497–1502, 2005.
- [42] Chenguang Lu, Lei An, Qiang Fu, Jie Liu, Hong Zhang, and James Murduck. Schottky diodes from asymmetric metal-nanotube contacts. *Appl. Phys. Lett.*, 88:133501, 2006.
- [43] David Perello, Moon J. Kim, DongKyu Cha, Gang Hee Han, Dong Jae Bae, Seung Yol Jeong, Young Hee Lee, and Minhee Yun. Schottky barrier engineering in carbon nanotube with various metal electrodes. In *Proceedings of the 7th IEEE International Conference on Nanotechnology*, pages 189–193, Hong Kong, Aug. 2007.
- [44] J. Lefebvre, M. Radosavljević, and A. T. Johnson. Fabrication of nanometer size gaps in a metallic wire. *Appl. Phys. Lett.*, 76:3828–3830, 2000.
- [45] Mandar M. Deshmukh, D. C. Ralph, M. Thomas, and J. Silcox. Nanofabrication using a stencil mask. *Appl. Phys. Lett.*, 75:1631–1633, 1999.
- [46] Saleem G. Rao, Ling Huang, Wahyu Setyawan, and Seunghun Hong. Large-scale assembly of carbon nanotubes. *Nature*, 425:36–37, 2003.
- [47] Miron Hazani, Frank Hennrich, Manfred Kappes, Ron Naaman, Dana Peled, Victor Sidorov, and Dmitry Shvarts. Dna-mediated self-assembly of carbon nanotube-based electronic devices. *Chem. Phys. Lett.*, 391:389–392, 2004.

- [48] Zhifeng Deng, Erhan Yenilmez, Amy Reilein, Joshua Leu, Hongjie Dai, and Kathryn A. Moler. Nanotube manipulation with focused ion beam. *Appl. Phys. Lett.*, 88:023119, 2006.
- [49] MinFeng Yu, Mark J Dyer, George D Skidmore, Henry W Rohrs, XueKun Lu, Kevin D Ausman, James R Von Ehr, and Rodney S Ruoff. Three-dimensional manipulation of carbon nanotubes under a scanning electron microscope. *Nanotechnology*, 10:244–252, 1999.
- [50] Tobias Hertel, Richard Martel, and Phaedon Avouris. Manipulation of individual carbon nanotubes and their interaction with surfaces. *J. Phys. Chem. B*, 102:910–915, 1998.
- [51] Ph. Avouris, T. Hertel, R. Martel, T. Schmidt, H.R. Shea, and R.E. Walkup. Carbon nanotubes: nanomechanics, manipulation, and electronic devices. *Appl. Surf. Sci.*, 141:201–209, 1999.
- [52] Henk W. C. Postma, Allard Sellmeijer, and Cees Dekker. Manipulation and imaging of individual single-walled carbon nanotubes with an atomic force microscope. *Adv. Mater.*, 12:1299–1302, 2000.
- [53] G. Binnig, C. F. Quate, and C. Gerber. Atomic force microscope. *Phys. Rev. Lett.*, 56(9):930–933, 1986.
- [54] Claudio Rivetti, Chip Walker, and Carlos Bustamante. Polymer chain statistics and conformational analysis of dna molecules with bends or sections of different flexibility. *Journal of Molecular Biology*, 280:41–59, 1998.
- [55] Masato Tanigawa, Masanori Gotoh, Masayuki Machida, Takao Okada, and Michio Oishi. Detection and mapping of mismatched base pairs in dna molecules by atomic force microscopy. *Nucleic Acids Research*, 28:e38–e38, 2000.
- [56] S. Boichot, M. Fromm, S. Cunniffe, P. O’Neill, J. C. Labrune, A. Chambaudet, E. Delain, and E. Le Cam. Investigation of radiation damage in dna by using atomic force microscopy. *Radiation Protection Dosimetry*, 99:143–146, 2002.
- [57] Aiguo Wu, Lihua Yu, Zhuang Li, Huanming Yang, and Erkang Wang. Atomic force microscope investigation of large-circle dna molecules. *ANALYTICAL BIOCHEMISTRY*, 325:293–300, 2004.
- [58] Minoru Takeuchi, Hiroshi Miyamoto, Yasushi Sako, Hideo Komizu, and Akihiro Kusumi. Structure of the erythrocyte membrane skeleton as observed by atomic force microscopy. *Biophysical Journal*, 74:2171–2183, 1998.

- [59] Nuno C. Santos, Evgeny Ter-Ovanesyan, Joseph A. Zasadzinski, Manuel Prieto, and Miguel A. R. B. Castanho. Filipin-induced lesions in planar phospholipid bilayers imaged by atomic force microscopy. *Biophysical Journal*, 75:1869–1873, 1998.
- [60] F. VALLE, J. A. DEROSE, G. DIETLER, M. KAWA, A. PLÜCKTHUN, and G. SEMENZA. Imaging the native structure of the chaperone protein groel without fixation using atomic force microscopy. *Journal of Microscopy*, 203:195–198, 2001.
- [61] FM Ohnesorge, JK Horber, W Haberle, CP Czerny, DP Smith, and G Binnig. Afm review study on pox viruses and living cells. *Biophysical Journal*, 73:1997, 2183-2194.
- [62] Filip Braet, Ronald de Zanger, Carine Seynaeve, Marijke Baekeland, and Eddie Wisse. A comparative atomic force microscopy study on living skin fibroblasts and liver endothelial cells. *Journal of Electron Microscopy*, 50:283–290, 2001.
- [63] Jordanka Zlatanova, Stuart M. Lindsay, and Sanford H. Leuba. Single molecule force spectroscopy in biology using the atomic force microscopy. *Progress in Biophysics & Molecular Biology*, 74:37–61, 2000.
- [64] FranÇOis Ahimou, Frédéric A. Denis, Ahmed Touhami, and Yves F. Dufrière. Probing microbial cell surface charges by atomic force microscopy. *Langmuir*, 18:9937–9941, 2002.
- [65] Shuhei Nishida, Yutaka Funabashi, and Atsushi Ikai. Combination of afm with an objective-type total internal reflection fluorescence microscope (tirfm) for nanomanipulation of single cells. *Ultramicroscopy*, 91:269–274, 2002.
- [66] Robert W. Stark, Francisco J. Rubio-Sierra, Stefan Thalhammer, and Wolfgang M. Heckl. Combined nanomanipulation by atomic force microscopy and uv-laser ablation for chromosomal dissection. *European Biophysics Journal*, 32:33–39, 2003.
- [67] Sitti Metin. *Teleoperated 2-D Micro/Nanomanipulation Using Atomic Force Microscope*. PhD thesis, University of Tokyo, 1999.
- [68] T. Junno, K. Deppert, L. Montelius, and L. Samuelson. Controlled manipulation of nanoparticles with an atomic force microscope. *Appl. Phys. Lett.*, 66(26):3627–3629, June 1995.
- [69] D. M. Schaefer, R. Reifenberger, A. Patil, and R. P. Andres. Fabrication of two-dimensional arrays of nanometer-size clusters with the atomic force microscope. *Appl. Phys. Lett.*, 66:1012–1014, Feb. 1995.

- [70] R. W. Stark, S. Thalhammer, J. Wienberg, and W. M. Heckl. The afm as a tool for chromosomal dissection-the influence of physical parameter. *Appl. Phys. A*, 66:579–584, 1998.
- [71] A. A. G. Requicha, C. Baur, A. Bugacov, B. C. Gazen, B. Koel, A. Madhukar, T. R. Ramachandran, R. Resch, and P. Will. Nanorobotic assembly of two-dimensional structures. In *Proc. IEEE Int. Conf. Robotics and Automation*, pages 3368–3374, Leuven, Belgium, May 1998.
- [72] L. T. Hansen, A. Kuhle, A. H. Sorensen, J. Bohr, and P. E. Lindelof. A technique for positioning nanoparticles using an atomic force microscope. *Nanotechnology*, 9:337–342, 1998.
- [73] M. Falvo, R. Superfine, S. Washburn, M. Finch, R.M. Taylor, V.L. Chi, and F.P. Brooks Jr. The nanomanipulator: A teleoperator for manipulating materials at the nanometer scale. In *Proceedings of the International Symposium on the Science and Technology of Atomically Engineered Materials*, pages 579–586, Richmond VA, Oct. 1995.
- [74] M. Sitti and H. Hashimoto. Tele-nanorobotics using atomic force microscope. In *Proc. IEEE Int. Conf. Intelligent Robots and Systems*, pages 1739–1746, Victoria, B. C., Canada, October 1998.
- [75] M. Sitti and H. Hashimoto. Controlled pushing of nanoparticles: modeling and experiments. *IEEE/ASME Trans. on Mechatronics*, 5:199–211, 2000.
- [76] G. Y. Li, N. Xi, M. Yu, and W. K. Fung. Modeling of 3-d interactive forces in nanomanipulation. In *Proc. IEEE Int. Conf. Intelligent Robots and Systems*, pages 2127–2132, Las Vegas, NV, Oct. 28-30 2003.
- [77] Guangyong Li, Ning Xi, Mengmeng Yu, and Wai Keung Fung. Augmented reality system for real-time nanomanipulation. In *Proc. IEEE Int. Conf. Nanotechnology*, San Francisco, CA, August 12-14 2003.
- [78] G. Y. Li, N. Xi, and M. Yu. Development of augmented reality system for afm based nanomanipulation. *IEEE/ASME Trans. on Mechatronics*, 9:358–365, June 2004.
- [79] Guangyong Li, Ning Xi, Heping Chen, Craig Pomeroy, and Mathew Prokos. "videolized" atomic force microscopy for interactive nanomanipulation and nanoassembly. *IEEE Transactions on Nanotechnology*, 4:605–615, 2005.
- [80] B. Mokaberi and A. A. G. Requicha. Towards automatic nanomanipulation: drift compensation in scanning probe microscopes. In *Proc. IEEE Int. Conf. Robotics and Automation*, pages 416–421, New Orleans, April 2004.

- [81] M. Guthold, M. R. Falvo, W. G. Matthews, S. Paulson, S. Washburn, and D. A. Erie. Controlled manipulation of molecular samples with the nanomanipulator. *IEEE/ASME Trans. on Mechatronics*, 5(2):189–198, June 2000.
- [82] S.R. Manalis, S. C. Minne, and C. F. Quate. Atomic force microscopy for high speed imaging using cantilevers with an integrated actuator and sensor. *Applied Physics Letters*, 68:871–873, 1996.
- [83] T. Sulchek, S. C. Minne, J. D. Adams, D. A. Fletcher, A. Atalar, C. F. Quate, and D. M. Adderton. Dual integrated actuators for extended range high speed atomic force microscopy. *Applied Physics Letters*, 75:1637–1639, 1999.
- [84] T. Sulchek, R. Hsieh, J. D. Adams, G. G. Yaralioglu, S. C. Minne, C. F. Quate, J. P. Cleveland, A. Atalar, and D. M. Adderton. High-speed tapping mode imaging with active qcontrol for atomic force microscopy. *Applied Physics Letters*, 76:1473–1475, 2000.
- [85] G. Y. Li, N. Xi, and M. Yu. Calibration of afm based nanomanipulation system. In *Proc. IEEE Int. Conf. Robotics and Automation*, New Orleans, LA, April 26-May 1 2004.
- [86] E. Volterra and E.C. Zachmanoglou. *Dynamics of Vibrations*. Charles E. Merrill, Ohio, USA, 1965.
- [87] Thomas Bailey and James E. Hubbard Jr. Distributed piezoelectric-polymer active vibration control of a cantilever beam. *J. Guidance, Control and Dynamics*, 8:605–611, 1985.
- [88] Chonan S., Jiang Z.W., and Koseki M. Soft-handling gripper driven by piezoceramic bimorph strips. *Smart Materials and Structures*, 5:407–414, 1996.
- [89] S.B. Choi and C.H. Lee. Force tracking control of a flexible gripper driven by piezoceramic actuator. *ASME Journal of Dynamic Systems, Measurement, and Control*, 119:439–446, 1997.
- [90] Dong Sun and James K. Mills. Combined pd feedback and distributed piezoelectric-polymer vibration control of a single-link flexible manipulator. In *Proc. IEEE/RSJ International Conference on Intelligent Robots and Systems*, pages 667–672, Victoria, B.C., Canada, Oct. 1998.
- [91] A.N. Singh and Y.M. Ram. Dynamic absorption in a vibrating beam. *Journal of Mechanical Engineering Science*, 217:187–197, 2003.
- [92] H. Kataura, Y. Kamazawa, Y. Maniwa, I. Umezumi, S. Suzuki, Y. Ohtsuka, and Y. Achiba. Optical properties of single-wall carbon nanotubes. *Synth. Met.*, 103:2555–2558, 1999.

- [93] R. Jacquemin, S. Kazaoui, D. Yu, A. Hassanien, N. Minami, H. Kataura, , and Y. Achiba. Doping mechanism in single-wall carbon nanotubes studied by optical absorption. *Synth. Met.*, 115:283– 287, 2001.
- [94] L. Kavan, P. Raptá, L. Dunsch, M. J. Bronikowski, P. Willis, and R.E. Smalley. Electrochemical tuning of electronic structure of single-walled carbon nanotubes: in-situ raman and vis-nir study. *J. Phys. Chem. B*, 105:10764–10771, 2001.
- [95] S. M. Bachilo, M. S. Strano, C. Kittrell, R. H. Hauge, R. E. Smalley, and R. B. Weisman. Structure-assigned optical spectra of single-walled carbon nanotubes. *Science*, 298:2361–2366, 2002.
- [96] Yoshiyuki Miyamoto, Noboru Jinbo, Hisashi Nakamura, Angel Rubio, and David Tománek. Photodesorption of oxygen from carbon nanotubes. *Physical Review B*, 70:233408, 2004.
- [97] M. J. O’Connell, S. M. Bachilo, C. B. Huffman, V. C. Moore, M. S. Strano, E. H. Haroz, K. L. Rialon, P. J. Boul, W. H. Noon, C. Kittrell, J. Ma, R. H. Hauge, R. B. Weisman, and R. E. Smalley. Band gap fluorescence from individual single-walled carbon nanotubes. *Science*, 297:593–596, 2002.
- [98] J.A. Misевич, R. Martel, Ph. Avouris, J.S. Tsang, S. Heinze, and J. Tersoff. Electrically induced optical emission from carbon nanotube fet. *Science*, 300:783–786, 2003.
- [99] Woong Kim, Ali Javey, Ryan Tu, Jien Cao, Qian Wang, and Hongjie Dai. Electrical contacts to carbon nanotubes down to 1 nm in diameter. *Appl. Phys. Lett.*, 87:173101, 2005.
- [100] Norbert Nemeč, David Tománek, and Gianaurelio Cuniberti. Contact dependence of carrier injection in carbon nanotubes: An ab initio study. *Phys. Rev. Lett.*, 96:076802, 2006.
- [101] Wenguang Zhu and Efthimios Kaxiras. Schottky barrier formation at a carbon nanotubemetal junction. *Appl. Phys. Lett.*, 89:243107, 2006.
- [102] M. H. Yang, K. B. K. Teo, and W. I. Milne. Carbon nanotube schottky diode and directionally dependent field-effect transistor using asymmetrical contacts. *Appl. Phys. Lett.*, 87:253116, 2005.
- [103] Harish M. Manohara, Eric W. Wong, Erich Schlecht, Brian D. Hunt, and Peter H. Siegel. Carbon nanotube schottky diodes using ti-schottky and pt-ohmic contacts for high frequency applications. *Nano Letters*, 5:1469–1474, 2005.

- [104] Ali Javey, Jing Guo, Qian Wang, Mark Lundstrom, and Hongjie Dai. Ballistic carbon nanotube field-effect transistors. *Nature*, 424:654–657, 2003.
- [105] [online]. available: <https://www.veecoprobes.com>.
- [106] Edward F. Crawley and Javier de Luis. Use of piezoelectric actuators as elements of intelligent structures. *AIAA*, 25:1373–1385, 1987.
- [107] Stewart John Moorehead. Position and force control of flexible manipulators. Master's thesis, University of Waterloo, 1996.
- [108] William L. Brogan. *Modern Control Theory*. Prentice Hall, Englewood Cliffs, N.J., third edition, 1991.
- [109] Peter Dorato, Chaouki Abdallah, and Vito Cerone. *Linear-Quadratic Control: An Introduction*. Prentice Hall, Englewood Cliffs, N.J., 1995.
- [110] G. F. Franklin, J. D. Powell, and A. Emami-Naeini. *Feedback Control of Dynamic systems*. Prentice Hall, Upper Saddle River, NJ, fourth edition, 2002.
- [111] [Online]. Available: <http://www.rtai.org>.
- [112] William Singhose and Neil singer. Initial investigations into the effects of input shaping on trajectory. In *Proceedings of the 1994 American Control Conference*, pages 2526–2632, Baltimore, MD, test 1994.
- [113] Ho-Yin Chan, Ning Xi, Jiangbo Zhang, and Guangyong Li. Tuning semiconducting properties of single carbon nanotube for fabrication of nano devices. In *Proceedings of the 1st IEEE International Conference on Nano/Micro Engineered and Molecular Systems*, pages 1410–1413, Zhuhai, China, Jan. 2006.
- [114] Xiaodong Cui, Marcus Freitag, Richard Martel, Louis Brus, and Phaedon Avouris. Controlling energy-level alignments at carbon nanotube/au contacts. *Nano Letters*, 3:783–787, 2003.
- [115] Amitesh Maiti and Alessandra Ricca. Metal-nanotube interactions - binding energies and wetting properties. *Chemical Physics Letters*, 395:7–11, 2004.
- [116] King W.C. Lai, Ning Xi, Jiangbo Zhang, Guangyong Li, and Hongzhi Chen. Packaging carbon nanotube based infrared detector. In *Proc. IEEE Int. Conf. Nanotechnology*, pages 778 – 781, Hong Kong, August 2007.
- [117] Derek A. Stewart and Francois Leonard. Energy conversion efficiency in nanotube optoelectronics. *Nano Letters*, 5:2005, 219–222.
- [118] G. Y. Guo and K. C. Chu. Linear and nonlinear optical properties of carbon nanotubes from first-principles calculations. *Phys. Rev. B*, 69:205416, 2004.

- [119] D. P. Neikirk, D. B. Rutledge, and W. Lam. Far-infrared microbolometer detectors. *International Journal of Infrared and Millimeter Waves*, 5:245–277, 1984.
- [120] H.C. Liu. Quantum dot infrared detector. *OPTO-ELECTRONICS REVIEW*, 11:1–5, 2003.
- [121] Joseph N. Zalameda and andWilliam P.Winfrey. Investigation of uncooled microbolometer focal plane array infrared camera for quantitative thermography. *Journal of Nondestructive Evaluation*, 24:1–9, 2005.
- [122] Sanjay Krishna, Sarath D. Gunapala, Sumith V. Bandara, Cory Hill, and David Z. Ting. Quantum dot based infrared focal plane arrays. *Proceedings of the IEEE*, 95:1838–1852, 2007.
- [123] J.L. Tissot. Ir detector with uncooled focal plane arrays, state-of-the art and trends. *OPTO-ELECTRONICS REVIEW*, 12:105–109, 2004.

MICHIGAN STATE UNIVERSITY LIBRARIES



3 1293 03062 7511